Microstructural Characterization of Quenched and Tempered Heat-treated P110 Casing Steels

by

Mingzhang Yang

A thesis submitted in partial fulfilment of the requirements for the degree of

Master of Science

In

Materials Engineering

Department of Chemical and Materials Engineering

University of Alberta

© Mingzhang Yang, 2021

Abstract

P110 is a quenched and tempered (Q&T) heat-treated high strength casing used in oil/gas mild sour well drilling. Critical properties influencing performance are strength and hydrogen embrittlement (HE) resistance, which are related to carbide morphology, steel composition, and Q&T conditions. This study investigated the effects of Cr and C content, as well as Q&T conditions on the type and morphology of carbides that form in P110 steel. Specifically, a series of Q&T heat treatments were conducted on as-rolled steels with two nominal compositions, 0.278C-0.77Cr and 0.255C-0.52Cr (wt%).

The effects of austenitizing and quenching (A&Q) treatment (950°C for 15 to 90 min) on as-rolled P110 plates were studied using optical microscopy (OM), micro-hardness, x-ray diffraction (XRD), scanning electron microscopy (SEM), electron backscatter diffraction (EBSD), electron microprobe analysis (EMPA), and scanning-transmission electron microscopy (TEM/STEM). Microsegregation of Cr and Mo was observed in the as-rolled steels with the former exhibiting a higher extent of microsegregation. A&Q at 950°C for 30 min caused a slight reduction in the extent of microsegregation, but the growth in prior austenite grain (PAG) size during this period was significant. Based on the optimum balance bewteen solutionizing and PAG growth, A&Q steels from 950°C for 15 min were selected as the starting materials for tempering studies. The A&Q steel (950°C-15 min) contained less 0.5 vol% retained austenite, and a fine PAG size (~ 11 µm), as well as fine (< 20 nm) and dispersed (Ti, Mo)C carbides formed during the hot-rolling process.

Following A&Q treatment, the effects of tempering conditions on carbide morphology were studied by tempering the A&Q treated steels (950°C-15 min) between 550°C and 715°C for

15 min to 390 min. The carbide morphology (i.e., type, size, shape, volume fraction, and distribution) was studied using SEM and STEM. The relations among carbide morphology, steel composition, and tempering conditions were studied using Thermo-Calc simulations. The average Mo content in the metallic constituent of (Ti, Mo)C particles increased from 34 to 44 wt% after tempering at 715°C for 45 min, whereas their shapes and size distribution were unaffected by subsequent tempering heat treatments. Coarsening of M_3C particles was accelerated by increasing tempering temperature (T), particularly at $T > 650$°C. It is noteworthy that after tempering at 650°C for 45 min, M_3C particles in ferrite were enriched in Cr and approached equilibrium. Any increase in tempering T or t beyond this condition led to a significant increase in particle size and a decrease in number density. The increase in nominal Cr and C content did not result in a prominent difference in the size and volume fraction of tempered carbides. However, $M_{23}C_6$ carbides were only identified in tempered 0.77Cr steel as a result of the higher nominal Cr content.

The effects of carbide morphology on tempered structure were studied. With increasing tempering temperature, coarsened carbides reduced the pinning action of lath boundaries, which enabled lath structure coarsening. The average lath width at temperatures of 600°C, 650°C, and 715°C (45 min) corresponded to 329 ± 69 nm, 335 ± 89 nm, and 638 ± 90 nm, respectively, with the most substantial change in coarsening occurring between 650°C and 715°C.

Micro-hardness and tensile testing were undertaken for the Q&T steels. The hardness and tensile properties after tempering for any combination of t and T exhibited a linear behavior when plotted against the Holloman Jaffe (HJ) parameter. A reduction in softening during tempering for HJ < 17.4 was observed, which was associated with the grain boundary pinning action from fine and uniformly distributed (Ti, Mo)C and M_3C particles. The continuous decrease in hardness and

iii

tensile properties with increase tempering T or t was attributed to the combined effects of M_3C coarsening, dislocation annihilation, and lath structure coarsening.

To produce P110 steel that meets the minimum YS requirements from the API 5CT standard, tempering should be conducted at conditions where HJ < 18.4. Unless tempering t is sufficiently low, the tempering T should not exceed 650°C to acquire sufficient strength. In terms of HE resistance, the optimum carbide morphology can be obtained by tempering at 650°C for 45 min, where uniformly distributed fine particles (60-65 nm) with a high number density ($51/\mu m^2$) and volume fraction (0.11) are produced.

Acknowledgments

Table of content

Chapter 5

List of Tables

List of Figures

x

Chapter 1

Introduction

The oil and gas industry requires steel casing in downhole applications for mild sour service (H_2S) conditions and at temperatures > 80°C. These conditions can result in hydrogen damage of the steel and ultimately failure. Therefore, a higher grade of casing steel capable of withstanding high mechanical loads and resisting hydrogen embrittlement (HE) is required. The favorable properties of P110, a heat treatable steel, are achieved for casing applications through a combination of suitable composition and by the appropriate heat treatment conditions (i.e., tempering temperature).

Quenching and tempering (Q&T) heat treatment has been proven to provide greater resistance to HE failures than as-rolled, normalized steels [1]. Therefore, with an understanding of the benefits of employing Q&T as a treatment process to reduce HE, extensive efforts were made to achieve a combination of high strength, toughness, and enhanced HE resistance. This is achieved by concurrently optimizing Q&T conditions, alloying design, and metallurgical quality [2,3]. Metallurgical factors that affect the performance of P110 in mild sour well applications are [1-4]:

1] Tensile strength and hardness
2] Grain size, and grain boundary angles
3] Microstructural and elemental (i.e., segregation) uniformity
4] As quenched martensite fraction
5] Steel cleanliness
6] Carbide morphologies: types, size, volume fraction, distribution, shape, and interparticle spacing

In particular, the relationship between carbide morphology and steel composition and/or Q&T conditions (temperature/time) has been deemed important with regards to HE resistance. Previous studies reported that the evenly dispersed and fine (<50 nm) precipitates, such as TiC and Mo_2C, are strong irreversible H traps and conducive to improve HE resistance [2-5]. Carbide type and morphology (for Q&T products) are influenced by composition, tempering temperature and time

[6]. It is of interest to determine whether the morphology of tempered carbides can be affected by only adjusting the Cr and C content, as well as tempering conditions. In addition, there is still no systematic study investigating the sour service of high strength Cr-Mo alloy steel, particularly a steel with low Cr (< 1 wt%) and medium C (0.25 to 0.4 wt%) content.

The research aims of this work are: 1] Quantify the effect of Cr and C content and tempering conditions on the type and morphology of precipitates that form in quenched and tempered P110 steel. 2] Investigate the effect of carbide morphology on tensile properties and hardness. 3] Validate precipitate observations with thermodynamic calculations (Thermo-Calc).

To accomplish these objectives, a series of Q&T heat treatments were conducted on two compositions of P110 steel (0.77 wt% Cr and 0.52 wt% Cr). The microstructure of the steel (at each stage in the processing) was examined using optical microscopy (OM), scanning electron microscopy (SEM), X-ray diffraction (XRD), and transmission electron microscopy (TEM) for phase identification, grain size measurement, and precipitation characterization. Hardness measurements were taken for both the as-quenched and Q&T conditions. Tensile tests were conducted for the tempered steel. The type, fraction, and composition of precipitates were predicted using Thermo-Calc.

The thesis is divided into six (6) chapters. Chapter 2 presents an introduction to P110 casing steel for mild sour service, HE mechanisms, Q&T heat treatments and the metallurgical factors associated with HE. Chapter 3 documents the experimental approach and techniques used during this study. Chapter 4 details and discusses the microstructure analysis of both the quenched martensite structure and the as-rolled plate. Chapter 5 presents the metallurgical characterization of the tempered P110. Chapter 6 provides a summary of this study as well as opportunities for future work. Additional details on tested and characterized specimens can be found in the appendices.

Chapter 2

Literature Review

This literature review includes an introduction to casing steel used for sour service with an emphasis on the heat treatment of P110. A review of the mechanisms of the hydrogen embrittlement (HE) is provided. The austenitization and quenching process (AQ), as well as the tempering heat treatment for Cr/Mo steels, is discussed. The latter will focus on the formation and morphological changes of the carbide precipitates. Finally, the effect of microstructure on sour service performance is presented.

2.1 Casing Steel Designation for Sour Service

Since the 1930s, the American Petroleum Institute (API) has issued standards and specifications for casing, tubing, and drill pipe (OCTG-Oil Country Tubular Goods). As indicated by API SPEC 5CT, the steel evaluation of casing steel can be sorted into ten types, including H-40, J-55, K-55, N-80, C-75, L-80, C-90, C-95, P-110, and Q-125 [7]. According to API 5CT, the allowable yield strength for P110 is 758.4 MPa to 965.2 MPa which exceeds the maximum 103.4 MPa range specified by NACE.

The Energy Resources Conservation Board (ERCB) provides guidance for sour service application in Directive 10: sour services refer to service environment (e.g., oil and gas service, transmission pipelines, refinery equipment) which contain hydrogen sulfide (H_2S) equal or greater than 0.3 kPa (0.05 psi) [1]. As shown in Figure 2.1, based on the H_2S partial pressure and the pH of the environment, the severity of sour service is classified into several regions: no sour (0), mild (1), intermediate (2), and severe service region (3) [8]. The vertical line at 0.3 kPa (0.05 psi) separates the sweet service (i.e., no sour service) from the sour service. Grade P110 is designated as a proprietary mild sour (MS) material. It is worth noting that this diagram intends to represent severity according to sulfide stress cracking (SSC), whereas no similar diagram exists for hydrogen induced cracking (HIC).
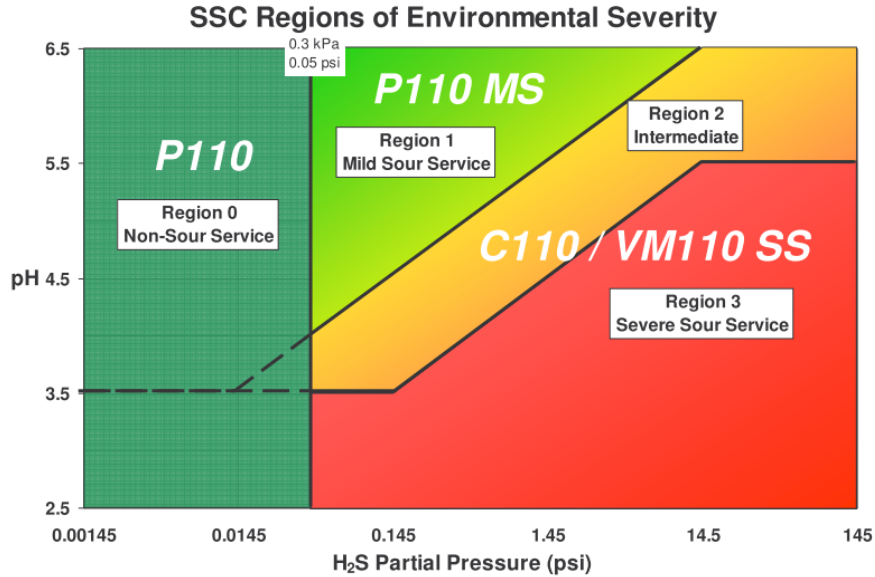
Figure 2.1. Usage domain for 110 ksi grades, adapted from MR0175-2003 / ISO 15156 recommendation at room temperature [1,7].

2.2 Hydrogen Embrittlement (HE) Phenomena

Environmental assisted cracking (EAC) is a contributing factor to the failure of these materials in mild sour environment. It comprises three environmental cracking phenomena: stress-oriented hydrogen-induced cracking (SOHIC), hydrogen-induced cracking (HIC), and sulfide stress cracking (SSC) [9]. HE includes HIC and SSC. For the occurrence of HE, the interaction of the following three conditions needs to be simultaneously satisfied: susceptible material, presence of hydrogen, and a tensile stress. This section contains a comprehensive background about HE, a review of HE mechanisms, and an introduction to environmental cracking phenomena.

2.2.1 Role of hydrogen sulfide (H₂S) in HE

H_2S has long participated in corrosion damage, such as SSC, HIC, and SOHIC of high strength and high hardness carbon (C) steel applied in wet H_2S environments [9]. H_2S can dissolve in an aqueous environment and form corrosive solutions. However, H_2S is not directly involved in SSC or HIC, but rather provides the mechanism for hydrogen evolution by enhancing the iron dissolution rate and increasing the relative amount of atomic hydrogen absorption [10]. In other words, H_2S increases the corrosion rate in aqueous solutions and inhibits the hydrogen

recombination reaction [9]. The corrosion process increases hydrogen charging in an anaerobic environment commonly followed by reactions (2.1), (2.2), (2.3), (2.4) [9]:

Anodic Reaction:

$$Fe \rightarrow Fe^{2+} + 2e^-$$ (Equation 2.1)

Cathodic Reaction:

$$H_2S + H_2O \rightarrow H^+ + HS^- + H_2O$$ (Equation 2.2)

$$HS^- + H_2O \rightarrow H^+ + S^- + H_2O$$ (Equation 2.3)

Net Reaction:

$$Fe + H_2S_{(aquous)} \rightarrow FeS + 2H^o$$ (Equation 2.4)
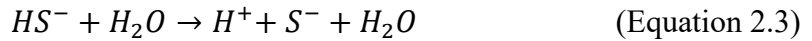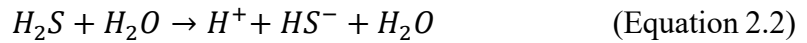
Depending on the pH, H_2S partial pressure, and oxidizing potential of the environment, corrosion products such as FeS (troilite), FeS_2 (pyrite), Fe_7S_8 (pyrrhotite), and Fe_9S_8 (kansite) can be formed [9]. These products of iron have a considerable effect on the kinetics of the corrosion process due to differences between the crystal lattice of the various corrosion products [11].. The hydrogen ions produced in the cathode can commonly recombine to form harmless hydrogen gas on the surface of the steel; however, the presence of sulfide ions hinders the formation of hydrogen molecules [9]. Thus, hydrogen ions can be absorbed into the steel matrix and cause hydrogen embrittlement (to be discussed in Chapter 2.2.2). A schematic of the variation in corrosion rate and hydrogen permeation as a function of H_2S concentration is shown in Figure 2.2. Hydrogen permeation (i.e., diffusion of hydrogen ions) rate increases with the forming of the sulfide, whereas the general corrosion rate reduces due to thickening of the sulfide film thickens [12].
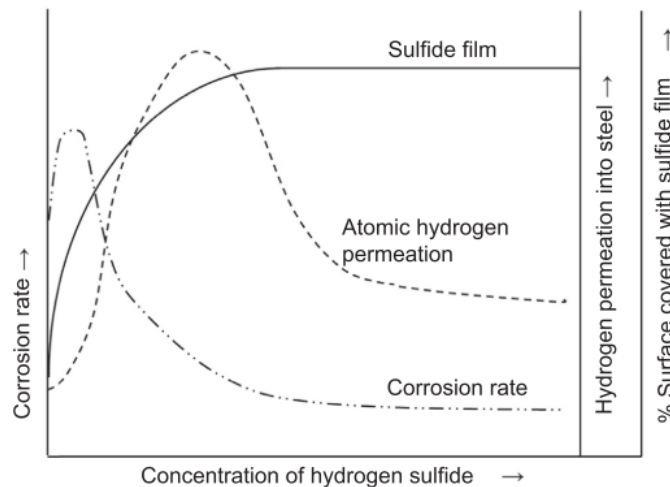
Figure 2.2. Variation in corrosion and hydrogen permeation as a function of H_2S concentration [12].

2.2.2 *Hydrogen embrittlement mechanism*

Many hydrogen embrittlement mechanisms have been proposed in literature: enhanced cleavage, enhanced grain boundary fracture, enhanced shear, localized micro-voids, or all of the above. In this section, the following mechanisms are selected and discussed: hydrogen-enhanced decohesion theory (HEDE), hydrogen enhanced localized plasticity (HELP), and absorption-induced dislocation emission (AIDE).

In 1926, Pfeil proposed the oldest mechanism, the hydrogen-enhanced decohesion (HEDE) theory [13]. He suggested that the cohesion across grain boundaries and cubic cleavage planes was reduced by hydrogen. In 1959, Troiano proposed that the decreased cohesion was due to the electron donation from hydrogen atoms to unfilled 3d atomic orbital of iron (Fe) [14]. Troiano's theory was furtherly quantitatively studied and developed by Oriani [15], Gerberich [16], and others [17]. HEDE indicated that the locations with high H atom concentration or high hydrogen electron density will cause the separation of atoms, thus weakening metal atoms bonds (cohesive strength) and trigger fracture [18]. The HEDE mechanism usually accounts for brittle cracking due to the absence of local deformation. Several locations tend to have a high concentration of absorbed hydrogen and cause decohesion according to Lynch. These include crack tips, grain boundary, and particle-matrix interfaces, where the cohesive strength in the atomic lattice can be easily overcome with the assistance of external stress [19].

Hydrogen enhanced localized plasticity (HELP) theory is constantly competing with HEDE theory, since Beachem's fractographic observation of low alloyed steel in the early 1970s [20]. The idea that solute H atoms facilitate dislocation activity/mobility in the H enriched region which enhances the local plastic deformation, was widely accepted and has been promoted by others since the 1980s. There was extensive evidence to support the theory, ranging from atomistic calculations and in-situ TEM observation of dislocations, to nano-indentation tests and elastic shielding theory [21,22]. Unlike HEDE theory, facilitated localized HELP tends to produce a non-crystallographic ductile/planar slip fracture rather than a macroscopically cleavage-like or brittle intergranular fracture of HEDE [22].

The adsorption-induced dislocation emission (AIDE) model was established on the foundation of both the HEDE and HELP theories. HEDE accounts for the nucleation of fracture (by reducing

atomic cohesive strength), while localized hydrogen atmosphere shielding (i.e., HELP) facilitates the fracture growth. Specifically, the adsorbed hydrogen, located at surfaces or crack tips, promotes the nucleation stages by weakening interatomic bonds and dislocation movement from crack tips. Crack growth is not only induced by dislocation emission under applied stress, but also by the formation of micro-voids ahead of crack tips due to stress localization [21]. AIDE, therefore, contributes to cleavage-like fractures as well as dimpled intergranular fractures [22].

In summary, there is no unified theory accepted. To identify the dominant mechanism of HE, the fracture path and mode must be extensively studied considering alloying design, microstructure, thermal conditions, imposed stress, and other factors. It is essential to understand and apply these models in explaining various HE phenomena. For example, the HELP model was used to explain the continuous cracking under tensile stress along the fusion boundary of dissimilar welds of nickel-based alloy 625 on steel [23]. Also, the combined effect of HEDE and HELP helps explain the implication of solute hydrogen on dislocation movements [2].

2.2.3   Environmental assisted cracking

Hydrogen induced cracking (HIC) is a type of hydrogen embrittlement in susceptible steels and often exists as a form of stepwise cracking under the absence of external tensile stress. HIC cracks are characterized by their parallel directions towards the steel surface (i.e., axial direction of pipe) [9]. Following absorbed atomic hydrogen in steel, the hydrogen atoms are trapped and recombine into hydrogen gas in weak internal interfaces such as inclusions and laminations [9]. Cracking can occur once the internal pressure at these locations reaches a critical value [9].

It is worth noting that blister cracks resulting from HIC can turn into stress-oriented hydrogen-induced cracking (SOHIC) under residual or applied tensile stress [9]. Similar to the formation process of step-like cracking, blistering cracks form a stacked array of cracks in the through-thickness direction [9]. SOHIC is included as a type of EAC instead of an alternative to HIC [9].

Sulfide stress cracking (SSC) is a type of hydrogen embrittlement in susceptible steels with the presence of tensile stresses and H_2S in the environment [24]. SSC cracks are characterized by their brittle manner and are perpendicular to the tensile stress (i.e., residual stress or external stress) [25]. SSC cracking starts from the hard section or tip of deep pits when the stress is beyond the yield strength and the fracture is usually arrested in the ductile area [25]. Kane and Cayard indicated that

the locations with high internal stress due to the high concentration of absorbed hydrogen atoms (i.e., grain boundaries, inclusions, and notches) are likely to be the initiation sites of SSC [9]. Figure 2.3 is a schematic of cracking morphology in high and low strength steel. Intergranular cracking is commonly observed in high strength steel (≥700 MPa), whereas low strength steels (≤700 MPa) predominately fail by transgranular cracking. A mixed path can be found in low strength steels in some cases [25].

Intergranular cracking   Transgranular cracking
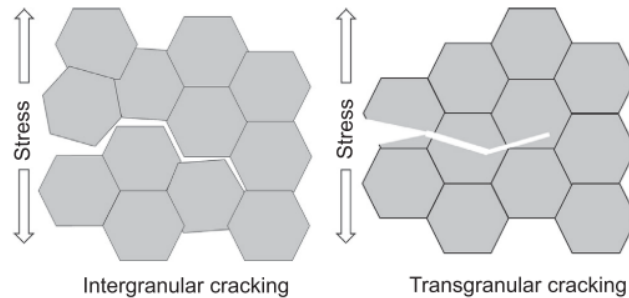
Figure 2.3. Cracking morphology of high strength steel on the LHS and low strength steel on the RHS [25].

2.3 Fundamentals of Austenitizing and Quenching

This section focuses on reviewing the microstructural development during the austenitizing and quenching process, as well as the role of alloying elements in the process.

2.3.1 Microstructural development during austenitization

Austenitization has a strong influence on the final properties of the structure of the materials, particularly due to the austenite grain size and segregation of alloying elements. To induce austenitization, the materials are heated from room temperature over its A_3 temperature. The A_3 temperature ranges from 820 °C to 850 °C for carbon steel with 0.25 wt% to 0.30 wt% C content according to the Fe-Fe$_3$C phase diagram (Figure 2.4) [26]. Three main features of austenitization are [27]:

1. Atom mobility and driving force for the formation of austenite increase with increasing temperature.
2. The nucleation and growth of austenite increase with increasing temperature.

3. A one-phase structure (austenite) with a more homogeneous carbon distribution replaces the previous two-phase mixture (ferrite + pearlite).

2.3.1.1 Austenite transformation

The role of the prior as-rolled P110 microstructure on the austenitization process is of interest. Capdevila and Caballero et al. concluded that the austenite formation starts at a higher temperature for coarse pearlite and that transformation rates are also slower for a microstructure with coarse pearlite [28]. The same conclusion was drawn by Mehl [29]. The mechanism is related to carbon diffusion being proportional to the interlamellar spacing of pearlite. V. Savran concluded that the ferrite to austenite transformation is a more rapid process than the pearlite to austenite transformation as it is an interface-controlled process [27].
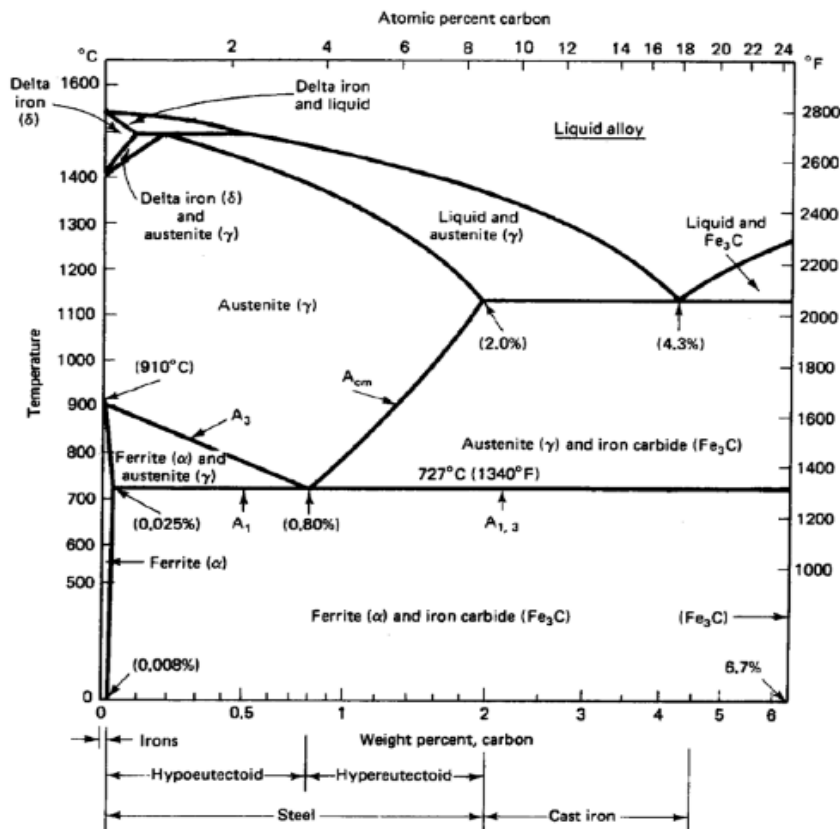
Figure 2.4. Fe-Fe$_3$C phase diagram, indicating the equilibrium phases as a function of carbon concentration (0.0 wt% to 6.7 wt%) and temperature [26].

The formation of austenite from proeutectoid ferrite and pearlite in hypoeutectoid steels was reviewed by V. Savran in detail [27]. During the heating process, pearlite regions with approximately 0.8 wt% C will transform to austenite first as the temperature reaches above eutectoid temperature. Dykhuizen et al. proposed that the ferrite will only start transforming after 10 vol% pearlite is transformed [30].. Summarizing, the transformation of a ferrite-pearlite mixture to austenite in low and medium carbon steel proceeds in the following steps [27].:

1. Pearlite to austenite transformation takes place. Because the C (carbon) diffusion rate is dependent on the effective diffusion distance, the growth of newly formed austenite is slightly slower if the inter-lamellar distance is larger.
2. Dissolution of the carbide creates a high-carbon austenite region (on the previous pearlite-ferrite grain boundaries).
3. The ferrite to austenite transformation happens, with carbon diffusing to the low-carbon austenite region.
4. Homogenization of carbon, as well as some alloying elements, takes place.

2.3.1.2 Prior austenite grain size

During the austenitizing process, the austenite grain size (AGS) before quenching influences the phase transformation kinetics during cooling, as well as the mechanical properties which are correlated with microstructure. The precipitation of alloy carbides or nitrides in austenite could also inhibit grain growth rate by a grain boundary pinning effect [31]. Thus, it is difficult to account for or model the precipitation phenomena while predicting AGS. Furthermore, austenite grain growth is generally suppressed by adding alloying elements due to the solute drag effect [32].

According to S. Lee and Y. Lee, the alloying elements can segregate towards grain boundaries as solutes, and the magnitude of drag effect on grain boundary movement is proportional to the difference the difference in atomic size between Fe and an alloying element (e.g., Molybdenum (Mo), Chromium (Cr), Nickel (Ni), Manganese (Mn), and Phosphorus (P)) [33]. For instance, Mo is more effective to inhibit grain growth than Cr or Ni at all austenitizing temperatures because of the higher difference in atomic radius between Fe and Mo (0.034 nm) than between Fe and Cr (0.01 nm), or between Fe and Ni (0.007 nm) [33]. Besides alloying elements, increasing C content was found to obstructing austenite grain growth [33]. By taking into account the dragging effect of

alloy elements as well as the carbon content, an empirical equation aimed to predict the grain growth during austenitization (particularly for temperatures from 800 to 1200 °C and time up to 3 hours) was proposed by S. Lee and Y. Lee [33].

$$d = 76671\exp(-\frac{89098+3581C+1211Ni+1443Cr+4031Mo}{RT})t^{0.211} \quad \text{(Equation 2.5)}$$

where the unit for the alloying elements added is in wt%. In the equation, it is clear that the Mo addition has the most dominant effect on AGS followed by C. Additionally, temperatures have a larger effect in increasing the growth rate of austenite grain than time according to Equation 1.5. Similar experimental and numerical investigations of austenite grain growth as a function of time and temperature have been widely reported [34,35,33,36,37].

2.3.2 As-quenched microstructure

During the quenching process, the face-centered cubic (FCC) crystal structure of austenite transforms by shear into the body-centered tetragonal cubic (BCT) crystal structure of martensite without the loss of its contained C atoms [38]. Thus, the retained C inside the BCT structure makes martensite supersaturated with C and stretches the BCT structure slightly so that it is no longer cubic.

The hardness of martensite is a function of the carbon content of the steel. As shown in Figure 2.5, the hardness of as-quenched martensite increases linearly from 0 to 0.5 wt% C content. It is also clear that the hardness values drop when the C content of the steel is higher than 0.8 wt%. This is due to the inevitable presence of retained austenite (RA) due to the low M_s of higher carbon steel, where RA is a relatively soft micro-constituent [39,40]. Theoretically, appreciable quantities of retained austenite exist only for steels with C > 0.4 wt% [41].
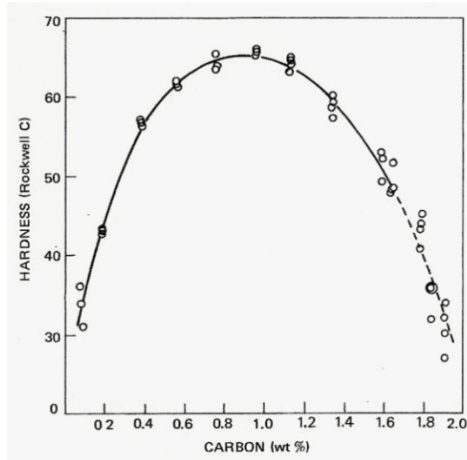
Figure 2.5. Hardness of as-quenched martensite as a function of carbon content [39].

Brine (95% NaCl solution), water, and oil are three conventional quenching mediums [42]. Their approximate cooling rates are 220 °C/s, 130 °C/s, and 50 °C/s, respectively [42]. Under circumstances where the quench rate and the steel's hardenability are sufficient for full hardening, the types of martensite structure are dependent on the carbon content of the parent austenite [39]. Figure 2.6 illustrates the relationship between the type of martensite, carbon content, and martensite start temperature for Fe-C steels. Lath martensite tends to form from parent austenite with C contents less than 0.6 wt%; it exhibits higher toughness and ductility, but lower strength [39]. In comparison, plate martensite tends to form from steels with C higher than 1.0 wt% and it produces higher strength, but low ductility [39]. Parent austenite with C content between 0.6 to 1.0 wt% produces a mixture of the two morphologies. For low carbon steel, the high martensite start temperature (M_s) makes the formation of cementite possible during quenching. This phenomenon is referred to as auto-tempering or self-tempering. To prevent the formation of cementite by C atom diffusion, the final temperature should be suppressed below M_s. Conversely, increasing the C content significantly lowers the M_s and (M_f). Thus, a sufficient magnitude of cooling is required to completely convert austenite to martensite. Most alloying elements decrease the M_s temperature, particularly Mn and Ni. The following empirical equation predicts the M_s as proposed by S. Pashangeh et al [43]:

$$Ms\ (°C) = 539 - 423C - 30.4Mn - 17.7Ni - 12.1Cr - 7.5Mo \qquad \text{(Equation 2.6)}$$

Figure 2.7 shows the typical morphology of lath and plate martensite using optical microscopy (OM). The typical feature of lath martensite is that the martensite crystals form parallel to one another within blocks and packets, whereas plate martensite consists of non-parallel martensite crystals. Both lath and plate martensite require the use of an electron microscope for complete resolution.
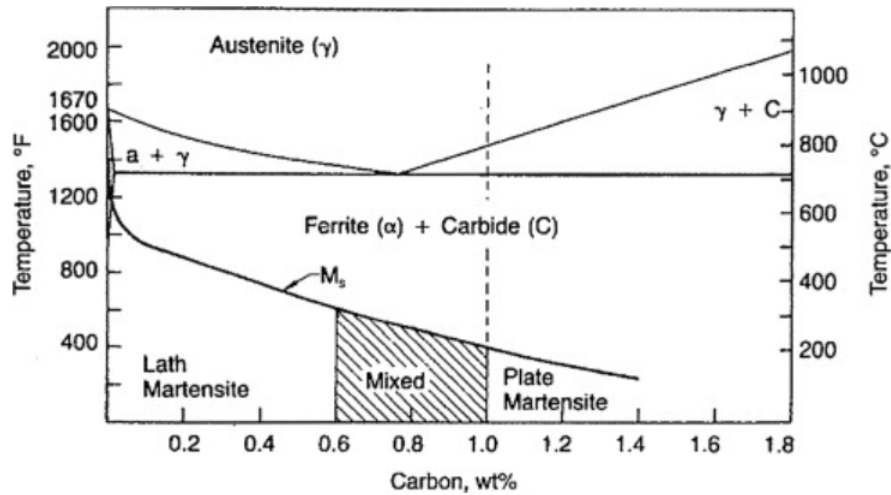
Figure 2.6. M_s temperature and martensite morphologies as a function of carbon content [44].
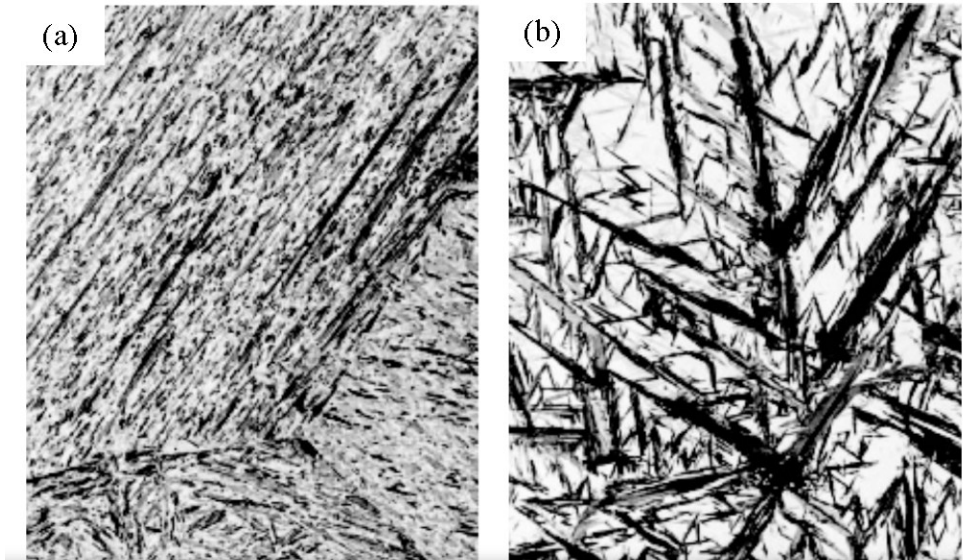
Figure 2.7. Martensite microstructure (low optical micrograph) (a) lath martensite and (b) plate martensite [45].

2.4 Fundamentals of Tempering

Tempering of martensitic steels can involve the decomposition of retained austenite, segregation of C, the precipitation of carbides, and the recovery and recrystallization of the martensite structure. The microstructural developments during the tempering process are complex and concurrent. This section reviews the processes involved during the tempering of as-quenched steels and the role of alloying elements.

2.4.1 Classification of tempering stages

For low and medium carbon steel, the super-saturation of C atoms and the presence of alloying elements in martensite crystals, as well as the high density of dislocations, provide opportunities for C atom segregation and carbide precipitation. There is a high driving force for ferrite recovery and recrystallization during tempering [46]. The transformations occurring during tempering of ferrous martensite are summarized in Table 2.1 [47]:

Table 2.1. Stages of tempering [44, 47].

T/ °C	Transformation	Remarks
25-100	Carbon segregate to dislocation/GBs	Pre-precipitation clustering
100-200	Transition carbide precipitation (<2nm)	Fe_2C, $Fe_{2.4}C$
200-350	Retained austenite (95%) transforms to ferrite/Fe_3C	Tempered martensitic embrittlement
250-350	Lath-like Fe_3C precipitation	N/A
350-550	Segregation of impurity/alloying element	Temper embrittlement
400-600	Recovery of dislocation substructure Lath Fe_3C agglomerates	Lath structure maintained
500-700	Alloy carbides Secondary hardening	Fe_3C may dissolve
600-700	Recrystallization and grain growth Cementite coarsening into spheroidal Fe_3C	Recrystallization is significant in low C steel Equiaxed ferrite formed

Prior to the tempering process, the austenitization heat treatment creates a relatively uniform dispersion of C and alloying elements. The identification of the first tempering stage is the carbon segregation and the precipitation of very fine transition carbides at a temperature between 100 to 200 °C [47]. In the second stage of tempering, the retained austenite transforms into a mixture of ferrite and cementite between 200 to 350 °C. The cementite tends to form along the inter-lath plates between martensite laths [47]. The morphology of the cementite plates is detrimental to fracture toughness and responsible for tempered martensite embrittlement [47]. The third stage of tempering starts from the formation of Fe_3C within the martensite laths, where transition carbides are replaced by Fe_3C [47]. With an increase in temperature, Fe_3C spheroidizes, and coarsens following an Ostwald ripening mechanism, where small particles merge into large particles to minimize the surface to volume ratio [48]. The heating rate affects the dispersion and refinement of Fe_3C [49]. For example, T. Furuhara found the refinement of Fe_3C by imposing more rapid heating during tempering [49]. In the fourth stage of tempering, particularly from 600 to 700 °C, the steel matrix also experiences drastic changes: [1] The fine martensite lath boundaries and random dislocations are eliminated (i.e., recovery) and [2] high angle parallel boundaries arrange and form equiaxed ferrite grains (i.e., recrystallization) of martensite [47]. It is worth noting that alloying elements can postpone the stages and kinetics of recovery, recrystallization, and grain growth due to the pinning action of carbides on the boundaries [47].

2.4.2 Effect of alloying elements and secondary hardening

Transition elements such as Cr, Mo, Niobium (Nb), Titanium (Ti), and Vanadium (V) are normally added to steel, and they act as strong carbide formers during tempering. During the early stages of tempering, C atoms redistribute to and precipitate at sites close to inter-lath boundaries, PAG boundaries, and dislocations to lower their chemical potential [41]. At higher temperatures (i.e., normally higher than 500 °C), the higher diffusion rates of these elements facilitate the rearrangement of these substitutional atoms [41]. The segregated alloying atoms can either form their own fine carbides or migrate to cementite particles [41]. Honeycombe proposed two mechanisms for the formation of alloy carbides [50]:

[1]   Separate nucleation and growth: alloy carbides nucleate heterogeneously at lath boundaries, PAG boundaries, and dislocations at the expense of cementite.

[2]   In-situ transformation: alloy carbides nucleate at cementite/ferrite interfaces, grow and eventually replace the host cementite.

During the alloy carbide transformation, much finer, dispersed, and more thermodynamically stable alloy carbides replace the previous coarse cementite. This fine, dispersed carbide morphology has a strengthening effect and contributes to the retardation of softening; it is referred to as secondary hardening [50]. Bain and Paxton reviewed the alloying elements and their hardening effects in detail [51]:

[1]   Silicon (Si), Ni, and Mn are not carbide formers. However, these elements largely dissolve into ferrite as substitutional solute atoms; therefore, they can raise the hardness of tempered steel by strengthening the ferrite. The strengthening effect of the elements follows the order of Si> Mn> Ni.

[2]   Cr and Mo are strong carbide formers. According to the illustration in Figure 2.8 (a) and (b), 0.5 wt% of both Cr and Mo additions is high enough for retarding softening. As shown in Figure 2.8, Cr retards softening but barely has a secondary hardening effect unless Cr is higher than 4 wt%. It is also clear that the secondary hardening effect from Cr addition is less prominent compared to the effect from the same amount of Mo addition.

[3]   It is worth noting that hardness evolution is not only dependent on alloying elements. For example, the rapid drop in hardness at high-temperature tempering range (i.e., over-tempered zone) is mostly attributed to the coarsening of cementite precipitates. Moreover, the recovery of the dislocation substructure could also play a role.
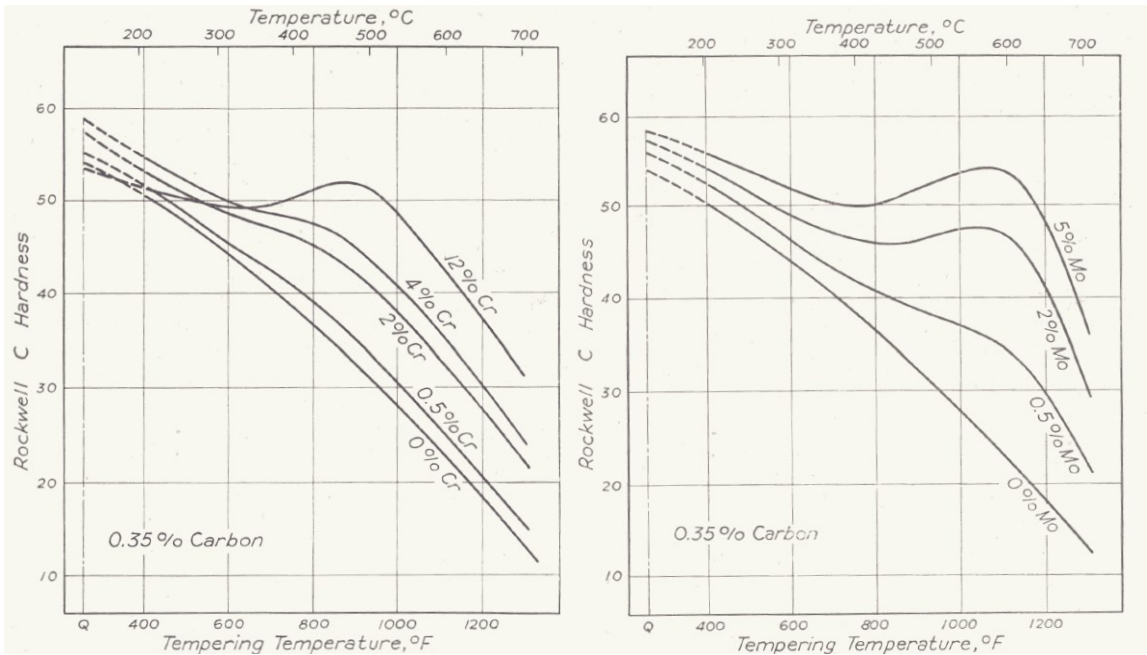
Figure 2.8. Secondary hardening of 0.35 wt% C steels with additions of (a) Cr and (b) Mo [51].

When the diffusion rates of Cr and Mo are high (e.g., when T>550 °C), the formation of the fine and dispersed Mo carbides has a higher effect in retaining the fine substructures and resisting coarsening and softening than Cr [47]. To evaluate the strengthening effect, it is important to define and predict the fineness as well as the volume fraction of precipitates. The volume fraction is related to the solubility of the alloy carbides in the austenite. Cr, Mo, and V tend to precipitate with a higher volume fraction in ferrite than Ti and Nb due to their relatively higher solubilities in austenite [47]. The fineness is related to the driving force for nucleation (i.e., magnitude of ΔG_N^o), while the free energy (ΔG_f^o) of formation of the precipitate is proportional to the ΔG_N^o. H. L. Schick summarised the enthalpies of formation of carbides, nitrides, and borides [52]. As shown in Table 2.2, precipitates with a fine and dispersed morphology, such as TiC, VC/N, NbC/N, have high heats of formation, whereas the coarse precipitates, e.g., Fe_3C, $Cr_{23}C_6$, MoC, and Mo_2C, have relatively low heats of formation [52]. Krauss indicated that the fine precipitates are all closed packed intermetallic compounds, while coarse precipitates have complex crystal structures [47].

Table 2.2. Enthalpies of formation of carbides, nitrides, and borides [52].

Enthalpy of formation at 298.15 K ΔH_f/KJ mol^{-1}
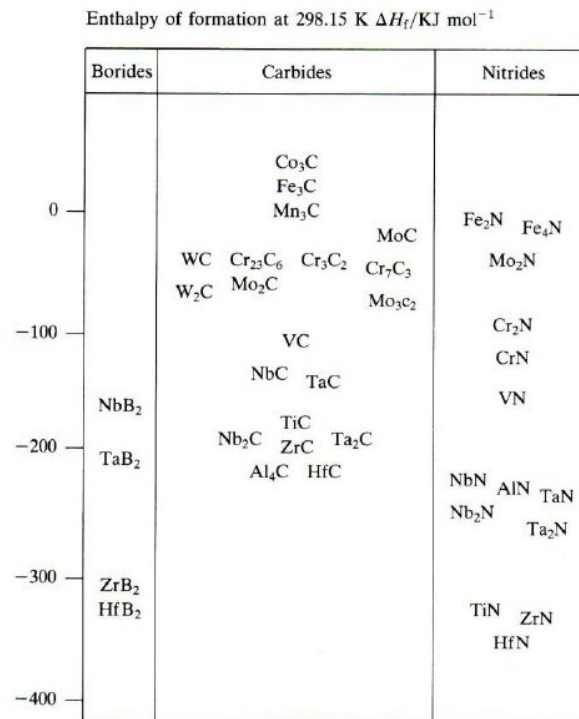
2.4.3 Time and temperature relationships in tempering

Tempering conditions should be carefully selected with awareness of the effects on temper embrittlement, residual stress, stress corrosion cracking, hardness, and toughness [53]. In addition, the selection of tempering conditions should be tailored to the carbon content as well as alloying chemistry [53]. Thus, in a conventional tempering process, there is a necessity to quantify the amount of tempering occurring in each heat treatment. The Holloman-Jaffe (HJ) parameter, also known as the Larson Miller parameter. It was proposed and developed by various authors (Holloman and Jaffe, 1945; Larson and Miller, 1952; Mendelson et al., 1965) and was used to relate time, temperature, and hardness [53]. The equation is described as:

$$\text{HJ parameter} = T(C + \log(t)) \qquad\qquad \text{(Equation 2.7)}$$

$$\text{Hardness} = f[\text{HJ parameter}] \qquad\qquad \text{(Equation 2.8)}$$

18

where T is the isothermal tempering temperature (in K), t is the holding time (in hours) and C is the Holloman-Jaffe constant that is dependent on steel composition. A value of $C=19.5$ is recommended by Holloman and Jaffe for application to carbon steels with 0.25 to 0.40 wt% C. In the absence of secondary hardening, the hardness can be linearly fitted as a function of HJ parameters [53].

The HJ equation was adapted to accommodate non-isothermal stages of tempering. The modified version of the HJ equation proposed by Tsuchiyama is shown below [54]:

$$P_n = T_n(logt_n + C) \qquad \text{(Equation 2.9)}$$

$$t_n = 10^{[(\frac{T_{n-1}}{T_n})(\log(t_{n-1} + C) - C]} \qquad \text{(Equation 2.10)}$$

$$T_n = T_{n-1} + \alpha\Delta t \qquad \text{(Equation 2.11)}$$

where T_1 is the starting temperature of the heating stage, t_n is the hold time of the nth period, t_{n-1} is total time from the first period to the $(n-1)^{th}$ period, α is the heating rate, T_n is the temperature at n^{th} period, and P_n is the HJ at the nth period. Figure 2.9 (a) and 2(b) illustrate that the modified HJ equation can predict the hardness after non-isothermal tempering more accurately than the conventional HJ equation [54]. This modified HJ equation can be effectively utilized for simulating the industrial/induction tempering process where higher heating rates and short holding times are used.

It is worth mentioning that the HJ parameters were developed to establish a relationship between tempering conditions and hardness for a specific alloyed steel under the assumption that the other mechanical properties, such as yield strength (YS) and ultimate tensile strength (UTS), also follow the same trend. V. Euser et al. reported that toughness cannot be linearly correlated with HJ parameters or hardness [55].
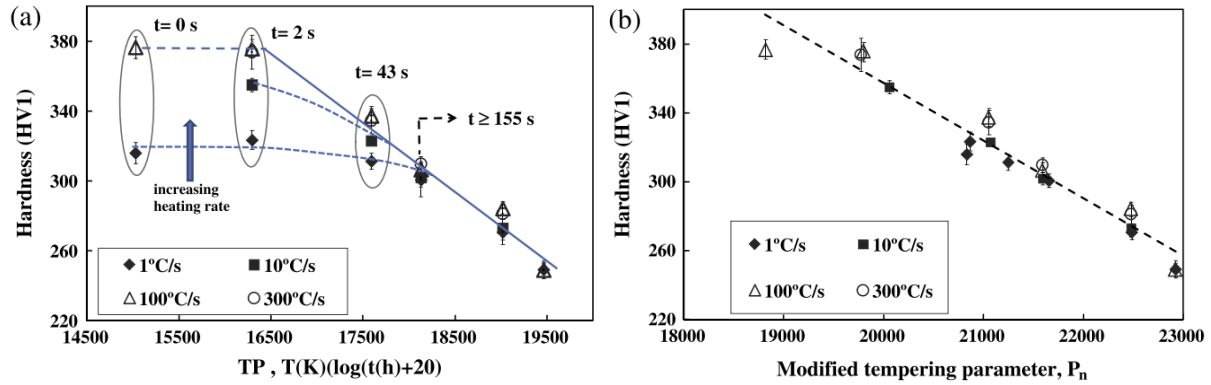
Figure 2.9. Plot of hardness vs (a) conventional HJ and (b) modified HJ parameters [54].

2.4.4 Cementite and alloy carbides

Various types of potential carbides with distinctive thermal stability in the Fe-Cr-Mo-Ti-C system could be present during tempering at different temperatures and times, namely M_2C, M_3C (alloyed cementite), M_7C_3, and $M_{23}C_7$. Depinoy et al. summarized the characteristics of these potential carbides, as shown in Table 2.3 [56]. Table 2.4 shows the crystallographic information of carbides.

Table 2.3. Carbide Characteristics in Fe-Cr-Mo-Ti-C [56,57].

Carbide	Morphology	Metallic Elements	Nucleation Site
MC	Globular	Ti, Mo	laths
M_3C	Globular, Rod-like, rhombus-shaped	Fe-rich with Cr	interfaces
M_7C_3	Rhombus-shaped, rod-like	Cr-rich with Fe	interfaces
$M_{23}C_6$	Fine Rod-like	Fe-rich with Cr	interfaces/laths

'Interfaces'' stands for prior austenite grain boundaries and lath boundaries, while ''laths'' stands for the matrix or dislocations.

Table 2.4. Crystallographic Structure of Potential Carbides in Fe-Cr-Mo-Ti-C [58,59,60].

Carbide	Space Group	Crystal System	a (A˚)	b (A˚)	c (A˚)	Datasheet
MC	Fm-3m (225)	Cubic	4.31	4.31	4.31	cF8
M_3C	Pnma (62)	Orthorhombic	4.53	5.08	6.74	oP16
M_3C	Pnma (62)	Hexagonal	4.77	4.77	4.35	hP8
M_7C_3	Pnma (62)	Orthorhombic	4.52	6.97	12.07	oP40
$M_{23}C_6$	Fm-3m (225)	Cubic	10.69	10.69	10.69	cF116

According to thermodynamic information, the predominant carbide formed at the initial tempering stage is M_3C. Depending on the Cr and/or Mo content and the tempering temperature and time, different carbides can then form after the precipitation of M_3C. M_7C_3 carbides are prone to form in steel containing high Cr content after prolonged tempering time (e.g., 0.12 wt% C-1.1 wt% Cr alloy steel) [61]. $M_{23}C_6$, as a type of equilibrium carbide, has been reported to form by replacing the M_3C (unstable) and M_7C_3 (metastable) [56]. $M_{23}C_6$ carbides can be promoted and stabilized by increasing the Cr and Mo content [3,56,61]. Additionally, it is generally accepted that both M_7C_3 and $M_{23}C_6$ carbides tend to form as Cr content increases in M_3C carbides [61,62]. Thus, decreasing Cr or Mo content to prevent the nucleation and coarsening of $M_{23}C_6$ carbide is feasible [3]. In contrast, M_2C carbides could precipitate independently in steel with a high Mo to Cr ratio during the early stages of tempering. M_2C carbides were found after tempering at 600 °C for 60 minutes and retained even after 6000 minutes of 0.6 wt% Cr-0.5 wt% Mo alloy steel [61]. It is worth noting that the behaviors of different carbides (e.g., precipitation sequence and thermal stability) are highly dependent on the alloying chemistry.

2.4.5 Carbide coarsening

The precipitation reaction consists of the three following stages: nucleation, growth, and coarsening. Nucleation is the formation of a new phase from supersaturated ferrite matrix [63,64]. The growth stage entails the diffusional transport of C atoms from the solid solution to pre-existing clusters; the size and volume fraction of the carbides increase at this stage. The coarsening stage involves the growth of large particles at the expense of the dissolution of small particles; this

phenomenon is referred to as Ostwald Ripening [63,4]. Theoretically, during the coarsening stage, the particle size increases with increasing tempering time or temperature while the equilibrium volume fraction is stable [63].

The characterization work by Nazemi et al. on cementite during tempering of low alloy, medium carbon steel illustrated the concepts of carbide coarsening [65]. Once supersaturation of alloying elements in cementite is reached, rod-like cementite particles begin to transform into spherical shapes, and small particles dissolve to aid coarsening of the larger idiomorphic particles [65].

Hou et al. summarized the volume fraction and number density of cementite particles in the Fe-C-Cr system with respect to tempering time at 700 °C [66]. As shown in Figure 2.10, the number density of carbides decreases whereas the volume fraction increases with increasing time. The volume fraction stops increasing and becomes constant at approximately 3 to 5 hours; cementite reaches an equilibrium state at 700 °C. Ju et al. observed that the change in number density and size becomes less prominent with longer tempering times (particularly from 4 to 6 hours) [4]. This was attributed to the smaller size difference and subsequent reduced driving force for coarsening according to the Ostwald ripening equation [4].
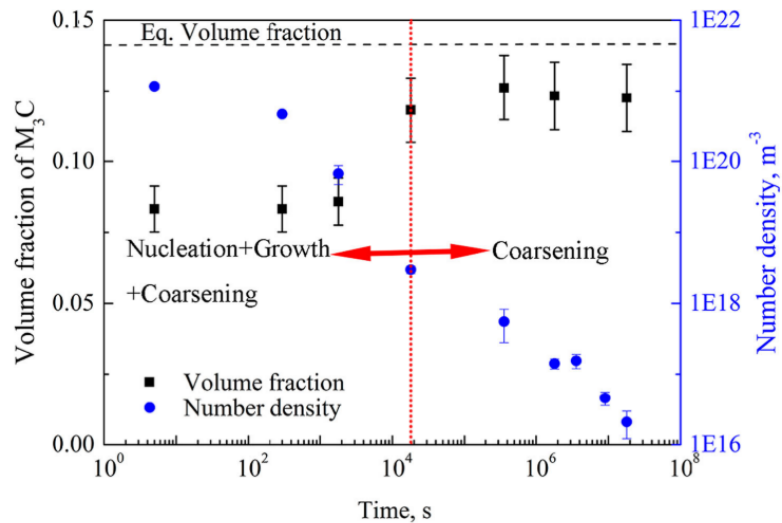
Figure 2.10. Experimental volume fraction and number density of cementite as a function of tempering time at 700 °C [66].

2.4.6 Elemental partition

The coarsening of carbides can be expressed by the Ostwald ripening equation [64]:

$$\overline{r_t}^3 = \overline{r_0}^3 + m^3 t \qquad \text{(Equation 2.12)}$$

where $\overline{r_t}$ is the average radius of the precipitate at time t, $\overline{r_0}$ is the average initial radius of the precipitate, m is the coarsening rate constant. It is worth noting that m is dependent on the mole fraction of alloying elements as well as the carbon content. The rate constant m can be expressed as [64]:

$$m = \frac{8\sigma V_m^\theta}{9RT} DC_e \qquad \text{(Equation 2.13)}$$

where σ is the carbide-martensite interfacial energy, V_m^θ is the molar volume of the precipitate phase, C_e is equilibrium solute concentration (i.e., C concentration), D is the diffusion coefficient of the coarsening rate-determining element, and R is the universal gas constant [67]. According to Björklund et al., as the precipitate size (i.e., r) reaches a specific large size, the coarsening rate is controlled by the slow diffusing substitutional alloying elements [67]. Generally, in the case of cementite, the C content is still the dominant factor for m [68]. In other words, the coarsening of cementite is controlled by C diffusion from ferrite. However, for $M_{23}C_6$, Cr is the rate-determining element for m, followed by Mo and Mn [68]. Therefore, the coarsening of $M_{23}C_6$ mostly occurs in medium and or high Cr alloyed steel (with more than 1.0 wt% Cr content).

The alloying elements can be divided into two types based on their segregating behavior. Elements with relatively higher solubility in cementite, such as Mn, Cr, and Mo, are segregating elements, while elements with negligible solubility in cementite, such as Si and Al, are anti-segregating elements [69]. Y. Wu et al. summarized the behavior of these elements in cementite. After prolonged tempering time or tempering at high temperature, segregating elements (i.e., Cr, Mn, and Mo) tend to partition to cementite and reach an equilibrium, whereas anti-segregating elements (i.e., Al and Si) are rejected from cementite [69]. Both types of elements influence the kinetics of cementite precipitation from various aspects. For segregating elements, the high interfacial Mn content in cementite reduces the C activity between the dissolving and the coarsening carbides, which restrains the carbon flux for cementite coarsening [69,70,71]. Cr and Mo are expected to have the

same effect as Mn [69]. However, no experimental evidence of the effect of Cr or Mo concentration in cementite on retarding the cementite coarsening was found. It is interesting to note that the anti-segregating elements (i.e., Al and Si) are commonly observed to initially enrich in cementite, and gradually rejected from cementite after prolonged tempering time [72]. In addition, Si was found to have a retardation effect on cementite precipitation by the formation of a Si layer outside the cementite during the growing stage [73,70].

2.5 Metallurgical Factors for Sour Service Performance

This section reviews the metallurgical features affecting the sour service performance of a Cr-Mo alloy steel, including martensite fraction, prior austenite grain size, elemental segregation, and carbide morphology.

2.5.1 Effect of microstructure on sour service performance

The metallurgical factors influencing sour service performance are well established [2,3,74,75,76,77,78]. A fully martensitic structure with minimal elemental segregation is the preferred microstructure [3]. According to Asahi et al, a higher fraction of martensite transformation leads to an improvement in SSC resistance [74]. The segregation of alloying elements could induce the formation of undesirable phases (e.g., large precipitates and inclusions), which adversely affect the material properties. Furthermore, high strength and toughness, as well as superior SSC resistance, were obtained by tempering at high temperatures [2,75,76]. This can be attributed to the combined effect of the dramatic decline in dislocation density and the precipitation of fine carbides and/or carbonitrides [2]. Finally, a fine PAG grain size was shown to improve the toughness and SSC resistance (by inhibiting inter-granular cracking) [77,78].

2.5.2 Effect of carbide morphology on sour service performance

The interaction of hydrogen atoms with precipitates in the presence of external stress is another key metallurgical factor affecting the sour service performance. The effect of precipitation is not only limited to material strengthening but also is effective in decreasing the sensitivity to H related failure. The presence of fine (<30 nm) carbides can improve the HE resistance by trapping hydrogen at the coherent precipitate/matrix interface. A gradual increase in carbide size leads to a

decrease in coherency and subsequent H trapping ability [79]. The most commonly found nano-sized particles, such as TiC, VC, (Ti, Mo)C, and NbC, exhibited strong hydrogen trapping ability [80]. Besides the coherency and size of precipitates, their distribution and number density also affects sour service performance. Hutchinson et al. indicated that an increasing number of finer precipitates enhances the H trapping capacity and improves the strength via dispersion strengthening [81]. Wang et al. proposed that the semi-continuous and coarse carbides located on grain boundaries facilitate intragranular cracking under external stress, whereas refined and dispersed precipitates enhance the hydrogen trapping ability [5]. Lastly, the shape of the precipitates can affect sour service performance. For example, lenticular M_3C formed along GBs have a detrimental effect on SSC resistance [3]. This adverse effect can be mitigated by V addition combined with high-temperature tempering, where the lenticular M_3C develop into more uniformly distributed and spheroidized morphology [3].

Numerous studies have focused on the effect of carbide morphology on sour service performance in Cr-Mo alloy heat treatable steel [3,5,56,68,82]. The effects of M_2C, M_3C, M_7C_3, and $M_{23}C_7$ carbides on sour service performance are summarized as follows:

[1] M_3C can easily grow at elevated temperatures at PAG boundaries and lath boundaries. This can lead to inter-granular cracking and poor SSC resistance [3]. The coarsening of M_3C mainly depends on C diffusion rather than the partition of Cr and Mo elements. It is difficult to limit coarsening simply by modifying Cr and Mo content [68]. Thus, strict control of cementite coarsening through heat treatment is a key point for the targeted industrial application.

[2] Fine (<50 nm) and homogeneously distributed M_2C carbides normally precipitate during the early stages of tempering (<650 °C). They tend to grow upon further heating at higher temperatures or prolonged holding time [56]. Dépinoy et al. reported that M_2C carbides lose their stability and start to dissolve at temperatures higher than 700 °C [56].

[3] M_7C_3 and $M_{23}C_7$ are metastable and equilibrium carbides, respectively. Both can grow with increasing temperature and time, in particular $M_{23}C_7$ [56]. Reduced Cr and Mo content can prevent their formation and restrain their coarsening [3]. The addition of W or V is also useful in suppressing the carbide coarsening [5].

2.6   Summary and Research Significance

From the above literature review, considerable knowledge and understanding have been generated over the last century with the development of high strength, low alloy (HSLA) casing steel, particularly during the past two decades. P110, as one type of the HSLA casing steel, has been widely used in mild sour service (H_2S) at operating temperature $> 80°C$ in downhole applications. The development of P110 was motivated by the need to withstand high mechanical loads and resist HE at the same time. The metallurgical design for P110 is a tempered martensite structure with a fine grain size and martensite packet size. However, there is the issue that a casing steel possessing good strength is accompanied by poor HE resistance. It has been suggested that by optimizing the alloying design and quenching and tempering (Q&T) heat treatment conditions, a specific type of resultant carbide morphology is expected to achieve both high strength and superior sour service performance.

Thus, numerous fundamental studies have been conducted on revealing the relationship between carbide morphology, alloying composition, and Q&T conditions. In particular, carbide size and shape refinement by additions of V and W have been widely studied. It also has been suggested that Mn, Si, and Al additions can limit cementite coarsening during the tempering process. Another route of modifying carbide morphology is by restraining the precipitation of unwanted carbide types. For example, Cr content was reduced to 0.5 wt% to inhibit the precipitation of coarse $M_{23}C_6$ (detrimental to SSC resistance) [82]. Assuredly, the carbide refinement discussed above cannot be achieved without strict control of tempering time and temperature.

Previous investigations proposed that the addition of Cr may have some retardation effect on cementite coarsening to some extent, and the C content is directly related to the equilibrium volume fraction of the cementite precipitates during tempering. Therefore, it is of interest to determine whether the morphology of tempered carbides can be affected by only adjusting the Cr and C content, as well as tempering conditions. In addition, there is still no systematic study investigating the sour service of high strength Cr-Mo alloy steel, particularly a steel with low Cr (< 1 wt%) and medium C (0.25 to 0.40 wt%) content.

This study aims to evaluate the effect of Cr and C content on microstructural evolution and precipitation behavior, and to correlate them with steel mechanical properties. To quantitatively reveal the effect of Cr and C content on the tempered carbide morphology, a series of Q&T heat treatments with a wide range of temperatures and times were conducted. Emphasis was put on investigating the precipitation and elemental segregation of tempered P110 using scanning transmission electron microscopy (STEM). The next Chapter of the thesis will introduce the details related to materials, experimental methods, and thermodynamic calculations used in this study.

Chapter 3

Materials and Methodologies

In this Chapter, information on the chemical composition of the P110 steels investigated in this work is reported. This is followed by a description of the laboratory quenched and tempered heat treatments conducted. Then, the metallographic sample preparation, microstructure characterization, mechanical testing, and thermodynamic simulation are detailed.

3.1 Materials

Four different low alloy P110 casing steels, two as-rolled plates and two quenched pipes, were studied. The focus of this work is on the as-rolled plates. Information on the industrial quenched pipes is provided in Appendix A and B. Two compositions of plate were studied (Table 3.1) and are subdivided into high (0.77 wt%) and low (0.52 wt%) Cr contents. The other alloying elements are similar in both cases; however, the carbon content of the high Cr group is slightly higher.

Table 3.1. Chemical composition (wt%) of casing steels reported by the manufacturer.

Materials	C	Mn	Cr	Mo	Ti	B+N+S+P	Ca+Si+Cu+Ni
Low Cr Pipe & Plate	0.255	0.46	0.52	0.188	0.03	0.013	0.71
High Cr Pipe & Plate	0.278	0.46	0.77	0.19	0.027	0.0018	0.68

3.2 Quenched and Tempered Heat treatment

Austenitizing and quenching (A&Q) heat treatments were performed on as-rolled plate (i.e., 0.52 wt% and 0.77 wt% Cr plates) using a Thermo Scientific Thermolync benchtop muffle furnace. The austenitizing temperature is constant at 950 °C, while the holding time is 15, 30, 60, or 90 minutes. Each austenitization process was followed by water quenching. After cooling, the A&Q plates were prepared for metallographic characterization.

The tempering heat treatment was performed on laboratory A&Q plates (i.e., 0.52 wt% Cr and 0.77 wt% Cr plates) using the same furnace used previously for austenitization. The tempering temperature ranged from 550 °C to 715 °C, while the time ranged from 15 minutes to 6.5 hours. Once the isothermal tempering stage was completed, the samples were air-cooled followed by metallographic sample preparation. Figure 3.1 shows a sketch of the industrial hot rolling and subsequent laboratory heat treatment routes.
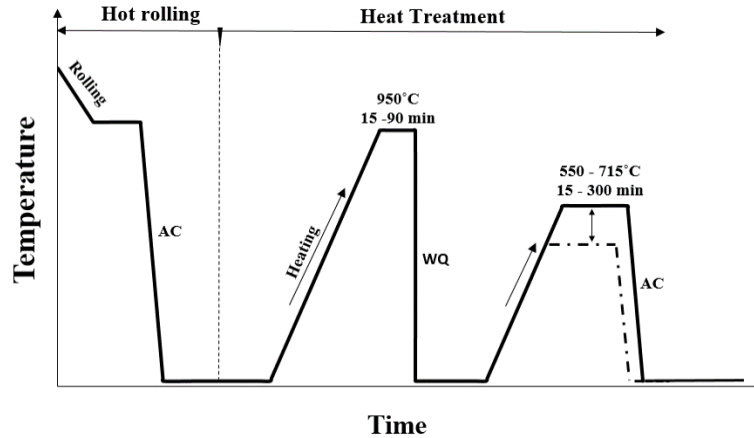
Figure 3.1. Sketch of hot rolling and subsequent A&Q&T heat treatment routes.

3.3 Sampling and Characterization of P110 Steels

This section introduces the methods for sample selection, preparation, metallurgical characterization, mechanical testing, and thermodynamic calculations.

3.3.1 Metallographic sample preparation

The location and orientation of all the samples are described in Figure 3.2. The rolling direction-transverse direction (RD-TD) surface at the ¼ thickness was taken for scanning transmission electron microscopy (STEM) and x-ray diffraction (XRD) examination. The rolling direction-nominal direction (RD-ND) surface was taken for optical microscopy (OM), scanning electron microscopy (SEM), electron microprobe analysis (EMPA), electron backscatter diffraction (EBSD), and prior austenite grain (PAG) observations.
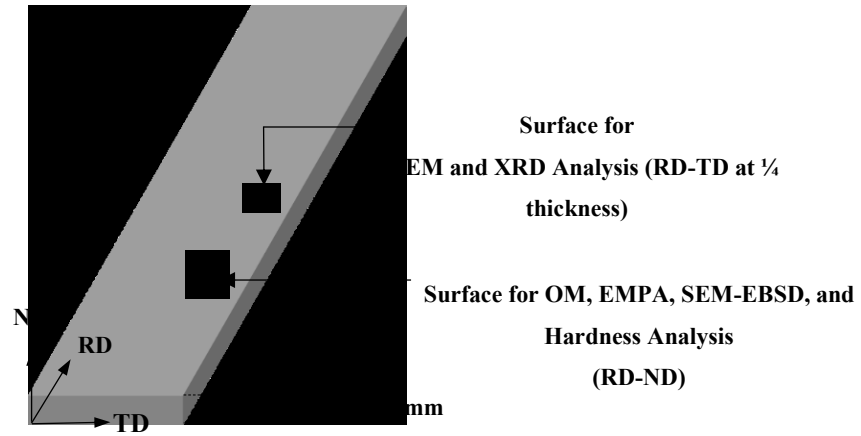
Figure 3.2. Locations in the as-rolled plate where metallurgical specimens were taken.

The required surface finish and etching details are shown in Table 3.2. Metallographic specimens were prepared using a Buehler Ecomet and Automet 250 auto polisher. Specimens were mounted in epoxy using 2.5 mm diameter molds, followed by grinding using silicon carbide grinding papers and mechanical polishing with a series of water-based diamond suspensions from 6 to 0.25 μm. Polishing using 0.05 μm alumina and 0.02 μm colloidal silica was needed for EBSD and TEM carbon replica sample preparation. The etching procedure for each technique is discussed in detail in the following sections.

Table 3.2. Metallurgical specimen preparation specifications.

Technique	Objective	Surface Finish	Etching
Vickers Hardness	hardness measurement	0.25 μm	N/A
XRD	phase identification	0.25 μm	N/A
EMPA	segregation characterization	0.25 μm	N/A
Optical Microscopy	microstructure observation	0.25 μm	2-3% Nital, immersion 10-60 s
	PAG observation	0.05 μm	Saturated picric + HCl + wetting agent, swab etching at 70°C
SEM w / EDS	microstructure and precipitation observation	0.05 μm	2-3% nital, immersion 10-60 s
EBSD	microstructure and phase observation	0.02 μm	2-3% nital, immersion 10-60 s
STEM	precipitation characterization	0.05 μm	3-5% nital, immersion 40-60 s

3.3.2 Microstructure and phase characterization techniques

3.3.2.1 X-ray Diffraction (XRD)

A Bruker D8 Discover diffraction system equipped with a copper source and a high throughput LynxEYE 1-dimensional linear detector was used to identify, as well as to quantify, the retained austenite in A&Q specimens. The RD-TD surface at the ¼-thickness location of the skelp was polished to 0.25 μm before XRD analysis. A fixed divergence silt, 0.3°, was set for all the XRD analysis. A step scan size within the 2θ interval angles of 20° to 110° at 1°/minutes rotating rate was performed.

3.3.2.2 Electron Microprobe Analysis (EMPA)

A CAMECA SX100 EMPA was used to map and quantify the chemical concentration distribution of the alloy elements in P110 as-rolled plates and A&Q plates. For clear elemental analysis, the RD-ND surface of the skelp was polished to 0.25 μm. The polished and un-etched surface was then coated with a carbon film before examination in the EMPA.

The parameters used during EMPA X-ray mapping and points scans are described in Table 3.3. An area of 1000 μm × 300 μm was mapped for all samples. After mapping, point scans were performed at regular intervals in the regions of interest on the EMPA map, where the scan spacing between two points was set as 10 μm. Each EMPA data point can provide five different elemental compositions. In this study, three carbide forming elements, Cr, Mn, and Mo, were measured and analyzed.

Table 3.3. Applied parameters during EMPA X-ray mapping and point scans.

Experimental Conditions	X-ray mapping	X-ray points scan
Current (nA)	200	100
Voltage (kV)	20	10
Beam size (μm)	Fully focused beam (<1 μm)	Fully focused beam (<1 μm)
Pixel size (μm)	10 × 10	N/A

Two methods were used for the quantification of elemental segregation, segregation ratio (*S.R.*) and partition coefficient (*k*). After obtaining the elemental concentration as a function of position, the segregation ratios of a specific measured element were calculated using Equation (3.1):

$$S.R. = \frac{\text{Measured Concentration (wt\%)}}{\text{Nominal Concentration (wt \%)}} \qquad \text{(Equation 3.1)}$$

Based on the measured concentrations from the point scans, partition coefficients of the measured elements were also calculated. The detailed procedure is shown in Appendix C.

3.3.2.3 Optical Microscopy

An Olympus BX61 microscope along with StreamMotion software were used in this study. To reveal the microstructure of as-rolled and as-quenched conditions, the polished specimens (i.e., polished to 0.25 μm) taken at the ¼ thickness location were lightly etched by immersing into 2-3% Nital (nitric acid in ethanol) for 10-60 s.

Both polarized light microscopy and bright field optical microscopy techniques can be used to delineate prior austenite grain boundary (PAGBs). In this study, the Olympus BX61 microscope was used. To reveal the PAGBs, the specimens were first polished to 0.05 μm. The polished specimens were then immersed into a hot 100 ml saturated aqueous picric acid solution at 70 °C along with 0.5 g wetting agent (sodium dodecylbenzene sulfonate) and less than 1 ml HCl. The PAGBs were delineated using swab etching every 60 s after immersion. Depending on the specimen surface condition and the saturation of picric acid, the etching time can vary from 2 minutes up to 5 minutes. Quantitative measurements of PAG size were undertaken according to ASTM E112-13 (Standard Test Methods for Determining Average Grain Size) [83]. ImageJ software was applied to measure grain size using the circular intercept method. At least five images were used for average PAG size calculation for each sample.

3.3.2.4 Scanning Electron Microscopy (SEM)

A Zeiss Sigma field emission scanning electron microscopy (FE-SEM) with a 30 μm aperture and an accelerating voltage of 10–20 kV was used in this study. In-lens secondary electron (in-lens), secondary electron (SE), and backscattered electron (BSD) imaging modes were applied. The required surface finish for SEM w / EDS was 0.25 μm, whereas for EBSD the required finish was 0.05 μm.

3.3.2.5 Energy Dispersive X-ray Spectroscopy (EDS)

Energy dispersive X-ray spectroscopy (EDS) was used for accurate phase identification and fast elemental/phase mapping. This was achieved by integrating the FE-SEM with an Oxford Instruments X-Max^{N} 150 detector and Oxford AztecSynergy software Version 2.4 for data

acquisition and analysis. A 30 μm aperture and an accelerating voltage of 20 kV were applied for this application.

3.3.2.6 Electron Backscatter Diffraction (EBSD)

Electron backscatter diffraction (EBSD) was used for accurate phase identification and grain boundary characterization. This was achieved by integrating the FE-SEM with an Oxford Instruments NordlysNano detector and Oxford AztecSynergy software Version 2.4 for data acquisition. A 60 μm aperture, an accelerating voltage of 20 kV, and a tilt of 70 ° were applied for this application. EBSD scans were taken at a step size of 0.5 μm at several locations and magnifications to obtain representative images of the microstructure. The RD-ND surface of the P110 skelp was characterized. Data post-processing was conducted with Oxford Aztec Crystal software.

3.3.2.7 Scanning Transmission Electron Microscopy (STEM)

Scanning transmission electron microscopy (STEM) was performed on carbon replica samples. A representative schematic illustrating the process of carbon replica film preparation is shown in Figure 3.3. As indicated in Figure 3.3a and 3.3b, the as polished bulk material (i.e., polished to 0.05 μm) of the RD-TD surface at the ¼ thickness location was first etched by 3% Nital solution for about 30 s to remove some of the iron matrix to expose the precipitates. A thin carbon film (~8 *nm* thickness) was then evaporated onto the etched specimen surface using a Leica ACE600 Carbon/Metal coater, as shown in the Figure 3c. The carbon film was scored into 1mm square sections by a razor blade to fit the TEM sample holder. The thin carbon film, containing the precipitates, was then lifted from the surface by immersing into a 5% Nital solution, as shown in Figure 3.3d. The carbon film was transferred into a solution containing 50% ethanol and 50% deionized water to remove the Nital solution and contaminants. Finally, the carbon film was transferred into a bath of deionized water, where the carbon films can spread out, float, and transferred onto a 200 mesh copper grid with a 3 mm diameter.

STEM observations were made using a JEOL JEM-2100F transmission/scanning transmission electron microscopy (JEOL, Tokyo, Japan) operating at 200 kV. The chemical composition for the different precipitates was determined in STEM mode equipped with an EDS detector. The data

acquisition and analysis (i.e., maps and spectra) were completed in AnalysisStation on the EDX computer. The size distribution and density of precipitates were characterized using bright field (BF) imaging in TEM mode. The d-spacings, as well as fast Fourier transforms (FFT), were obtained from the captured images under high resolution TEM (HR-TEM) mode and STEM-BF mode. All the analyses, including selected area diffraction (SAD), d-spacings, inter-planar angles, and FFT, were completed using ImageJ software. ImageJ describes particles with irregular shapes by the longest and shortest diameters, perimeters, and equivalent spherical diameters.
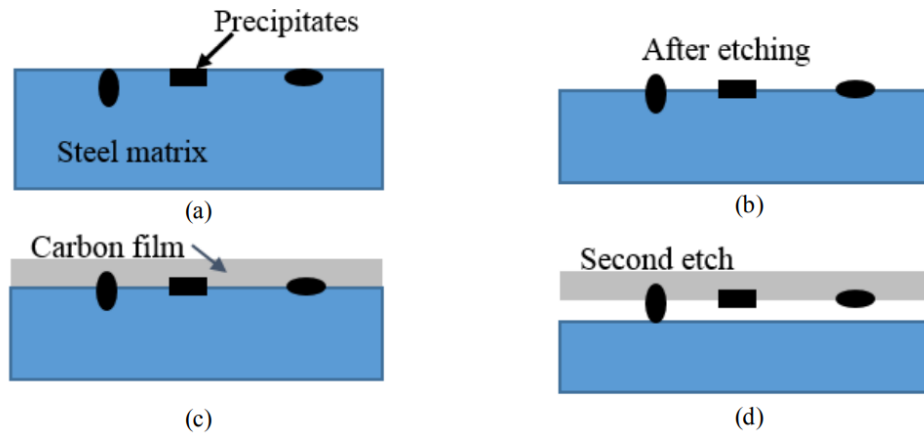
Figure 3.3. Sketches of carbon extraction replica film preparation process. (a) Prepared polished sample, (b) specimen after the first etch, (c) sample after depositing carbon film, and (d) sample after the second etch [84].

3.3.3 Mechanical testing

Mechanical testing methods, including micro-hardness and tensile testing, are described in this section.

3.3.3.1 Micro-hardness Testing

A schematic of the hardness matrix is shown in Figure 3.4. Micro-hardness measurements were performed on A&Q and Q&T plates using a Wilson VH3100 hardness tester with Minuteman software. A tested specimen with a 0.25 μm surface finish from the RD-ND surface was tested with a 2 kg force, and the dwell time for the hardness indenter was set to 10 s. The minimum spacing between hardness points was larger than 2.5 times the size of the indent to minimize

measurment errors. The size of each micro-hardness indent was automatically measured and converted into Vickers pyramid number (HV) by Minuteman software. Average hardness values were calculated based on a minimum of 30 indentations per sample.
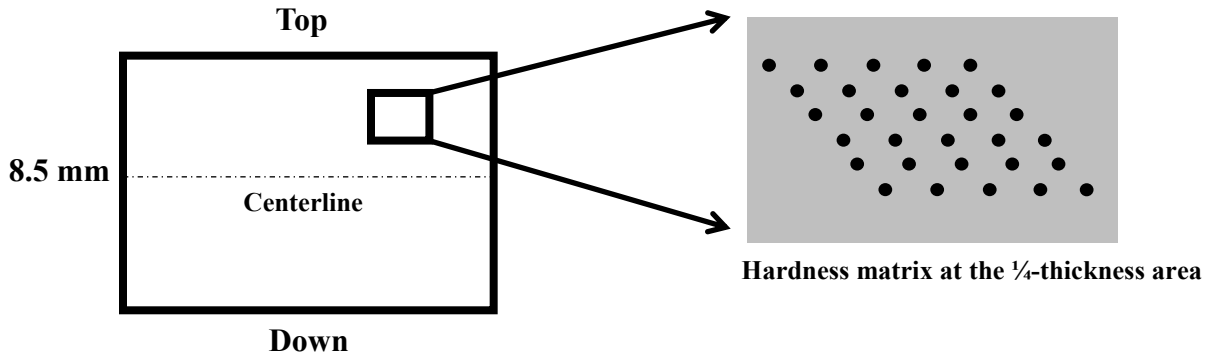
Figure 3.4. Schematic sketch of hardness matrix at the ¼ thickness area of the RD-ND surface.

3.3.3.2 Tensile Testing

Tensile specimens were taken from the longitudinal (parallel to the rolling direction) direction of the laboratory Q&T P110 plate. As shown in Figure 3.5, a longitudinal specimen with 5 mm thickness was machined from the middle of the wall thickness. Due to the limited thickness of the as-roll plate, sub-sized tensile specimens were selected and manufactured in accordance with ASTM E8/E8M (Standard Test Methods for Tension Testing of Metallic Materials) [85]. The sub-sized sheet type specimen along with the detailed specifications is illustrated in Figure 3.6.
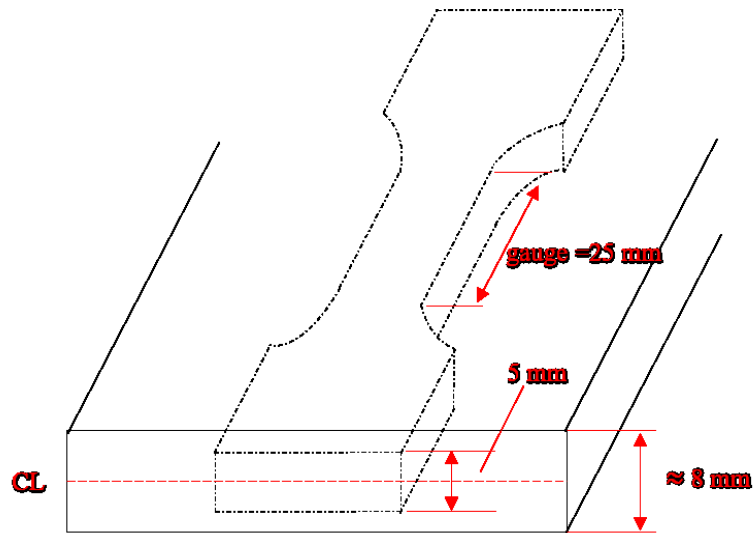
Figure 3.5. Schematic ketch of a sheet-type longitudinal tensile specimen at the ¼-thickness area in the plate.
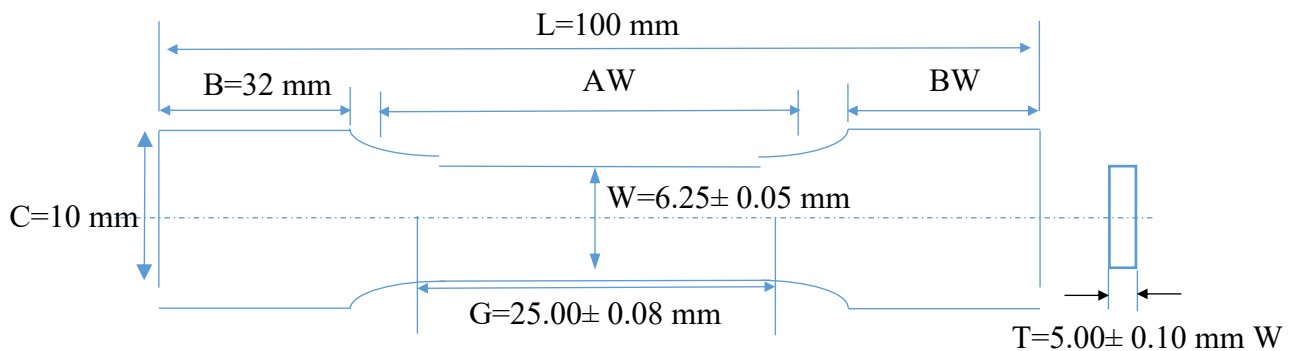
Figure 3.6. Specification of a sub-sized sheet-type tensile specimen.

The tensile test was performed on an MTS 810 Material test system with a 647 Hydraulic Wedge grip at a displacement rate of 0.5 mm/min. The tensile properties, including yield strength (YS) and ultimate tensile strength (UTS), of the Q&T specimens were obtained from the generated stress-strain curves. The YS was determined by the corresponding stress at 0.5% strain offset, while the maximum stress in the stress-strain curve was taken as the UTS. All tensile properties were taken to be the average of duplicate experiments performed for each specimen group.

3.3.4 Thermodynamic Simulations

ThermoCalc® 2020 was used to model the precipitation behavior during austenitization and tempering treatments. TCFE10 and MOBFE3 databases were used for all calculations. Two modules were used in this work; i.e., property model and phase diagram modules.

The property model simulation module was used for predicting driving forces for the precipitation of MC, M_3C, and $M_{23}C_6$ in P110 with the various Cr and Mo compositions at different temperatures. The driving force was defined as the difference in initial and final free energies (i.e., thermodynamic potential for the change). The phase diagram (binary, ternary, and multi-component) simulation module was used for predicting the types and amounts of equilibrium precipitation phases and the elemental partition during austenitization or tempering. It is worth noting that the equilibrium phase diagram is the result of thermodynamic calculations where the effects of kinetics were neglected in the calculation process. The slow diffusivity associated with the substitutional component (e.g., Cr and Mo) can retard the equilibrium coarsening kinetics for precipitation in ferrite. Additionally, the precipitation of tempered carbide (e.g., $M_{23}C_6$) is dependent on the diffusion of large solute atoms (e.g., Mo). Thus, the potential deviations between experimental characterization and thermodynamic simulation are taken into account during the discussion in Chapter 5.

3.4 Summary

The experimental techniques used for preparing, machining, processing, and analysis of P110 casing samples were detailed in this Chapter. The results obtained using the described techniques for the studied steels are presented in the Chapter 4 and Chapter 5.

Chapter 4

Characterization of As-rolled and Austenitized & Quenched Samples

In this chapter, the microstructural characterization of both the as-rolled plates and austenitized and quenched (A&Q) plates is presented. Specifically, measurements of elemental segregation using EMPA and OM were conducted on both the as-rolled and A&Q plates. Micro-hardness, X-ray diffraction (XRD), electron backscatter diffraction (EBSD), and scanning electron microscopy (SEM) analysis of the A&Q plate were also undertaken. Precipitation in the A&Q plates was characterized using scanning transmission electron microscopy (STEM). Based on the above analysis, an optimum A&Q heat treatment condition was determined.

4.1 EMPA Analysis of As-Rolled Plates

EMPA maps and point line scans were obtained at ¼ thickness locations of the 0.52 wt% Cr and 0.77 wt% Cr as-rolled and A&Q plates. The analysis location is shown schematically in Figure 4.1. The ¼ thickness area location was 1.5 mm below the top surface and 1.5 mm above the centerline of the as-rolled plates. The concentration distributions of Mn, Cr, Mo, Ni, and P were mapped by EMPA, but only the results of strong carbide forming elements, Cr and Mo, are discussed in this section.
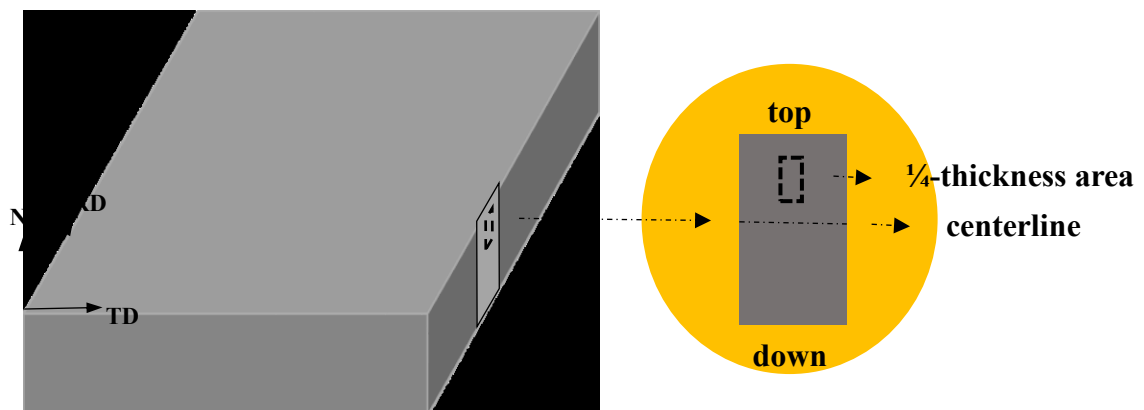
Figure 4.1 Schematic showing EMPA sample locations.

4.1.1 Cr and Mo analysis of the 0.52 wt% Cr sample

Enhanced grayscale maps for Cr and Mo for the 0.52 wt% Cr plate are shown in Figure 4.2. The enhanced grayscale maps were converted from original grayscale maps to visually enhance the difference between high concentration (dark color) and low concentration (white color) regions. The micro-segregation can be easily differentiated through the alternation of bright and dark colors. The dotted line in Figure 4.2 represents the location for the EMPA point line scan.
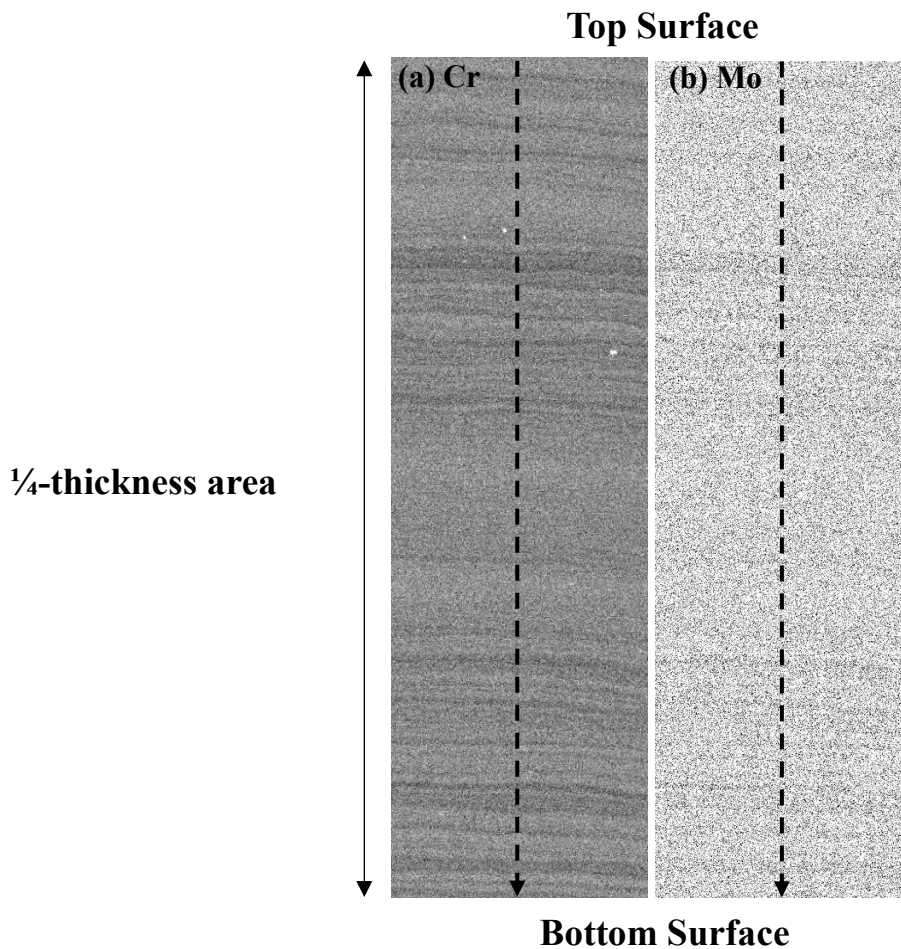
Figure 4.2. As-rolled EMPA enhanced maps for (a) Cr and (b) Mo for 0.52 wt% Cr plate.

Figure 4.3 shows the Cr and Mo concentration profiles obtained along the point line scan in the 0.52 wt% Cr plate. The maximum measured amounts of Cr (0.64 wt%) and Mo (0.27 wt%) from the line scan are significantly higher than the nominal values for Cr (0.52 wt%) and Mo (0.19 wt%).

By measuring the interpeak spacing across the 1000 nm analyzed region, an average interdendritic spacing of as-rolled 0.52 wt% Cr plate was estimated to be 43 ± 9 μm.
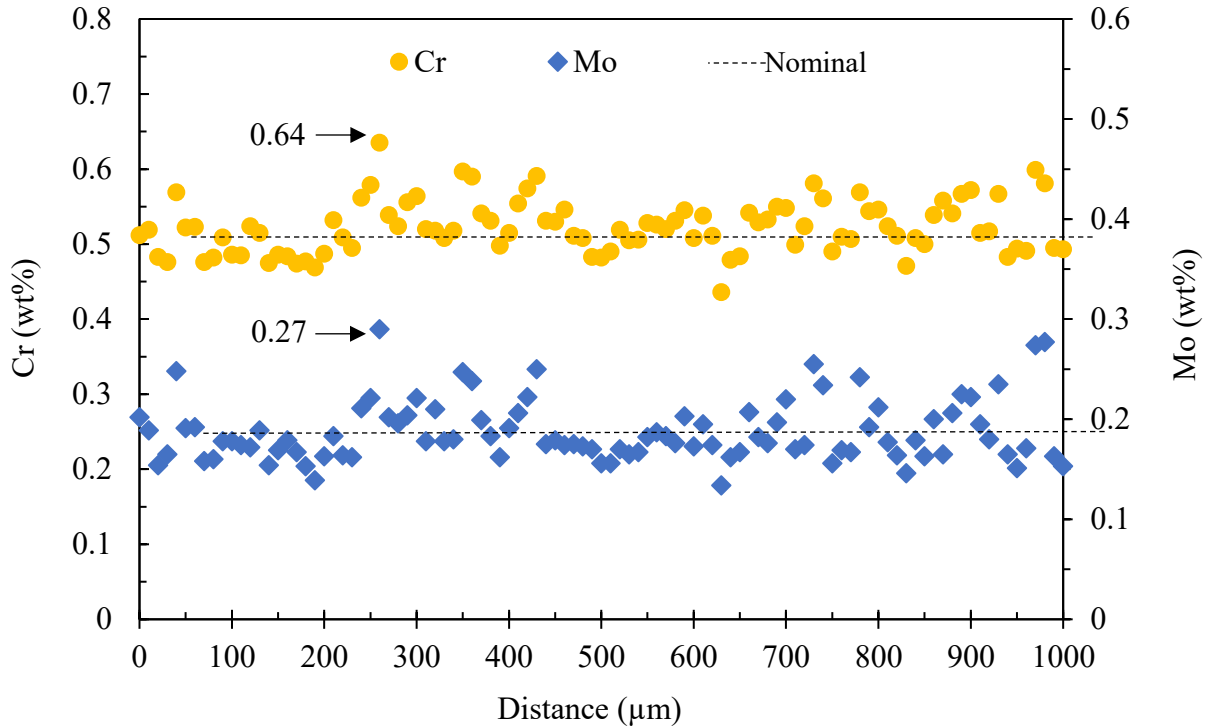
Figure 4.3. Cr and Mo point line scan for 0.52 wt% Cr plate.

A magnified view of the line scan (in the range of 300-500 μm) is shown in Figure 4.4. The peaks and troughs associated with the microsegregation are readily observed. The oscillations in the concentration of Cr and Mo overlap and they correspond to the changing local compositions of Cr and Mo in and between the dendrites. The amplitude of oscillation is proportional to the extent of microsegregation. Vertical dotted lines at each peak are marked and the distances between the peak locations are labeled as well. The Cr and Mo concentration profiles exhibit an oscillatory behavior with an interpeak spacing of 40 to 55 μm. The amplitude of the cyclic oscillation for Cr and Mo concentration is as high as 0.15 wt% and 0.13 wt%, respectively. Given that the nominal Mo content is 0.19 wt%, the cyclic oscillation amplitude of 0.13 wt% indicates a very high extent of Mo segregation.
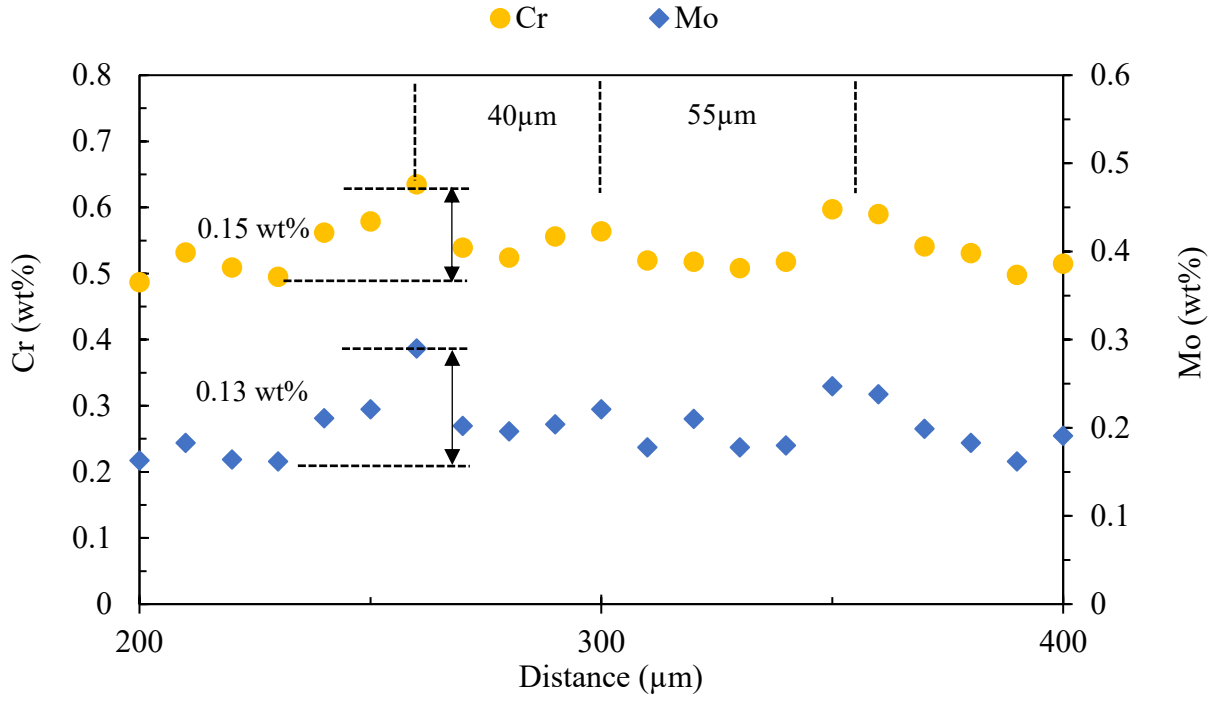
Figure 4.4. Magnified Cr and Mo wt% distributions across the point line scan for 0.52 wt% Cr plate.

4.1.2 Cr and Mo analysis of the 0.77 wt% Cr sample

Enhanced grayscale maps for Cr and Mo for the 0.77 wt% Cr plate are shown in Figure 4.5. The dotted line represents the location for the EMPA point line scan.
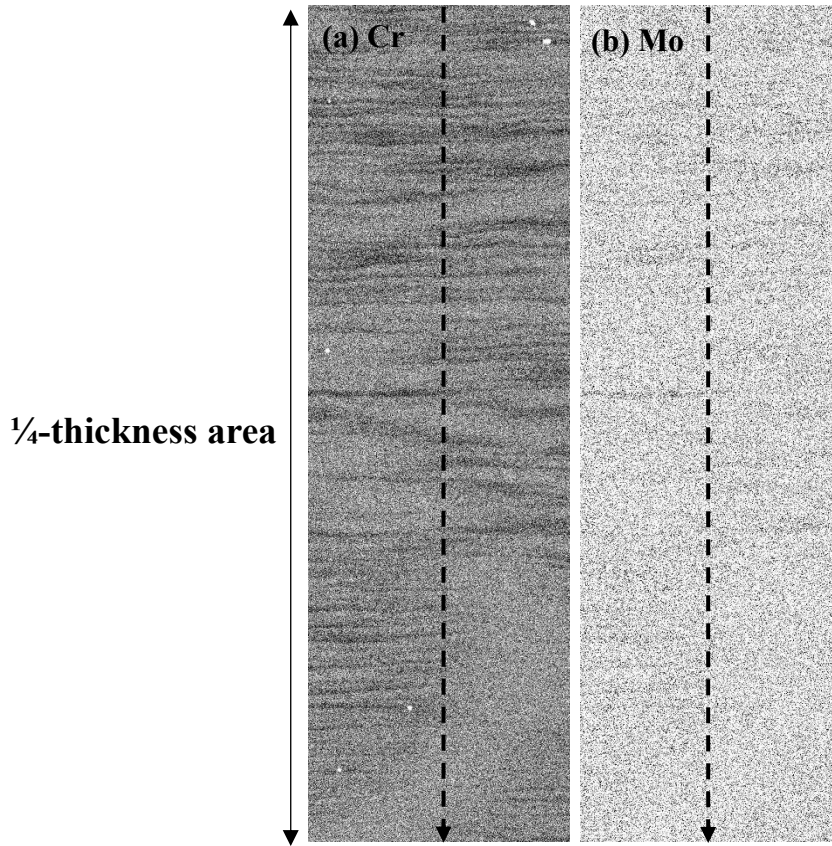
Figure 4.5. As-rolled EMPA enhanced maps for (a) Cr and (b) Mo for 0.77 wt% Cr plate.

Figure 4.6 shows the Cr and Mo concentration profiles obtained along the line scan in the 0.77 wt% Cr plate. The presented concentration profile for both Cr and Mo have a similar distribution as that for the as-rolled 0.52 wt% Cr sample. The maximum measured Cr (0.92 wt%) and Mo (0.30 wt%) from the line scan are significantly higher than the nominal Cr (0.77 wt%) and Mo (0.19 wt%) content. By measuring the interpeak spacing across the 1000 nm region, an average interdendritic spacing of as-rolled 0.77 wt% Cr plate was estimated to be 33 ± 11 μm. As expected, this spacing is smaller than the measured 43 μm for 0.52 wt% Cr plate, which can be attributed to the higher concentration of solutes (i.e., C and Cr contents).
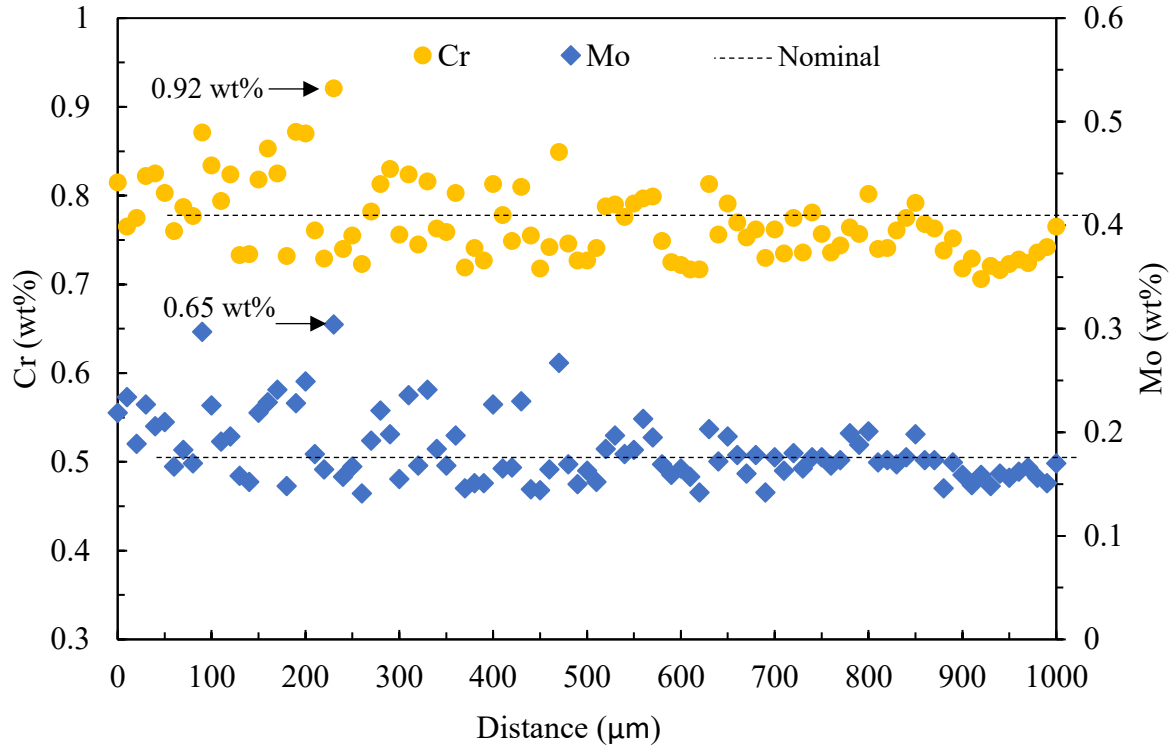
Figure 4.6. Cr and Mo point line scan for 0.77 wt% Cr plate.

A magnified view of the line scan (in the range of 100-300 µm) is shown in Figure 4.7. Vertical dotted lines at each peak are again labeled and the distances between the peaks are added. The Cr and Mo concentration profiles exhibit oscillatory behavior with scan distance. Interpeak spacings of 34, 36, and 40 µm are observed. The amplitude of the cyclic oscillation for Cr and Mo concentration is as high as 0.19 wt% and 0.12 wt%, respectively. The oscillatory amplitude for Cr wt% is slightly higher than the 0.15 wt% for 0.52 wt% Cr steels, which can be attributed to the higher nominal Cr wt%.
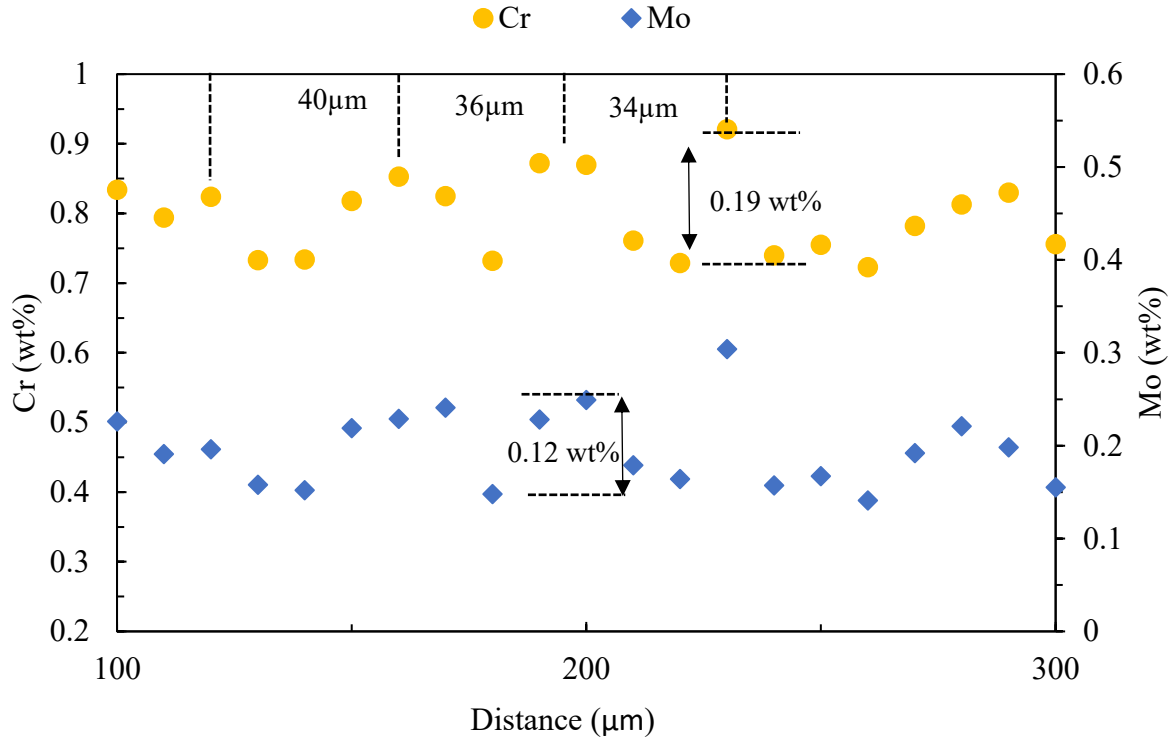
Figure 4.7. Magnified Cr and Mo wt% distribution across the point line scan in 0.77 wt% Cr plate.

4.1.3 Microsegregation ratios for Mn, Cr, Mo in as-rolled plates

The maximum segregation ratio (max S.R.), defined as the ratio of the maximum measured concentration wt% to the nominal concentration of an individual element, was used to quantify the extent of microsegregation of the two different as-rolled plates.

The calculated max S.R. from as-rolled 0.52 wt% Cr and 0.77 wt% Cr plates are shown in Table 4.1. Published works show that an increase in the nominal C content in steel results in increased segregation [86,87]. Thus, the measured max S.R. values for the 0.77 wt% Cr plate (i.e., 0.278 wt% C) were slightly higher than the 0.52 wt% Cr steel (i.e., 0.255 wt% C), except for Cr. It is worth noting that the maximum concentration value corresponds to the maximum measured concentration from the EMPA line scan, which may not reflect the actual maximum value on the EMPA map. Based on the measured max S.R. values of Mo, Cr, and Mn (Table 4.1), it can be concluded that the tendency to segregate follows the trend of Mo>Mn>=Cr.

Table 4.1. Max S.R. for Mn, Cr, and Mo in as-rolled 0.52 wt% Cr and 0.77 wt% Cr plates.

Plate	Mn	Cr	Mo
0.52 wt% Cr	1.22	1.22	1.55
0.77 wt% Cr	1.25	1.20	1.67

Both the measured concentration profiles (Figure 4.4 and 4.7) and the max S.R. values (Table 4.1) indicate that the nominal compositions cannot accurately reflect the actual compositions due to micro-segregation (in particular for Mo). This form of inhomogeneous distribution of Cr and Mo can affect precipitation formation. For example, localized regions with high Cr and Mo content can induce the precipitation of large $M_{23}C_6$ carbides (detrimental to SSC resistance) during tempering treatment [82]. Additionally, cyclic variations in concentration can also affect the consistency and accuracy of the TEM analysis. Therefore, the austenitization conditions should be carefully selected with regards to reduction in elemental segregation.

4.2   EMPA Analysis of Austenitized and Quenched Plates

In this section, EMPA analysis of the microsegregation of Cr and Mo in the A&Q treated plates is presented. A&Q heat treatments at 950 °C for 30 min were conducted on the 0.52 wt% Cr and 0.77 wt% Cr as-rolled plates. EMPA point scans were taken in the same location as the analysis conducted on the as-rolled plates (Figure 4.1). The EMPA data was quantitatively studied using the S.R. and the partition coefficient (k).

Figure 4.8 and Figure 4.9 show the calculated S.R. values for Cr and Mo obtained along the line scan in the A&Q 0.77 wt% Cr plate, respectively. Although the EMPA measurements performed on A&Q sample were different from the analyzed area for as-rolled sample, the trend of S.R. is still of some value. The S.R. profiles become less scattered after the A&Q treatment. In particular, the peak values of S.R. decrease dramatically with the maximum S.R. value for Cr decreasing from 1.20 to 1.10, and the maximum S.R. value for Mo decreasing from 1.67 to 1.39. The S.R. profile for Cr exhibited smaller overall values of S.R. compared with Mo, which can be attributed to the higher partition coefficient for Cr relative to Mo [88,89]. The A&Q 0.52 wt% Cr plate exhibited

similar segregation behavior as its 0.77 wt% Cr counterpart. As such, the plots for 0.52 wt% Cr plate (i.e., S.R.) are only included in Appendix C.
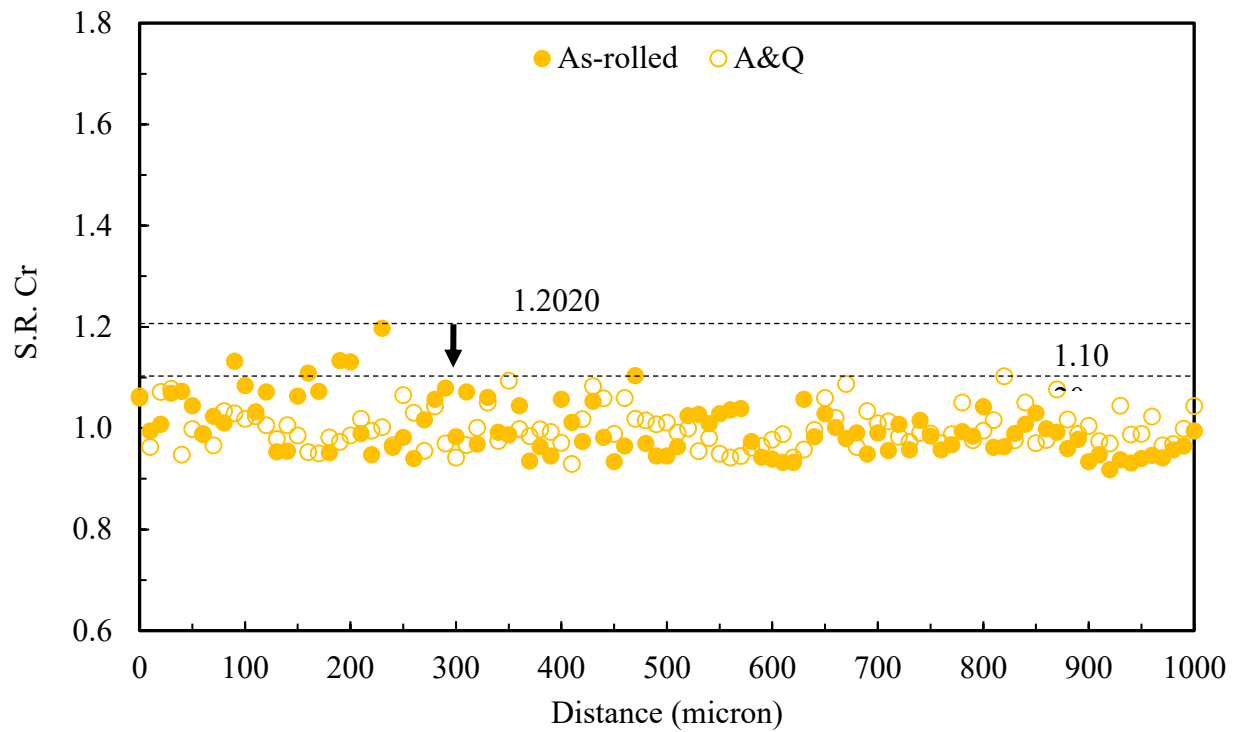
Figure 4.8. S.R. of Cr before and after austenitization (950 °C-30min) for 0.77 wt% Cr plate.
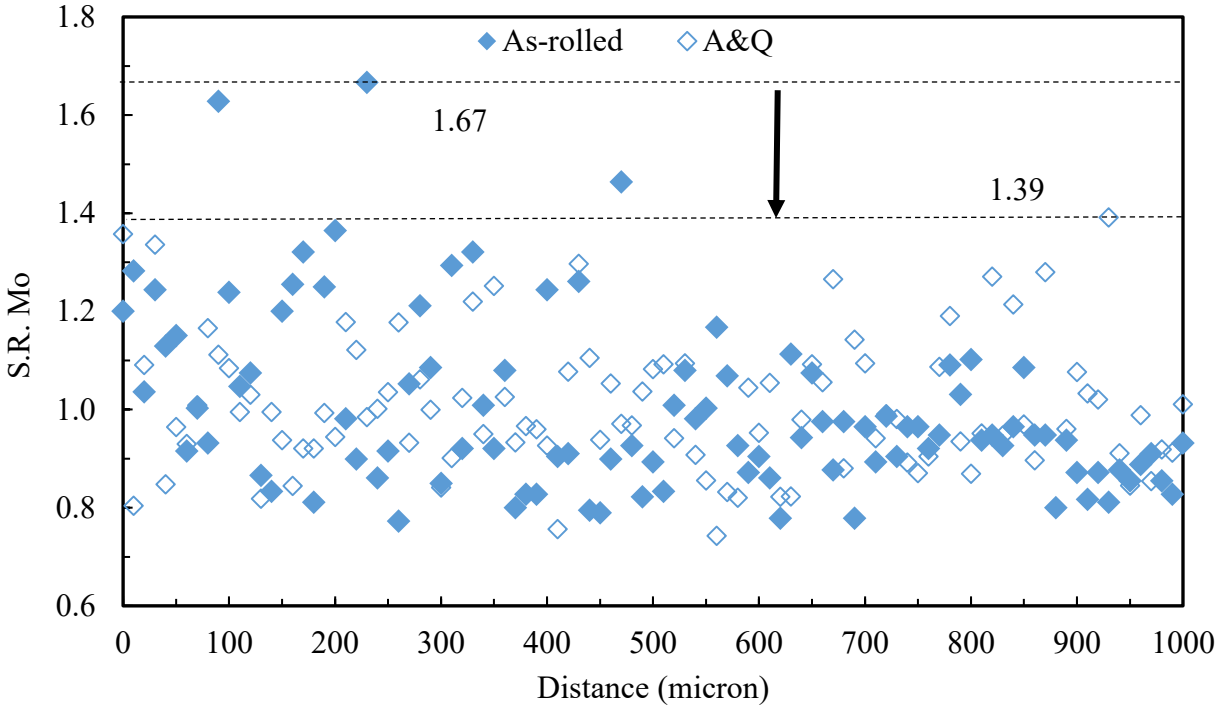
Figure 4.9. S.R. of Mo before and after austenitization (950 °C-30min) for 0.77 wt% Cr plate.

The calculated partition coefficients (k) for Cr and Mo for the 0.52 wt% Cr and 0.77 wt% Cr plates, before and after A&Q treatments, are summarized in Table 4.2. Appendix C2 shows a detailed example of the calculation. It is worth noting that the calculated k (often referred to as the pseudo-partition coefficient) for A&Q plates is not the actual k after solidification. In this experiment, the calculated k is simply used as a number to evaluate whether the austenitization at 950 °C for 30 min can affect microsegregation. A lower k ($k<1$) results in a higher degree of segregation and vice versa. Based on the calculated partition coefficient values, three conclusions were drawn:

[1] The 0.77 wt% Cr plate with a slightly higher nominal C wt% than the 0.52 wt% Cr plate does not display a higher extent of microsegregation in the as-rolled condition.

[2] The tendency to segregate follows the trend: Mo > Mn ≥ Cr. To explain why the extent of segregation for Cr is lower than that for Mn and Mo, Cr has the highest value of equilibrium partition coefficient (0.95) between BCC ferrite and liquid iron compared with Mn (0.84) and Mo (0.80) [90].

48

[3] Austenitization at 950 °C for 30 min reduced the extent of microsegregation for both steels. Mo experienced a higher degree of segregation reduction than Cr. The trend can be explained in terms of the higher diffusion coefficient for Mo in austenite than Cr [91].

Table 4.2. Partition coefficient for Mo, Mn, and Cr before and after austenitization (950 °C-30 min).

		k(Mo)	Increase in %	k(Mn)	Increase in %	k(Cr)	Increase in %
0.52 wt% Cr	As-rolled	0.852	↑ 2.30	0.930	↑ 0.80	0.935	↑ 1.07
	A&Q	0.871		0.938		0.945	
0.77 wt% Cr	As-rolled	0.836	↑ 4.54	0.922	↑ 2.23	0.945	↑ 1.69
	A&Q	0.874		0.943		0.961	

4.3 Metallographic Characterization of As-Rolled Plates

Optical micrographs of the as-rolled 0.52 wt% Cr and 0.77 wt% Cr plates at the ¼-thickness position are presented in Figure 4.10. The microstructure of the 0.52 wt% Cr plate consists of polygonal ferrite and large pearlite colonies. A banded structure was observed parallel to the rolling direction. In contrast, the 0.77 wt% Cr plate consists of much finer ferrite grain, acicular ferrite, and smaller pearlite colonies. The banded structure is more prominent compared to the 0.52 wt% Cr plates. Furthermore, some pearlite colonies formed a banded structure along the rolling direction.

Given the difference in initial microstructures between the as-rolled 0.52 wt% Cr and 0.77 wt% Cr plates, it is important to understand the effect of the initial structure on the kinetics of austenite formation. Published literature has shown that austenite transition rates are slower for microstructures with coarser pearlite, since the effective carbon (C) diffusion distance is proportional to the interlamellar spacing of pearlite [28]. Thus, assuming the pearlite structure of both steels have similar interlamellar spacing, the austenite transition rates are slower for structures with larger pearlite colonies (i.e., 0.52 wt% Cr plates). Dykhuizen et al. indicated that the ferrite will only start transforming after 10 vol% pearlite is transformed to austenite (i.e., until C is

available from the pearlite regions) [30]. Since it is difficult to directly measure the distribution of C in steel, OM and SEM characterization of as-quenched microstructure were undertaken to determine the effect of the difference in prior as-rolled microstructures on overall austenite transformation. The results are discussed in Chapter 4.4.
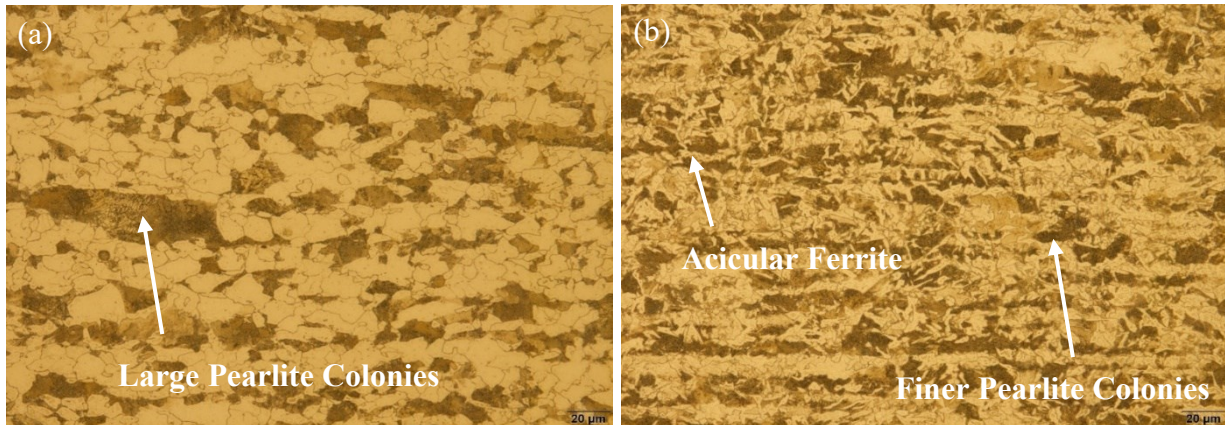
Figure 4.10. Optical micrographs of (a) 0.52 wt% Cr and (b) 0.77 wt% Cr as-rolled plates at ¼ thickness in the RD-ND plane.

4.4 Microstructural Characterization of A&Q plates

The ideal microstructure of casing steel for sour service application contains minimal elemental segregation (discussed in Chapter 4.2), maximum martensite transformation (i.e., low amount of retained austenite), fine prior austenite grain, and uniformly distributed fine precipitates. These metallurgical features can be obtained by optimizing A&Q conditions.

As-rolled 0.52 wt% Cr and 0.77 wt% Cr plates were austenitized at 950 °C for 15, 30, 60, and 90 min. OM and SEM characterization of the as-quenched martensite structure is presented. The effect of A&Q treatment on the amount of retained austenite was evaluated by micro-hardness, XRD, and EBSD. Based on the PAG size measurements, an optimum A&Q condition was determined. Finally, TEM characterization of the precipitates in the A&Q plates is presented.

4.4.1 OM and SEM analysis of as-quenched martensite

The morphologies of the as-quenched martensite for both 0.52 wt% Cr and 0.77 wt% Cr plates are shown in Figure 4.11 and 4.12, respectively. Two types of martensite morphologies were observed

in the lab-quenched plates: lath and lenticular (or plate-like) martensite. Only lath martensite was observed in the as-quenched 0.52 wt% Cr plates regardless of the austenitizing time. An example of lath martensite in the 0.52 wt% Cr plate quenched from 950 °C for 15 min is shown in Figure 4.11 (a). Figure 4.11 (b) shows an SE-SEM micrograph of martensite laths. Lath martensite can be distinguished by its parallel lath structure within packets or blocks (bundles of laths).

The quenched 0.77 wt% Cr plate was predominantly composed of lath martensite; however, some lenticular/plate-like martensite structure was also observed. This type of mixed microstructure is illustrated in Figure 4.12 (a), (b), and (c). Lenticular or plate-like martensite was identified due to its lens-shaped, needle-like structure. It is characterized by non-parallel and narrow plates or needles with length exceeding the packet size. As shown in Figure 4.12 (a), some regions are composed of alternating light and dark blocks. This observation indicates that the observed laths were formed at different orientations [92]. Furthermore, lenticular martensite consists of broken lines with a random breadth and various spacings between the lines as viewed in the SE-SEM [92]. An SEM micrograph consisting of a lenticular structure is shown in Figure 4.12 (d).
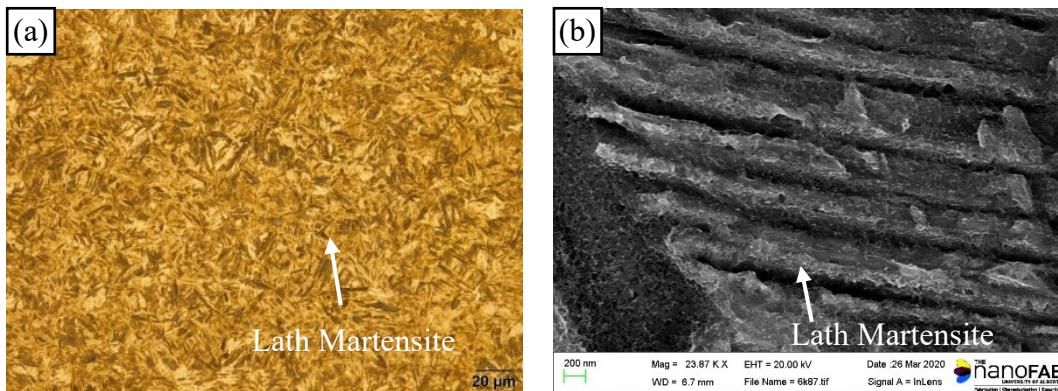
Figure 4.11. (a) Optical micrograph and (b) SE-SEM micrograph of as quenched 0.52 wt% Cr plate after heating to 950 °C for 15 min, showing martensite laths.
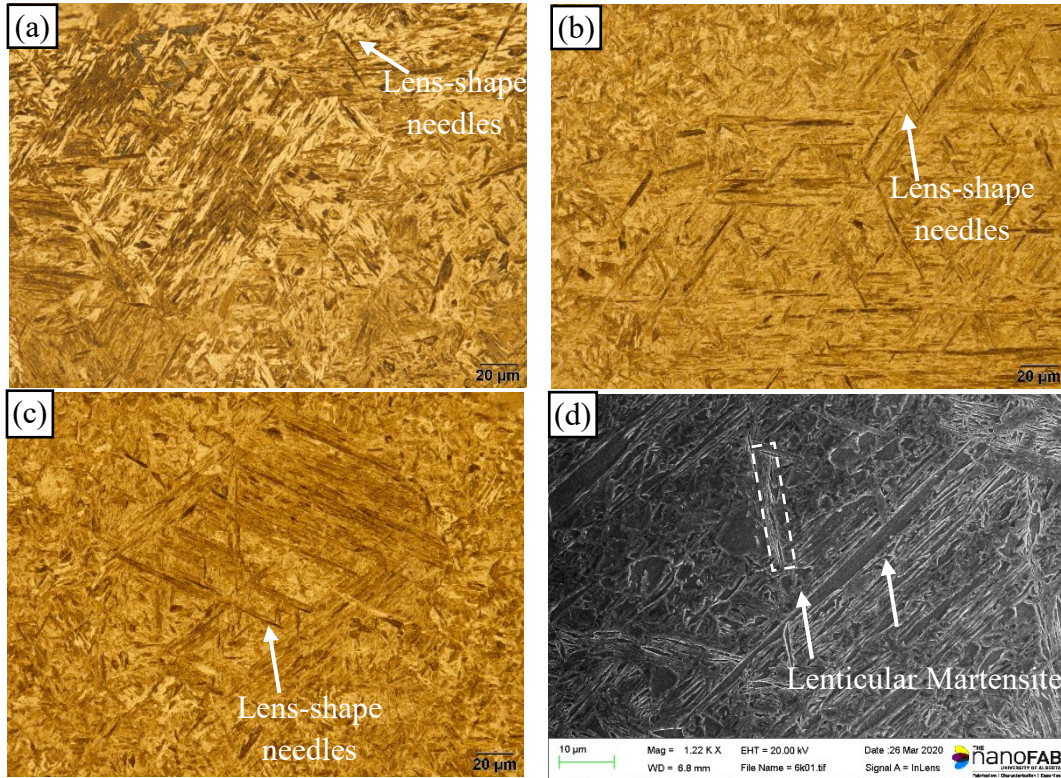
Figure 4.12. (a, b, c) Optical micrographs and (d) SEM SE micrograph of as quenched 0.77 wt% Cr plate after heating to 950 °C for 30 min, showing martensite needles and laths.

Lenticular martensite was observed in the quenched 0.77 wt% Cr plates (0.278 wt% C) regardless of austenitizing time (15 min to 90 min), but not in the quenched 0.52 wt% Cr (0.255 wt% C) samples. Published work has proposed that lenticular martensite generally forms at regions with higher carbon contents [92]. Specifically, Yuehui and Qiuhua et al. indicated the as quenched steel contains only lath martensite when C < 0.19 wt%, whereas quenched steel with 0.19 wt% < C < 0.40 wt% is composed of a mixture of lath and lenticular martensite [92]. Thus, the observed difference in martensite morphology in the experimental steels is due to the difference in nominal C content. The effect of Cr content on the martensite morphology is inconclusive.

Figure 4.13 (a) and (b) show SEM images of quenched 0.77 wt% Cr plate (950 °C for 30 min). Abnormally coarsened martensite structures (highlighted in white arrows) are observed. Similar coarse structures were observed in all the quenched P110 plates for different austenitization times. This coarse structure is referred to as coalesced martensite and is formed by the merging of two fine martensite plates with the same crystallographic orientation rather than the coarsening of a

single plate [77]. SEM micrographs of coalesced martensite obtained from published literature are shown in Figure 4.13 (c) and (d) [77].
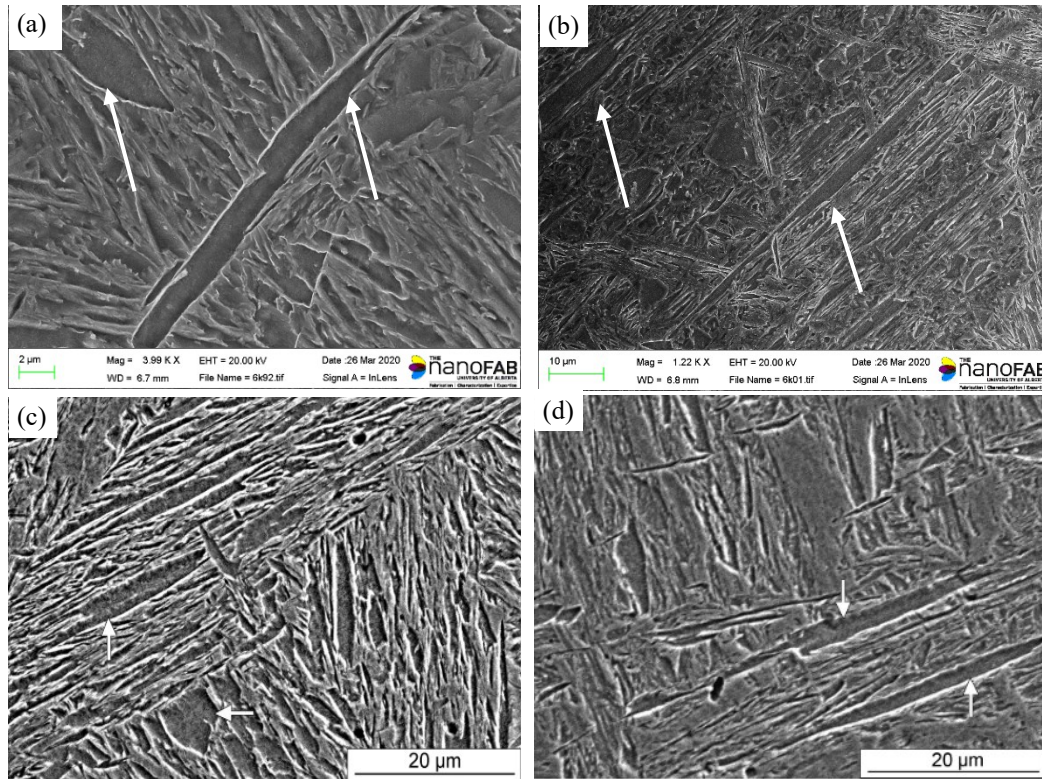
Figure 4.13. SEM SE micrographs of (a, b) as-quenched 0.77 wt% Cr P110 steels austenitized at 950 °C for 30 min and (c, d) as-quenched SA508 Gr. 3 steel austenitized at 1200 °C for 48 h, showing coalesced martensite plates [77]. The arrows indicate the regions or traces of coalesced martensite.

Pous-Romero and Bhadeshia reported that the coalesced martensite structure consists of thick crystallographically homogeneous grains, which can deteriorate the steel properties (particularly toughness) by initiating cleavage failure and promoting the propagation of cleavage cracks [77]. According to the literature, structure coarsening is inevitable during the quenching process; however, the dimension of the coalesced martensite plates can be significantly restrained by a small PAG size [77]. Therefore, the austenitization conditions should be strictly controlled to limit grain growth and to mitigate the detrimental effect of coalesced martensite on toughness.

In summary, lenticular martensite was identified in the as-quenched 0.77 wt% Cr steel as a result of higher nominal C content. No relationship between austenitization time (from 15 to 90 min) and as-quenched microstructure was identified. This indicates that 15 min of austenitization is sufficient to minimize the potential effects from the difference in initial as-rolled microstructures between steels. In other words, large pearlite colonies can fully transform into austenite with a relatively homogenized C distribution after heat-treating for 15 min; any prolonged austenitization beyond 15 min does not induce a prominent difference in the as-quenched microstructure.

4.4.2 Micro-hardness evaluation

Figure 4.14 shows the average micro-hardness values after austenitizing at 950 °C for different holding times. The study conducted by Prawoto and Jasmawati shows that as holding time increases from 1 h to 28 h, the micro-hardness of medium carbon steel decreases due to the continuous PAG growth [93]. However, for this work, no prominent relationship was found between micro-hardness and austenitization time or PAG size (Figure 4.14). Thus, the differences in PAG size after austenitization were too similar to be reflected in the hardness measurements.

Micro-hardness was used to estimate the fraction of martensite transformation during quenching. According to extensive hardness data from the literature, martensitic Fe-C alloy steels with 0.25 to 0.28 wt% C have hardness values ranging from 480 to 560 Hv [94]. The A&Q P110 plates exhibited comparable hardness values to the literature values (shaded band in Figure 4.14). This indicates that the as-quenched P110 sample consists of a structure with sufficiently high martensite transformation (i.e., a low amount of retained austenite).
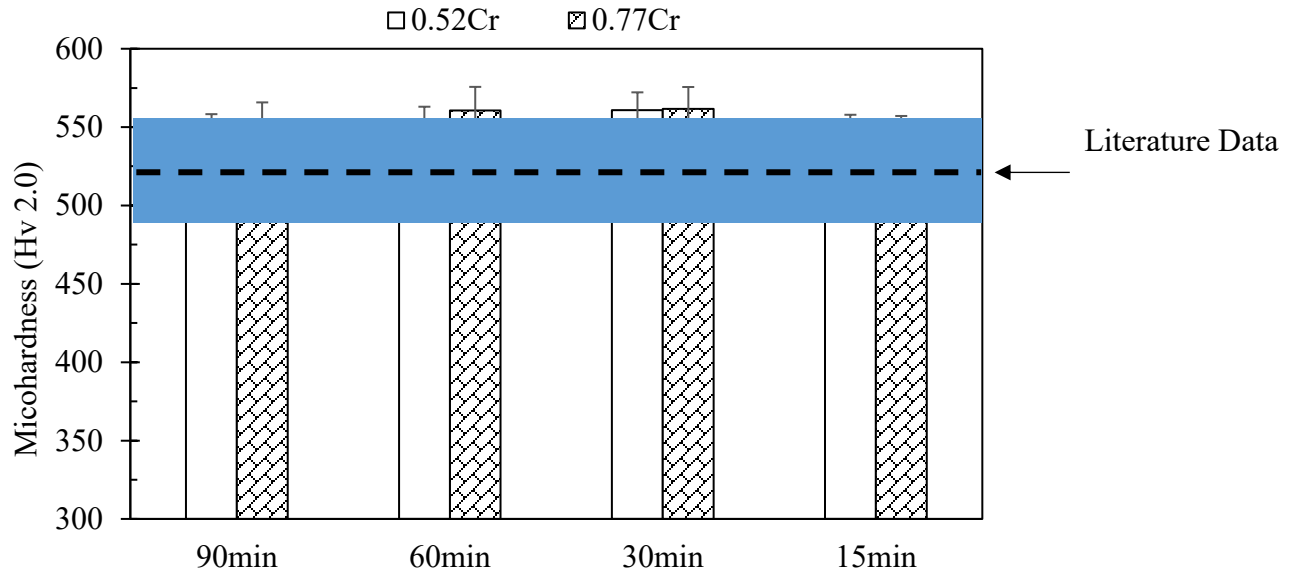
Figure 4.14. Micro-hardness of A&Q 0.52 wt% Cr and 0.77 wt % Cr plates as a function of austenitizing time. Error bars represent the standard deviation based on 30 measurements per sample.

4.4.3 Phase identification by XRD

To verify the laboratory quenching practice, XRD analysis was conducted to detect and quantify the presence of retained austenite (RA) of the as-quenched 0.52 wt% Cr and 0.77 wt% Cr steels (950 °C for 15 min).

The peaks for the ferritic phase (martensite) and RA were identified in XRD patterns, as shown in Figure 4.15. The ferritic phase is most dominant in the as-quenched state, The (111) peak of retained austenite, which theoretically is highest in intensity, can barely be seen. Based on the methods provided by Jatczak, the RA volume fractions were quantitatively determined using the measured integrated intensity values from XRD [95]. 0.5 vol% of RA was identified in both quenched steels.
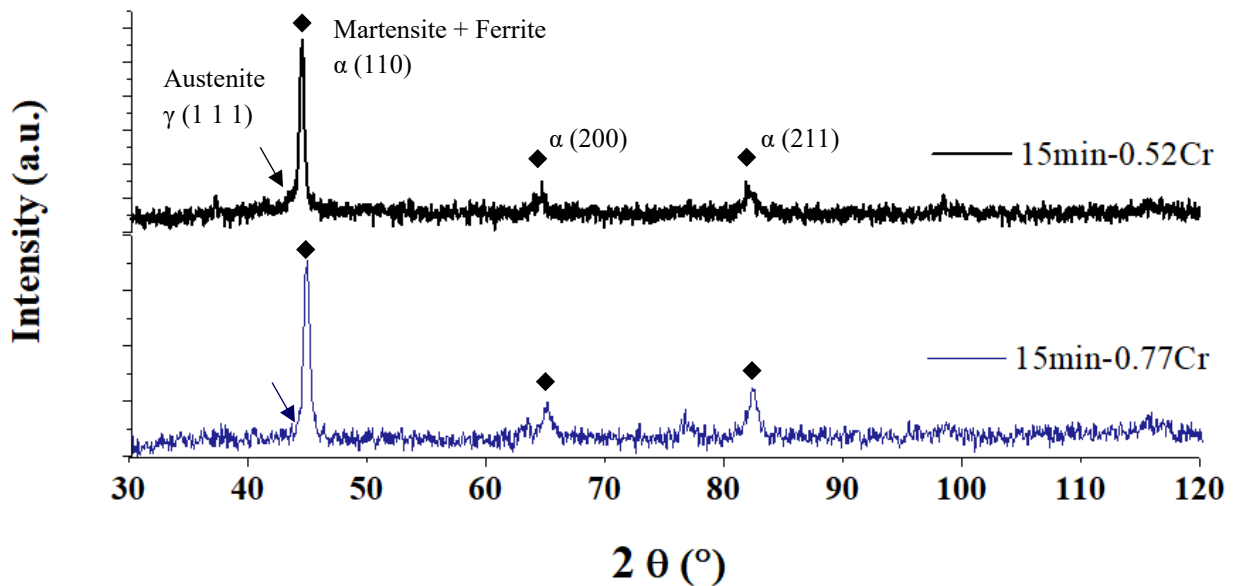
Figure 4.15. XRD patterns for as-quenched 0.52 wt% Cr and 0.77 wt% Cr plates from 950 °C for 15 min.

4.4.4 Microstructural characterization by EBSD

To compare the microstructures of quenched 0.52 wt% Cr and 0.77 wt% Cr plates, and to verify the obtained RA fraction (i.e., maximum 4.3 vol%) from previous XRD analysis, EBSD analysis was conducted on the steels after austenitization at 950 °C for 15 min.

EBSD data was obtained from a scanned area of $30 \times 25 \ \mu m^2$ with a scanning step size of 75 nm. The measured inverse pole figure, grain boundary distribution, and band contrast from RD-ND planes for the quenched 0.52 wt% Cr and 0.77 wt% Cr samples are shown in Figure 4.16 (a) and (b), respectively. The PAG and martensite packet boundaries are confirmed to be high angle grain boundaries (HAGBs) with misorientation angle (MA) larger than 15°, as highlighted in both figures. As expected, the martensite lath boundaries are observed to be low angle grain boundaries (LAGBs) with 2° < MA< 15°. The quenched 0.77 wt% Cr image (Figure 4.16 (b)) shows a lenticular structure with a length that exceeds the martensite packet size. This finding is consistent with the previous OM and SEM observations. Furthermore, the grain and lath orientations are randomly distributed, indicating that the texture of as-quenched martensite is weak.

Figure 4.17 (a) and (b) are phase maps for the two steels at the same location. Table 4.3 summarizes the fraction of LAGBs ($2° < \theta < 15°$) and HAGBs ($15° > \theta$), as well as the phase fractions. No cluster of RA phase was captured by EBSD, indicating that the steel was quenched to a temperature low enough to maximize martensite transformation. The grain boundary angles, grain sizes, orientation, and phase fractions for both the 0.52 wt% Cr and 0.77 wt% Cr plates are similar.

It is worth noting that the RA fraction (0.5 vol%) measured by XRD is similar to the value observed with EBSD (0.2 vol%). According to Pashangeh and Zarchi et al., the reason behind the slight discrepancy is that diffracted X-rays can detect the relatively fine grains of RA down to nearly 0.5-1 vol% in the carefully prepared steel samples, whereas EBSD only has a limited resolution due to the relatively large value of the EBSD step size (i.e., 75 nm) [43,96]. In addition, EBSD is a micro-scale analysis technique with a localized scanned area of 30×25 μm^2, so potential large RA colonies may be overlooked. Based on the measured RA fractions using the EBSD and XRD, the laboratory A&Q practices were able to produce a fully martensitic structure with minimal RA (0 - 1 vol.%).
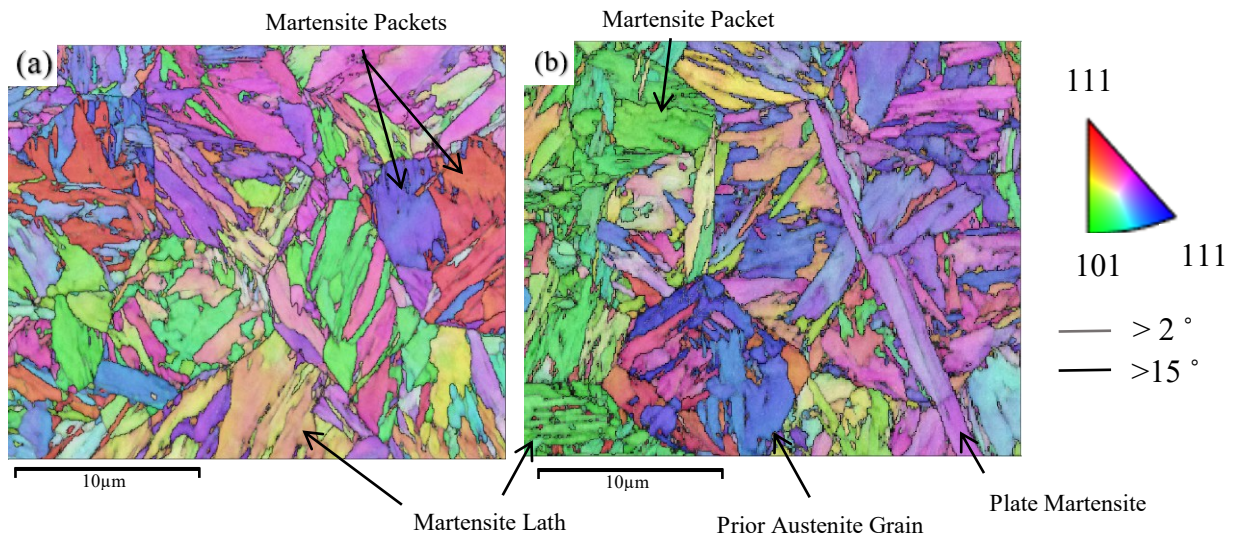
Figure 4.16. EBSD maps showing banded contrast, inverse pole figure, and grain boundaries. (a) 0.52 wt% Cr plate quenched from 950 °C-15 min and (b) 0.77 wt% Cr plate quenched from 950 °C-15 min. The images are overlaid with 2˚ low angle grain boundaries (LAGB) in light grey and high angle grain boundaries (HAGB) in black.
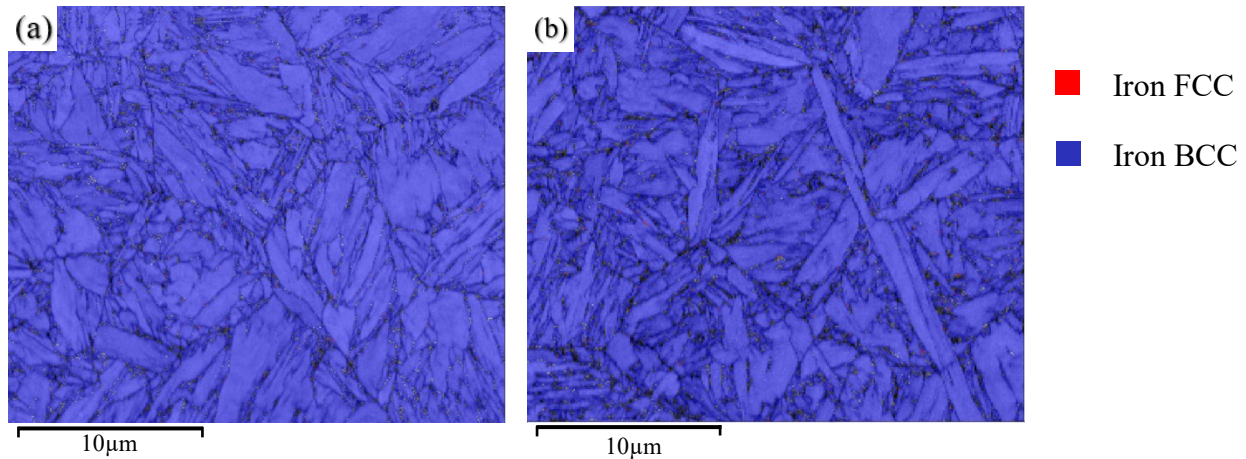
Figure 4.17. EBSD phase maps for (a) 0.52 wt% Cr plate quenched from 950 °C-15 min and (b) 0.77 wt% Cr plate quenched from 950 °C-15 min.

Table 4.3. Grain boundary angles and phase fractions from EBSD.

	Grain boundary angles		Phases fraction	
	LAGB	HAGB	BCT	Iron FCC
	$(2\,° < \theta < 15\,°)$	$(\theta < 15\,°)$	(Martensite)	(RA)
0.52 wt% Cr	33.1%	66.9%	>99.0%	<0.2 vol.%
0.77 wt% Cr	35.7%	64.3%	>99.0%	<0.2 vol.%

4.4.5 PAG growth

The average PAG size and austenitizing time are illustrated in Figure 4.18. The typical PAG morphology of the 0.52 wt% Cr plate after 950 °C for 15 min and 90 min are shown in Figure 4.19 (a) and (b), respectively. It is clear that the grain size increases with prolonged austenitization time. According to the plot in Figure 4.18 (c), the 0.52 wt% Cr plate exhibited a slightly higher grain growth rate compared to the 0.77 wt% Cr plate. The higher Cr content in the 0.77 wt% Cr plate causes a more pronounced dragging effect on austenite grain boundaries, which in turn leads to a slightly lower grain growth rate. Besides the alloying elements, additional C has been found to have an obstructing effect on austenite grain growth [33]. Thus, the higher nominal C content (0.28 wt%) in the 0.77 wt% Cr plate than the 0.52 wt% Cr plate (0.25 wt%) can also play a role in this phenomenon.
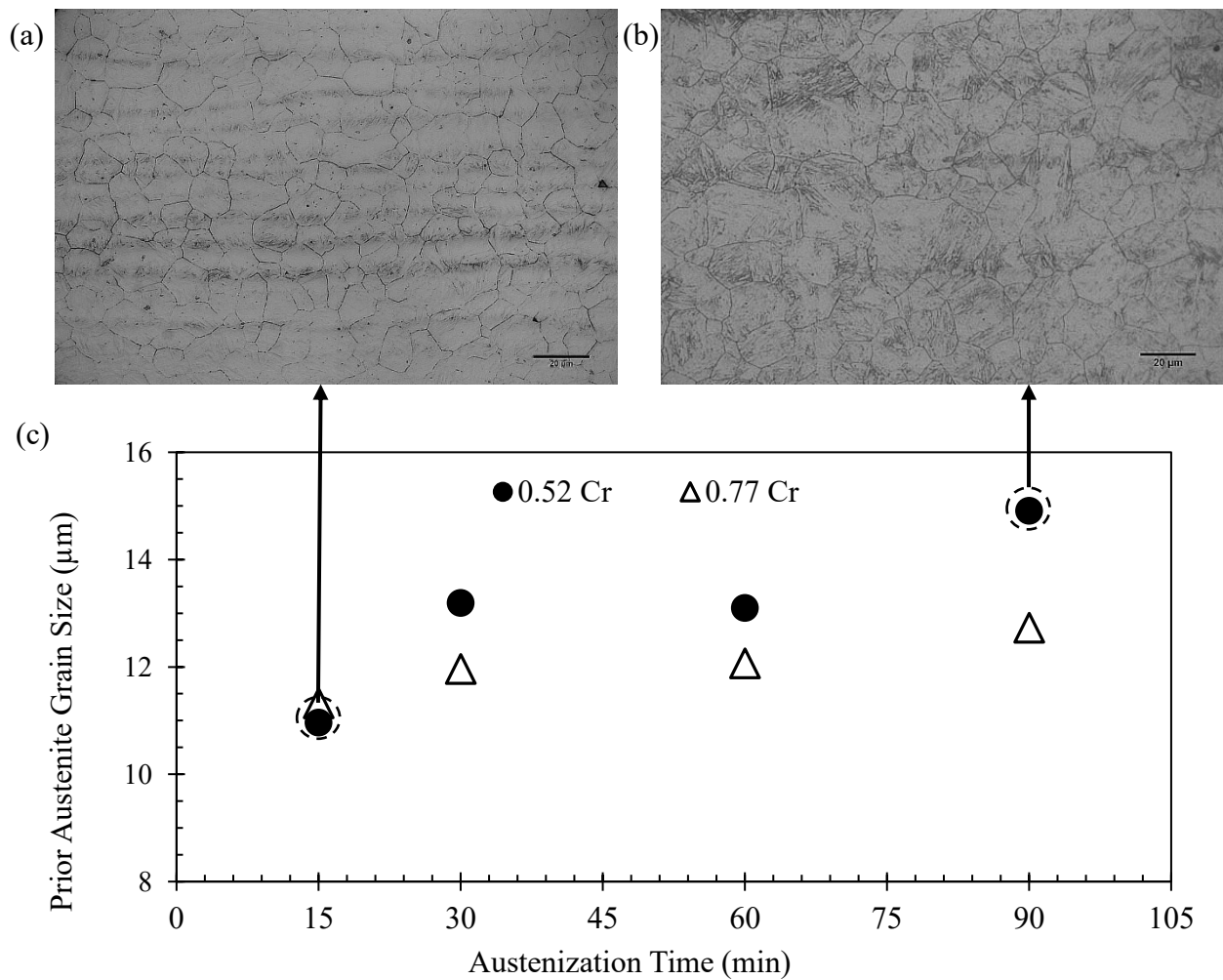
Figure 4.18. Optical images for (a) quenched 0.52 wt% Cr plate from 950 °C for 15 min and (b) quenched 0.52 wt% Cr plate from 950 °C for 90 min. (c) PAG size variation due to prolonged heating time for 15, 30, 60, 90 min at 950 °C.

4.4.6 Optimum A&Q condition

According to XRD and EBSD analysis, the laboratory quenching practice can produce fully martensitic steel with minimum RA (0.5 to 1 vol%). OM, SEM, and micro-hardness characterizations indicate that the changing austenitization time (15 to 90 min) does not have a pronounced effect on the as-quenched microstructure. Coalesced structures, which are believed to

be detrimental to toughness, were observed in all quenched steels. To mitigate their effect on toughness, minimizing PAG size is recommended. Additionally, steels with large PAG sizes generally exhibit lower toughness and cracking resistance (i.e., crack propagation is easier) because they have fewer grain boundaries for the strain to concentrate.

A&Q at 950°C for 30 min causes a slight reduction in the extent of Cr and Mo microsegregation (EMPA analysis), but the growth in PAG size during this period was significant. Therefore, as-quenched steel after heating to 950 °C for 15 min was selected as the starting materials for tempering studies based on the optimum balance between solutionizing and PAG growth.

4.4.7 *TEM characterization of precipitation*

The precipitations formed prior to tempering treatment could have a substantial influence on the tempered carbide morphology. Therefore, the precipitates that appeared in the optimum as-quenched steels (950 °C for 15 min) were characterized using S/TEM.

S/TEM analysis of carbon replica samples taken from the quenched 0.52 wt% Cr plate (950°C-15 min) is shown in Figure 4.19. The quenched plate contains very fine (<20 nm), dispersed particles (Figure 4.19 (a)). Bright-field (BF) TEM images at high magnification revealed that they are mostly spherical regardless of size (Figure 4.19 (b) and (c)). Due to the nature of carbon replica preparation, the locations and coherency with the steel matrix cannot be determined.
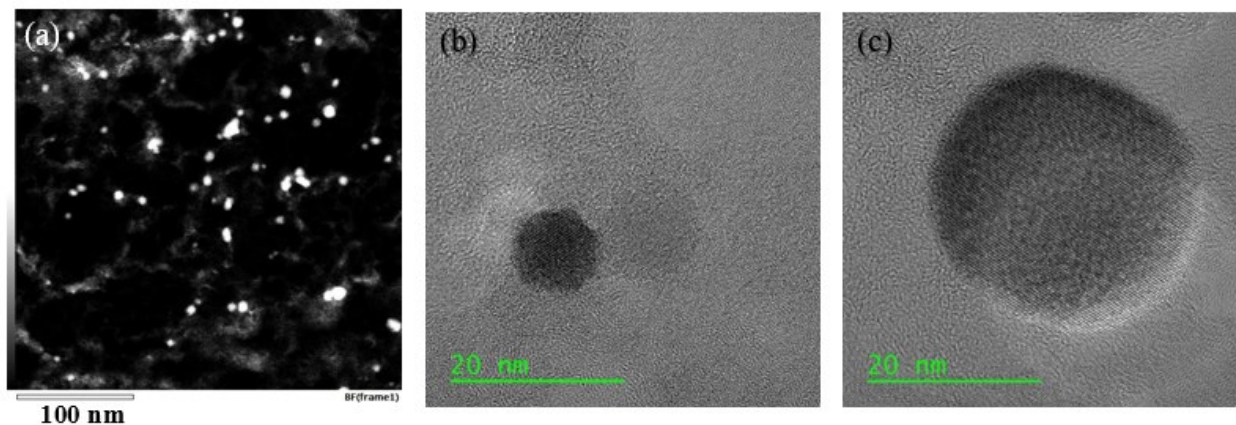
Figure 4.19. (a) STEM high angle annular dark-field (HAADF) image and (b, c) high resolution (HR) TEM micrographs of quenched 0.52 wt% Cr sample (950°C-15 min).

Figures 4.20 and 4.21 show STEM-high angle annular dark-field imaging (HAADF) images of precipitates extracted from quenched 0.52 wt% Cr and 0.77 wt% Cr plates (950 °C for 15 min) and their corresponding EDS maps of Mo, Ti, Cr, and Fe. All the obtained fine and spherical precipitates are rich in Mo and Ti. Some elliptical and cuboidal precipitates (>50 nm) with the typical shape for TiN are composed of Ti and Mo. EDS analysis determined that the Mo content in the metallic constituent of these spherical and elliptical particles ranges from 24 wt% to 64 wt% with an average of 34 wt%. Analyses for cuboidal particles are not presented due to the low number of analyzed particles. Furthermore, no iron-based carbides are observed in the as-quenched steels.

The precipitate size was measured based on the diameter of spherical particles, and the length of the longest axes of irregular particles (e.g., elliptical and cuboidal shape). Figure 4.22 shows precipitation size distributions for both carbon replicas. Nano-sized precipitates (< 10 nm) were the most common. At least 95% of precipitates have a size of less than 20 nm. The coarse precipitates with a size larger than 40 nm account for about 1% of the particles. A comparison in size distribution between 0.52 wt% Cr and 0.77 wt% Cr plates displayed no distinctive difference. This was expected since the nominal Mo and Ti content in the as-rolled 0.52 wt% Cr and 0.77 wt% Cr plates are similar. The variation in nominal C content from 0.25 wt% to 0.28 wt% did not affect the size distribution of the precipitates either.
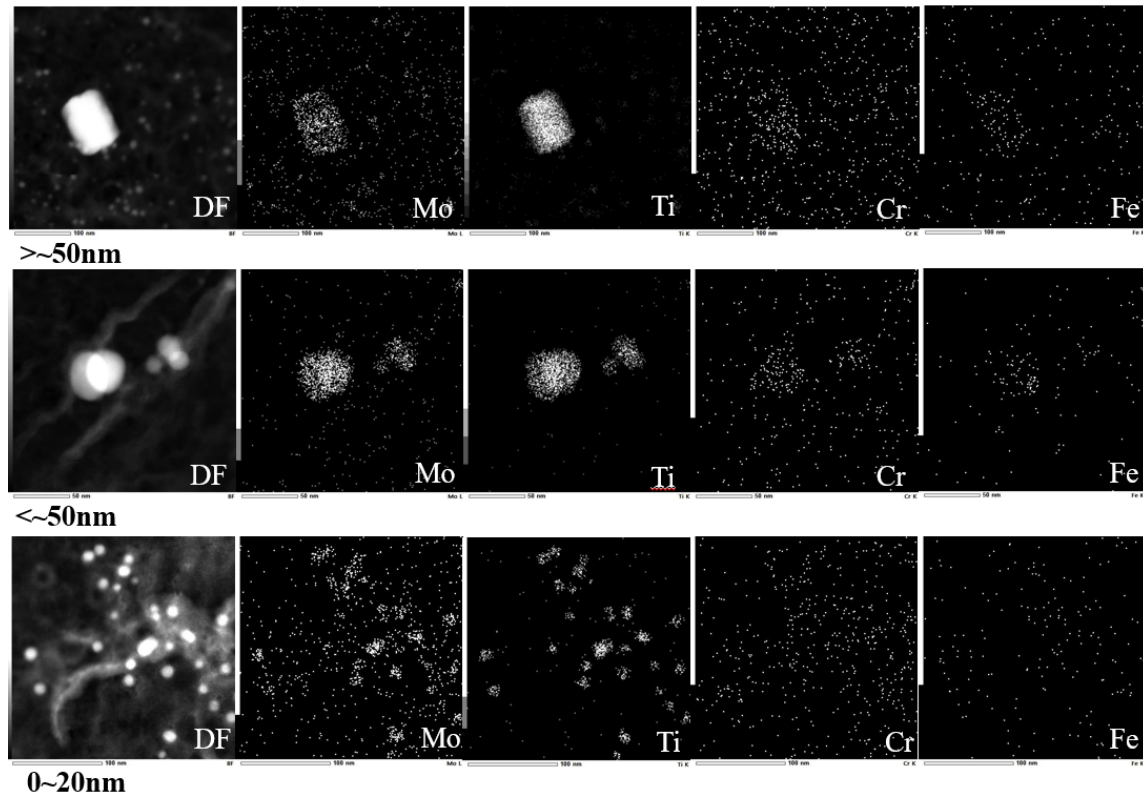
Figure 4.20. STEM HAADF images of as-quenched 0.52 wt% Cr samples (950 °C-15 min) and corresponding EDS maps of Mo, Ti, Cr, and Fe.

These fine, spherical, and (Ti, Mo) enriched precipitates could have been the MC-type precipitate. It is anticipated that these finely dispersed precipitates are beneficial in the sour service application, as they can not only irreversibly traps more hydrogen atoms but also contribute to dispersion strengthening [5]. The precipitates with large size (i.e. > 70 nm) normally have lower trapping ability due to their incoherent interface with ferrite matrix [79]. In the next chapter, their origins, crystal structure, and evolution (i.e., size and composition) during tempering treatment will be detailed and discussed.
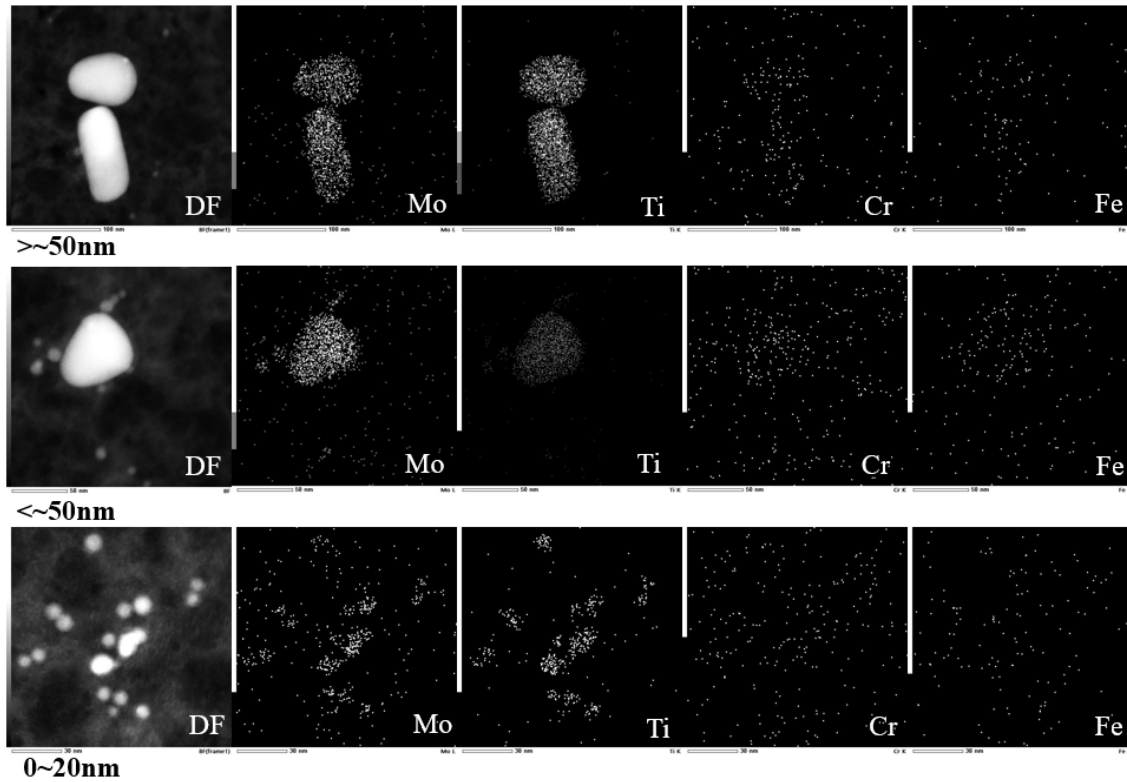
Figure 4.21. STEM HAADF images of as-quenched 0.77 wt% Cr samples (950°C-15 min) and corresponding EDS maps of Mo, Ti, Cr, and Fe.
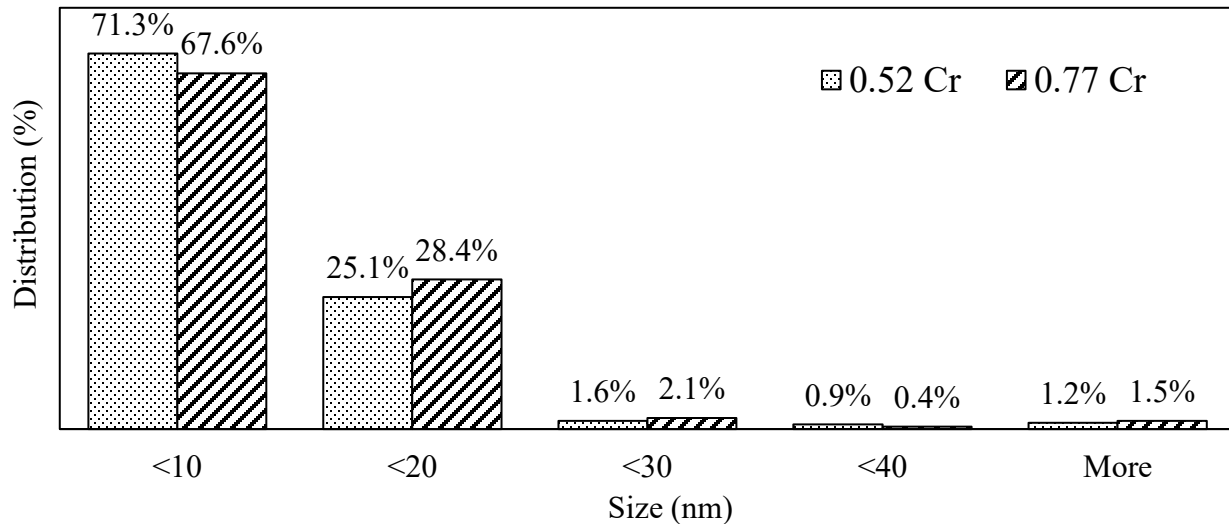
Figure 4.22. Precipitation size distribution maps based on 450 particle counts for each sample quenched from 950°C for 15 min.

Chapter 5

Characterization of Quenched and Tempered Samples

Based on the characterizations and analyses in Chapter 4, the A&Q treated 0.52 wt% Cr and 0.77 wt% Cr steels from 950 °C for 15 min were selected as the starting materials for tempering studies. The tempering behaviour of the A&Q steels was investigated using micro-hardness, tensile testing, and the Holloman Jaffe (HJ) tempering parameter. FESEM and STEM were conducted to study the effects of tempering conditions on the microstructure with emphasis on the characterization of carbide morphologies. The relations among carbide morphology, steel composition, and tempering conditions were studied using Thermo-Calc simulations. Finally, the effects of tempered microstructure on tensile properties and hardness are discussed.

5.1 Hardness and Holloman Jaffe Tempering Parameter

A schematic of the laboratory heat treatment schedules is presented in Figure 5.1. Specimens quenched from 950 °C (held 15 min) were tempered at temperatures between 550 and 715 °C for times between 15 and 390 min. Micro-hardness testing was performed on all heat-treated samples to determine their tempering behaviors.
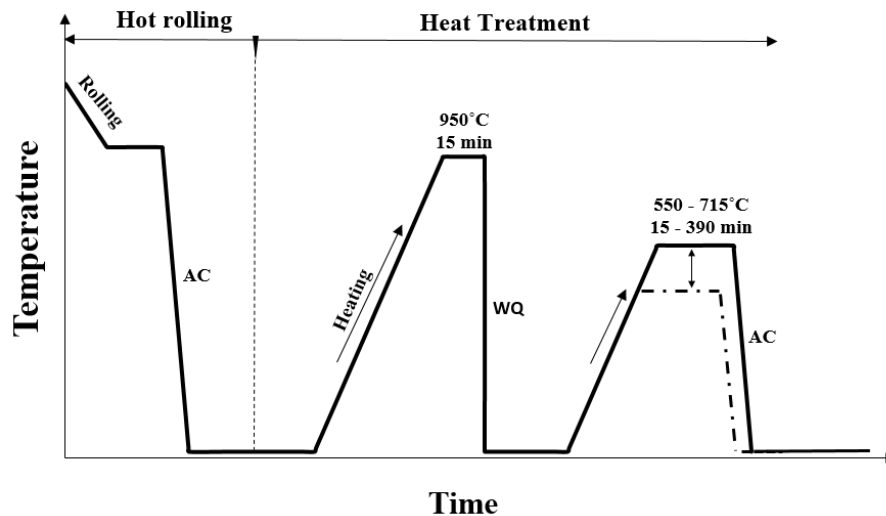
Figure 5.1. Schematic of hot rolling and subsequent A&Q&T heat treatment routes.

Using the Holloman Jaffe (HJ) (Equation 2.7) introduced in Chapter 2.4, the value of HJ was calculated for each heat treatment. A value of $C= 19.5$ was selected based on the carbon content of the steel [53]. The value of t used in the calculation is the isothermal holding time for tempering, where the non-isothermal periods (i.e., heating and cooling processes) were not included.

Table 5.1 summarizes the tempering temperature and time, the corresponding HJ parameters, and the measured hardness values in this study. HJ parameter, as expected, increases with increasing temperature and time with the former having the largest effect. In order to meet the industrial heating treating schedule, most laboratory tempering treatments are conducted between 600 °C and 715 °C for a total time (heating + soaking) of 45 min.

Table 5.1. HJ and average micro-hardness values.

Temperature (°C)	Time (min)	HJ Parameter	Hv (0.77 wt% Cr)	Hv (0.52 wt% Cr)
550	45	15.9	335 ± 4	329 ± 3
575	45	16.4	326 ± 4	318 ± 4
600	45	16.9	319 ± 5	310 ± 5
600	300	17.6	303 ± 3	300 ± 4
625	45	17.4	311± 4	307 ± 3
650	45	17.9	297 ± 5	294 ± 2
650	390	18.7	257 ± 4	253 ± 3
670	15	17.8	294 ± 6	289 ± 4
670	45	18.3	276 ± 3	272 ± 2
675	45	18.4	269 ± 4	268 ± 2
680	45	18.5	267 ± 3	266 ± 3
685	45	18.6	265 ± 3	260 ± 4
690	45	18.7	256 ± 2	255 ± 3
700	45	18.9	256 ± 3	254 ± 2
715	15	18.7	259 ± 6	258 ± 5
715	45	19.1	245 ± 3	242 ± 3
715	180	19.7	225 ± 3	220 ± 5

Figure 5.2 shows the measured hardness plotted as a function of the calculated HJ parameter. The hardness experiences a continuous decrease with an increase in HJ values. At low HJ values, the hardness decreases at a slower rate compared to the change in hardness for HJ values greater than

(>) 17.4. Best-fit linear regression lines as shown in the graph illustrate this change in rate. The two linear relationships developed are:

$$\text{Hardness (Hv)} = -15.54\text{HJ} + 578.5 \qquad (\text{HJ} < 17.4) \qquad \text{(Equation 5.1)}$$
$$R^2 = 0.850$$
$$\text{Hardness (Hv)} = -42.02\text{HJ} + 1043.8 \qquad (\text{HJ} \geq 17.4) \qquad \text{(Equation 5.2)}$$
$$R^2 = 0.981$$

To validate the trends observed, complementary tempering tests were conducted. These complementary tests are shown as filled squares in Figure 5.2. The 0.52 wt% Cr and 0.77 wt% Cr specimens were tempered at two distinctive conditions (i.e., 650 °C – 390 min, and 715 °C – 15 min) with the same HJ values (18.7). The specimens tempered for the two conditions exhibited only a 0.5 % difference in measured hardness values. In addition, the linear HJ relationship can accurately predict measured hardness within less than 0.3 % deviation.
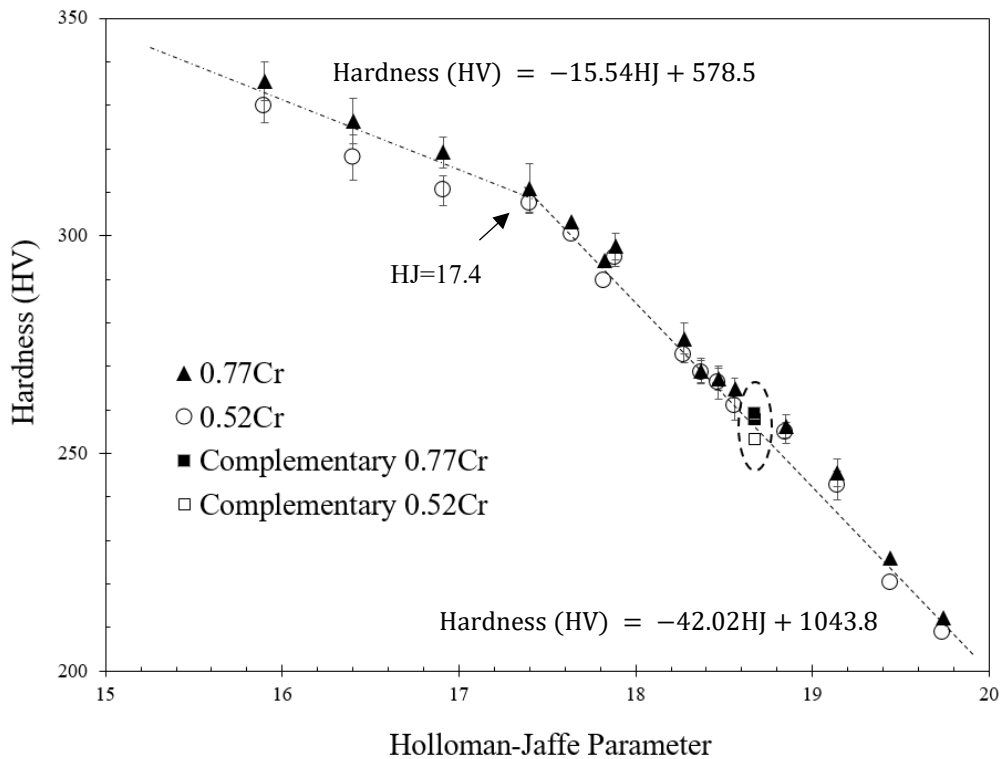
Figure 5.2. Micro-hardness versus HJ tempering parameters.

66

Published work indicates that the general decreasing hardness trend (Figure 5.2) is related to dislocation rearrangement/annihilation, substructure recovery, and a decrease in the quantity of interstitial carbon atoms in the matrix with the progression of tempering [5]. The change in hardness decreasing rate at HJ=17.4 (an empirical value for the P110 alloy system) indicates the occurrence of retardation of softening during tempering [53]. The presence of carbide-forming elements, Cr and Mo, is thought to be the main reason for this. According to Bain and Paxton, even a 0.5 wt% Cr or 0.5 wt% Mo addition can serve to resist softening [51]. No particular increase in martensite hardness (i.e., secondary hardening peak) was observed, indicating that the tempered particles were not fine enough to cause secondary hardening.

It should be noted that the tempered 0.77 wt% Cr plate consistently exhibited slightly higher hardness values relative to its 0.52 wt% Cr counterpart. A published study suggests that the amount of retardation of softening is proportional to the volume fraction (f_v) of alloy carbides and thus, is directly related to the amount of carbide forming elements [50]. Thus, the increase in Cr content from 0.52 wt% Cr to 0.77 wt% Cr may result in a difference in carbide morphology (e.g., volume fraction and average size).

In order to reveal the metallurgical effect of increasing Cr content, as well as to understand the mechanism behind the retardation of softening, FESEM and TEM characterization of the tempered structure and carbide morphology are presented and discussed in the following two sections.

5.2 SEM Characterization of Tempered Structure

Figure 5.3 (a), (b), (c), and (d) show SEM micrographs of 0.77Cr samples tempered at 600 ˚C, 650 ˚C, 685 ˚C, and 715 ˚C (45 min), respectively. Figure 5.3 (e), (f), (g), and (h) are higher magnification images of (a), (b), (c), and (d), respectively. The tempered structure consists of lath ferrite and precipitates.

In the fourth stage of tempering (600 °C to 700 °C), the growth and composition change of cementite accelerate [47]. With increasing tempering temperature, carbide coarsening reduces the pinning action of lath boundaries and the lath structure will begin to coarsen [47,69]. The lath width (Figure 5.3 (e), (f), (g), and (h)) increased with increasing temperature, probably due to the merging of two neighboring laths or the interface migration [97]. The average lath width (W_l) of samples

tempered at 600 °C, 650 °C, and 715 °C (45 min) was estimated using a line intercept method (based on 20 laths for each condition). The W_1 at temperatures of 600 °C, 650 °C, and 715 °C (45 min) corresponds to 329 ± 69 nm, 335 ± 89 nm, and 638.7 ± 90 nm, respectively, with the most substantial change in coarsening occurring between 650 °C and 715 °C. A similar magnitude of lath coarsening with increasing temperature was observed in a study by Sun and Wang et al [97], in which a 0.28Cr-0.40Mo-1.00Cr steel was tempered at three different temperatures (i.e., 650 °C, 700 °C, and 720 °C) for 60 min.

As noted above, coarsening of the lath ferrite should be accompanied by both the coarsening and compositional change of the carbides. The change in carbide morphology with tempering temperature and time is discussed in Chapter 5.5.
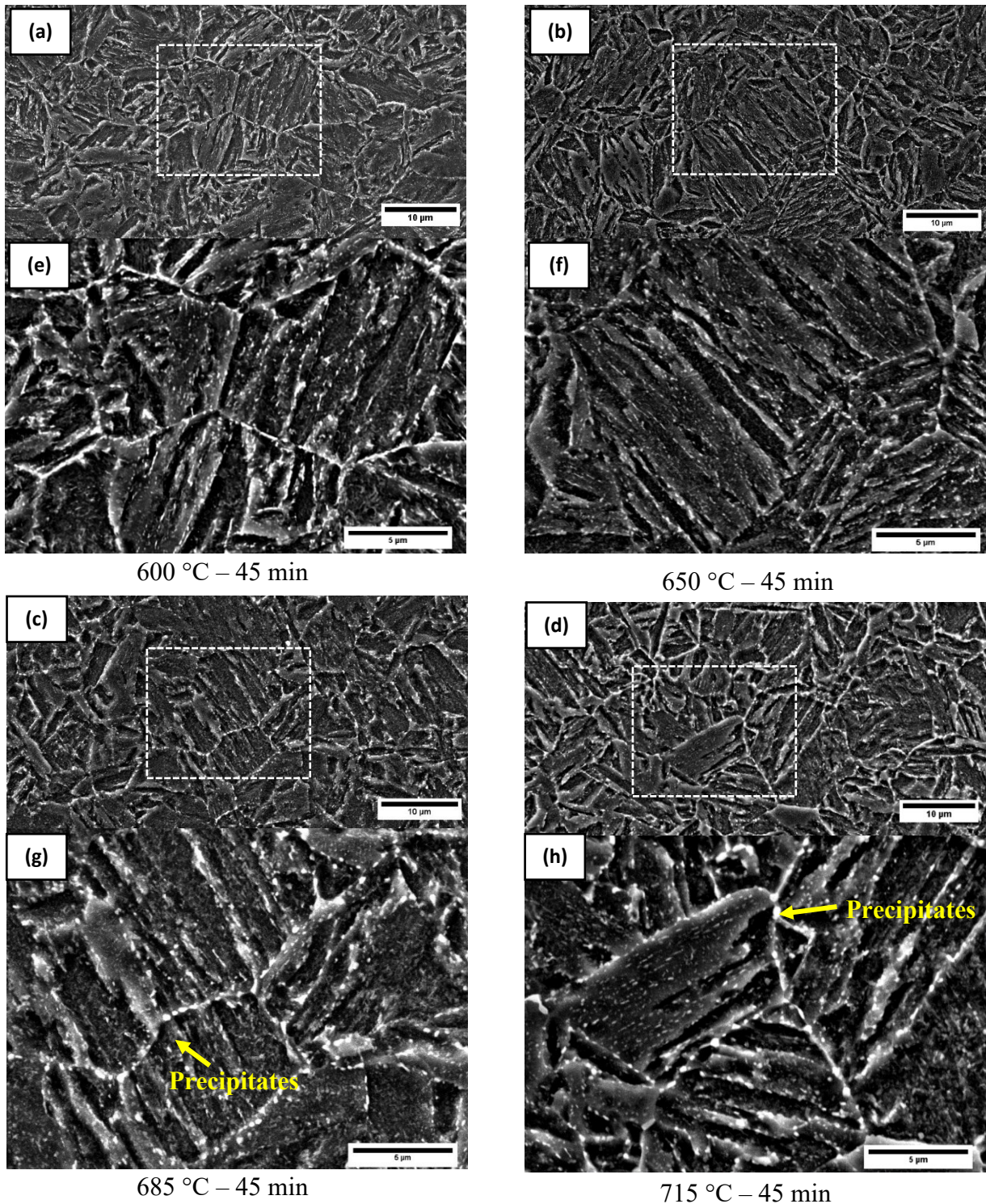
Figure 5.3. (a), (b), (c), and (d) SEM SE micrographs of 0.77 wt% Cr samples tempered at 600 ˚C, 650 ˚C, 685 ˚C, and 715 ˚C (45 min), respectively. Micrographs (e), (f), (g), and (h) correspond to higher magnification images of (a), (b), (c), and (d).

5.3 Assessment of Thermodynamic Stability of Carbides

Thermodynamic calculations on carbide stability were performed using Thermo-Calc software version 10.0 (TCFE10 database). The calculated mole fractions of carbides as a function of temperature using the nominal compositions of 0.77 wt% Cr and 0.52 wt% Cr steels were similar. Therefore, only the result based on the nominal chemical compositions of 0.77 wt% Cr steels will be presented in this section.

The amount of phases as a function of temperature for the 0.77 wt% Cr is illustrated in Figure 5.4. In addition to ferrite (BCC) and austenite (FCC), four types of carbides are thermodynamically stable over the tempering temperature range (550 °C to 715 °C): MC, M_3C, M_7C_3, and $M_{23}C_6$. Ti and Mo are the M constituent of MC carbide. Fe, Cr, Mo, and Mn are the M constituent of M_3C, M_7C_3, and $M_{23}C_6$ carbides. As the temperature increases beyond 600 °C, M_7C_3 completely dissolves and the phase fraction of $M_{23}C_6$ gradually decreases, whereas the fraction of the M_3C continues to increase up to 730 °C. A small fraction of MC-type precipitate remains up to 1200 °C. It is worth noticing that no Mo-carbide, such as M_2C or MC, is predicted in both the 0.52 wt% Cr and 0.77 wt% Cr alloy systems. The individual carbide types are studied via direct (S)TEM measurement of crystal structure, size, and composition and through additional Thermo-Calc analysis.
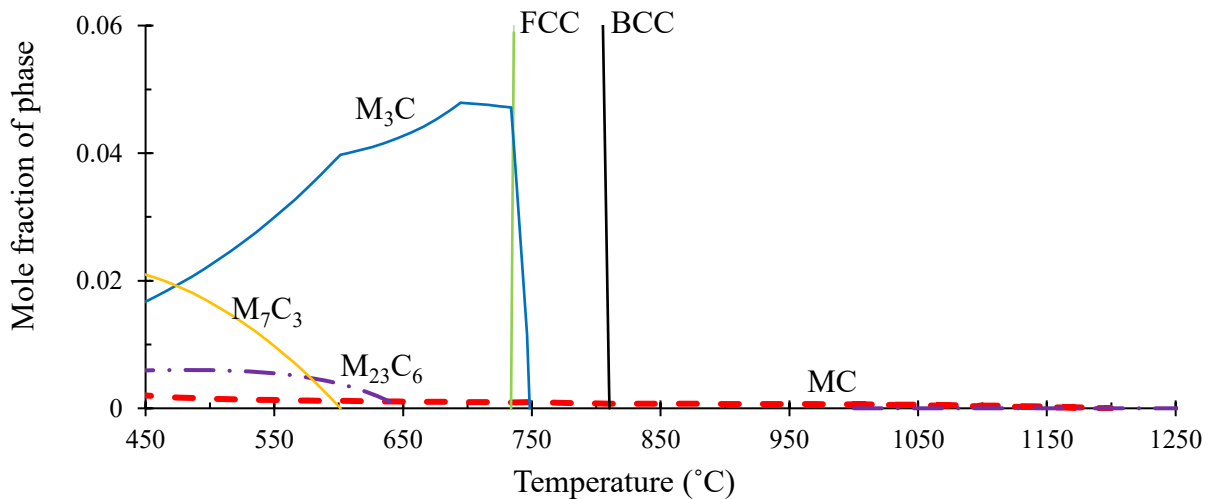
Figure 5.4. Mole fraction of phases as a function of temperature calculated using Thermo-Calc.

5.4   Analyses of MC Carbide

In this section, the precipitation of MC in the tempered steels was characterized by FESEM, (S)TEM, and studied by Thermo-Calc simulations.

5.4.1 FESEM and STEM characterization of MC type carbides

Figure 5.5 presents an FESEM micrograph of the precipitates in tempered 0.77 wt% Cr plate (715 °C-45 min). Coarse particles are readily visible. According to the EDS line scan in Figure 5.5 (b), the major component in all the coarse carbides is Fe. The counts of Fe X-rays across the coarse carbides are lower than the relative values in ferrite matrix due to the presence of Cr element. Very fine particles are also present and they are uniformly distributed in both the ferrite matrix and along the grain boundaries. Due to their relatively small size, EDS analysis was not undertaken. Therefore, STEM characterization of the chemical composition and crystal structure of these fine MC carbides was done.
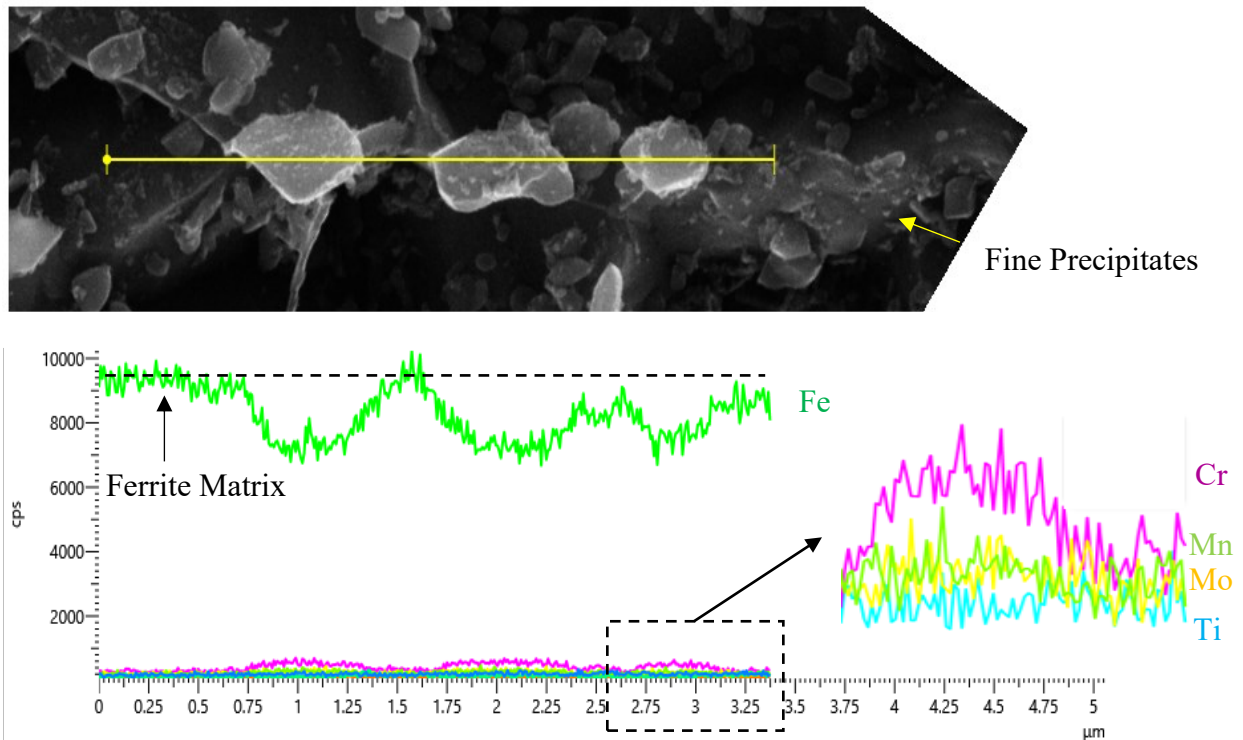
Figure 5.5. (a) FESEM SE micrograph of Fe-based precipitates along a ferrite grain boundary. (b) EDS line scan of the precipitates in (a).

Figure 5.6 shows a STEM-high angle annular dark-field (HAADF) image of tempered 0.77 wt% Cr plate (715 °C - 45 min) and the corresponding elemental maps. Two major types of carbides are present: coarse and rod-shaped particles (>50 nm), fine and spherical particles (<20 nm), see Figure 5.6 (b). The coarse particles were found to be enriched with Fe, Cr, and Mo (Figure 5.6 (c), (d), and (e)), and they are the primary precipitates in the tempered steels. The fine particles contain Mo and Ti (Figure 5.6 (e) and (f)), which may be the previously observed precipitates in as-quenched P110 steels. By measuring the size of the Ti-Mo particles from the EDS elemental mappings (50 particles), over 90% of Ti/Mo rich particles have a size of less than 20 nm. This fraction is similar to the particle size distribution obtained from as-quenched steels.
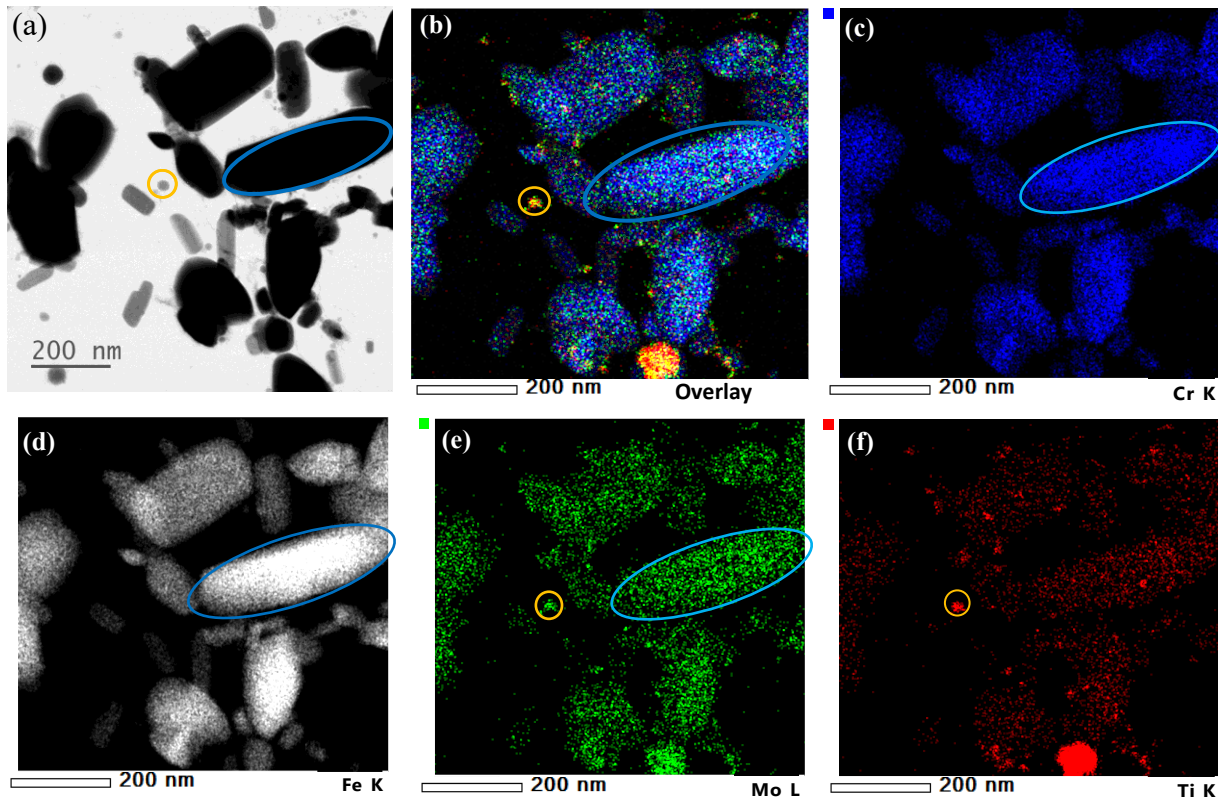
Figure 5.6. (a) STEM HAADF image of tempered 0.77 wt% Cr plate (715 °C for 45 min) and the corresponding EDS maps of (b) overlay maps of Cr, Fe, Ti, and Mo elements, (c) Cr, (d) Fe, (e) Mo, and (f) Ti.

High resolution (HR) - STEM imaging was conducted to determine the crystal structure of the Mo and Ti enriched particles. Bright field (BF) and HAADF images of these particles are shown in

Figure 5.7 (a) and (b), respectively; the corresponding Fast Fourier transform (FFT) pattern is shown in Figure 5.7 (c). The FFT pattern can be indexed to $(Ti_{0.5}Mo_{0.5})C$, which has a NaCl type crystal structure (same as TiC).
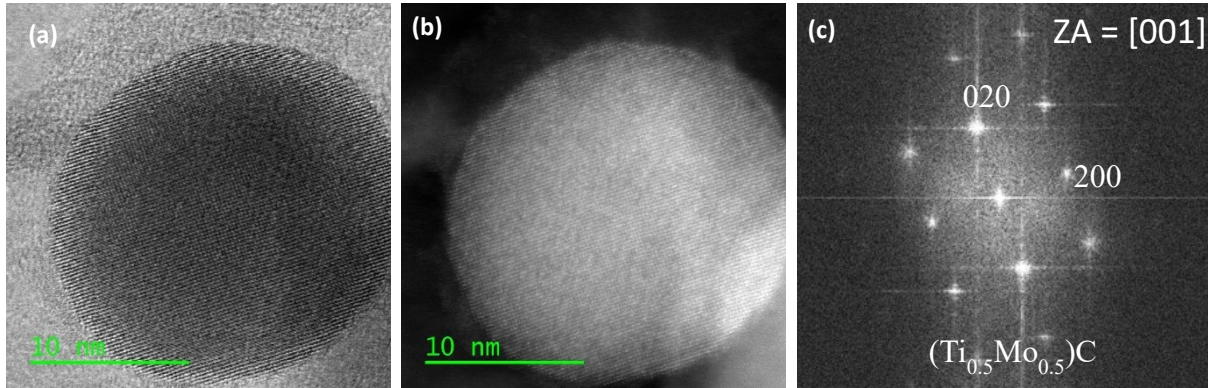
Figure 5.7. (a) BF image, (b) DF HR-STEM image, and (c) corresponding FFT image of MC type carbide.

The Ti and Mo content in (Ti,Mo)C carbides were measured via STEM-EDS analysis in tempered 0.77 and 0.52 wt% Cr plates (715 °C for 45 min). Figure 5.8 shows one such spectrum. The Fe and Cr peaks came from the extracted ferrite matrix. Based on the measured 40 particles, the average metallic composition was 44 wt% Mo (28 at%) and 56 wt% Ti (72 at%). The weight percentage of Mo (i.e., 44 wt%) is higher than the 34 wt% obtained from the as-quenched specimens.
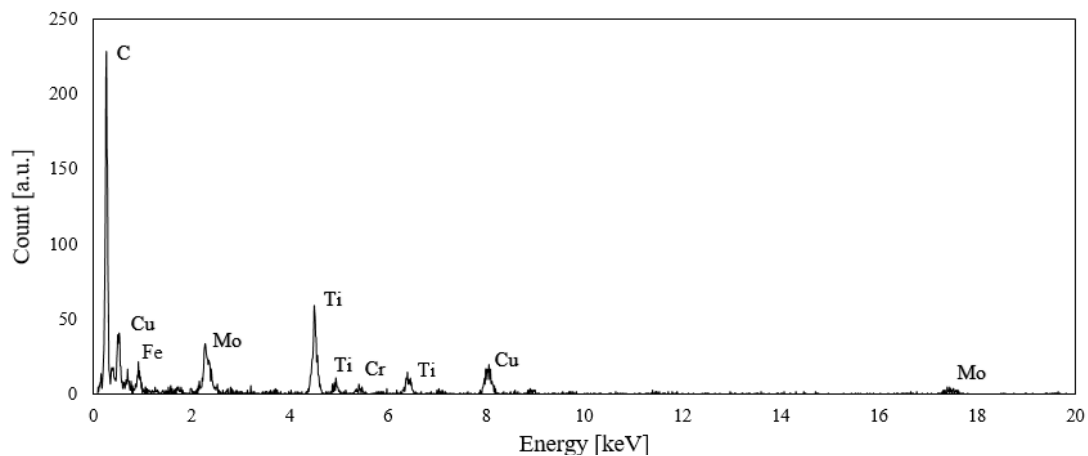
Figure 5.8. STEM-EDS spectrum from a (Ti,Mo)C particle. The Cu peaks in the EDX spectrum are from the copper grid (sample holder), and the C peak comes from the carbide as well as the carbon film of the carbon replica specimen.

5.4.2 Thermodynamic simulations for MC carbide precipitation

To understand the mechanism of (Ti,Mo)C precipitation, and to investigate the effect of tempering treatment on (Ti,Mo)C carbides, thermodynamic calculations were performed using Thermo-Calc software.

Figure 5.9 shows the calculated precipitation curves for MC type carbides. A simplified system with a composition of 0.28C-(0.03 to 0.04)Ti-(0 to 0.3)Mo-Fe (wt%) was considered for the calculation. It is clear that with a slight increase in nominal Ti content (from 0.03 to 0.04 wt%), the precipitation amount increases significantly. This suggests that in the experimental steel, it is Ti that determines the quantity of precipitation. Furthermore, with an increase in Ti addition, the solid solution temperature in austenite correspondingly increases. Figure 5.9 also illustrates the effect of Mo addition on TiC precipitation behavior. After addition of Mo, the total amount of TiC increased. Under the circumstance where the crystal structure of MC remains unchanged, an increase in precipitation amount indicates that the Mo element enters the TiC structure, which indirectly increases the mass fraction of TiC precipitation. This speculation is proven valid as the MC carbides have the same crystal structure as TiC (Figure 5.7). It is noteworthy that due to the predicted precipitation of MoC carbides in the simplified C-Ti-Mo-Fe system, the Mo content in MC carbides starts to decrease at temperatures lower than approximately 670 to 720 °C.
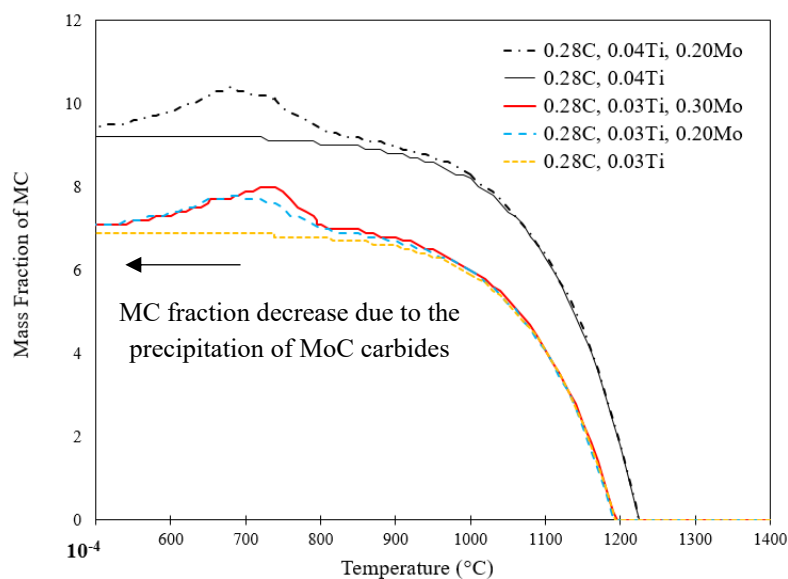
Figure 5.9. Calculated precipitation curves for MC with different Ti and Mo content.

74

Figure 5.10 presents the calculated Mo and Ti content in the (Ti, Mo)C phase as a function of temperature. A simplified system with a composition of 0.28C-0.03Ti-0.20Mo-Fe (wt%) was considered for the calculation. As shown in Figure 5.10, MC carbides became more enriched in Mo at temperatures lower than approximately 815 °C, indicating that Mo has low solubility in the ferrite/BCC matrix and a high driving force to enter the (Ti, Mo)C precipitates in the laboratory tempering temperature region (i.e., low temperature ferrite region). The trend of increased Mo content in MC carbides is consistent with previous STEM-EDS measurements where the average Mo content in MC increased from 34 wt% (as-quenched steel) to 44 wt% (tempered steel from 715 °C for 45 min). Furthermore, at 690 °C, there is a trough of the Ti content in the MC phases and a corresponding peak of Mo content. This provides evidence that Mo enters TiC through substitution, thereby forming (Ti, Mo)C.
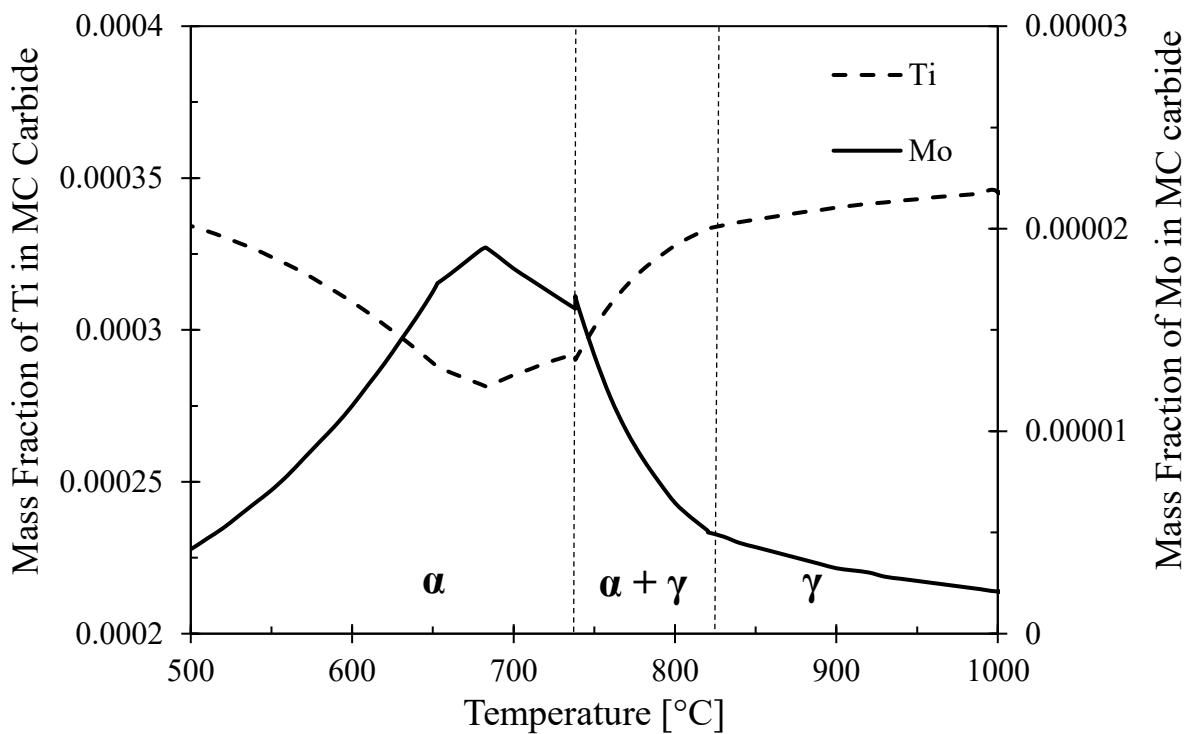
Figure 5.10. Calculated Mo and Ti compositions for MC as a function of temperature in the 0.77 wt% Cr steel.

5.4.3 Effect of tempering treatment on MC carbide coarsening

Previous MC carbide size measurements from EDS maps for tempered 0.77 wt% Cr steel (715 °C - 45 min) showed that over 90% of MC carbides have a size of less than 20 nm (similar to the size distribution of the as-quenched specimen). This indicates that coarsening of MC during tempering was negligible.

Numerous studies have proposed that the incorporation of Mo favors nucleation of MC and simultaneously suppresses coarsening by reducing the interfacial energy of the MC/ferrite interface [98,99,100,101,102]. Thus, the measured high average Mo content (44 wt%) in MC for tempered specimens indicates that Mo may inhibit carbide coarsening to some extent.

Finally, coarsening of (Ti, Mo)C is controlled by the diffusion of Ti in ferrite [98,99,100,101]. The limited Ti content in ferrite and its low diffusivity does not satisfy the conditions for MC carbide coarsening.

5.4.4 Summary and potential effects of MC carbide

The fine MC precipitates were presumably formed during industrial hot rolling via strain-induced precipitation in which the diffusion rates for both Ti and Mo atoms were high. Only about 1.2 % of the particles in the as-quenched steels were larger than 40 nm (the size distributions were present in Chapter 4.4.7. This indicates that the industrial hot rolling temperature was not high enough to induce detrimental MC carbide coarsening. After the tempering treatment, (Ti,Mo)C carbides retained a similar size distribution of the as-quenched steels but had a higher average Mo content (increased from 34 to 44 wt%).

It is accepted that the introduction of the fine carbides is conducive to achieving precipitation strengthening and increasing HE resistance by providing a high density of irreversible hydrogen traps [5,2,80]. In particular, precipitates with sizes less than 30 nm, such as TiC, MoC, and Mo_2C, exhibit strong hydrogen trapping ability [2,103,104]. Furthermore, the (Ti,Mo)C particles with fine morphology could contribute to the grain boundary pinning action and possibly participate in the retardation of martensite recovery [69].

5.5 Analysis of Iron-based Carbides

TEM analysis was performed on 0.52 wt% Cr and 0.77 wt% Cr samples tempered at six different tempering conditions along the HJ plot. The selected conditions are highlighted in Figure 5.11. In this section, the effects of steel composition (i.e., C and Cr content), tempering temperature (from 600 to 715 °C), and time (from 15 to 360 min) on the morphology of Fe-based carbides are studied.
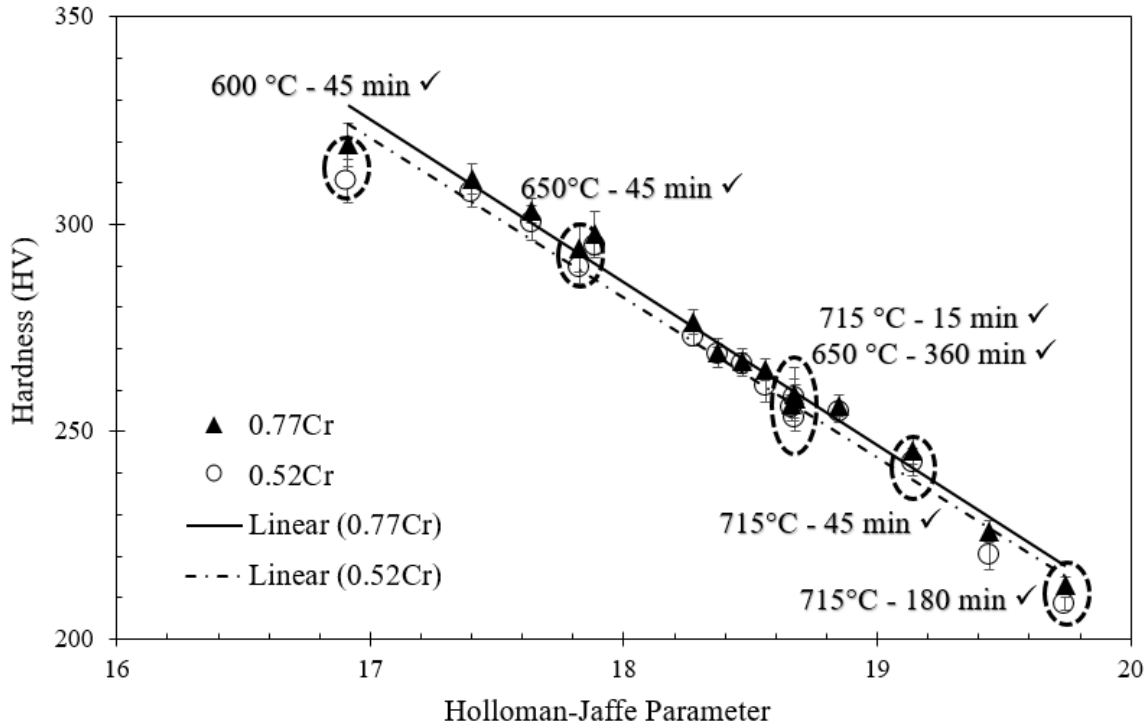
Figure 5.11. Selected conditions for TEM analysis (highlighted in the circle).

5.5.1 STEM identification of Fe-carbides

Figure 5.12 (a), (b), (c), and (d) shows TEM BF micrographs taken from carbon extraction replicas after tempering at 715 °C for 45 min. Their corresponding selected electron diffraction (SAED) patterns are shown in Figure 5.12 (e), (f), (g), and (h), respectively. All particles were identified to be M_3C with an orthorhombic crystal structure. Similar M_3C particles were identified in all the tempered samples.

77
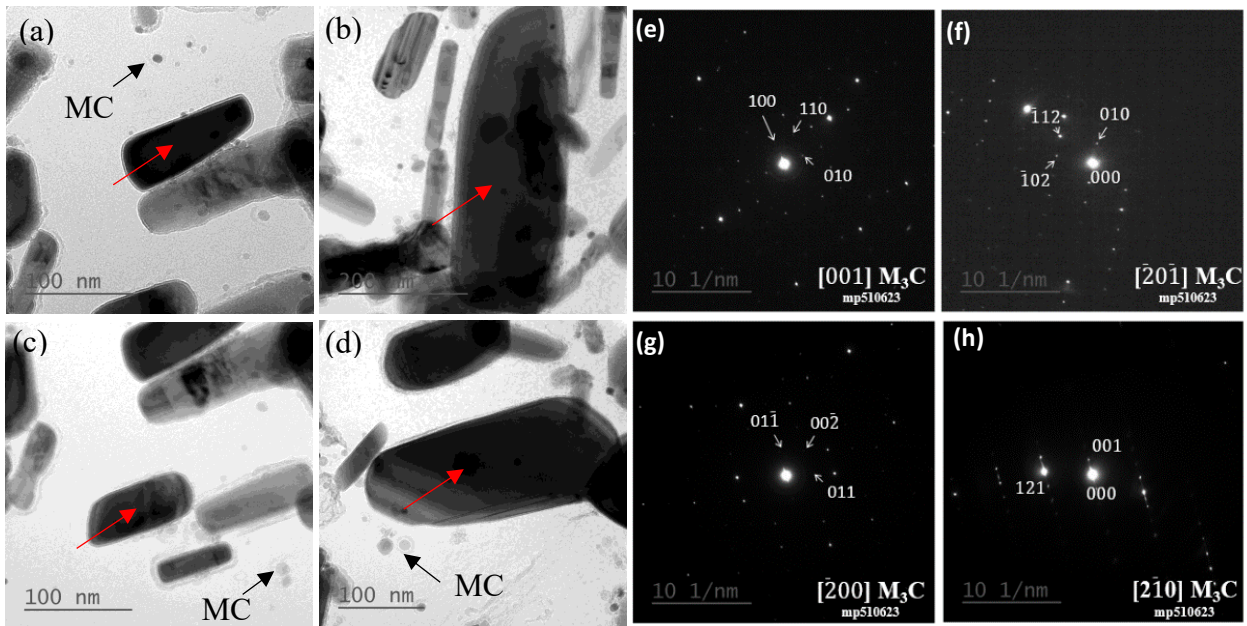
Figure 5.12. (a), (b), (c), and (d) TEM BF images of carbon replica samples after tempering at 715 °C for 45 min. (e), (f), (g), and (h) SAED patterns for the carbides in (a), (b), (c), and (d), respectively. The patterns are indexed to M_3C and are close to the zone axes shown.

Figure 5.13 (a) and (c) show STEM-BF micrographs of the oval and rod shaped precipitates, respectively. Their corresponding FFT patterns revealed that the precipitates are $M_{23}C_6$ carbides with a cubic crystal and a lattice parameter of 10.7 Å, as shown in Figure (b) and (d). It is noteworthy that $M_{23}C_6$ carbides were only identified in the 0.77 wt% Cr samples tempered at 650 °C (45 min).
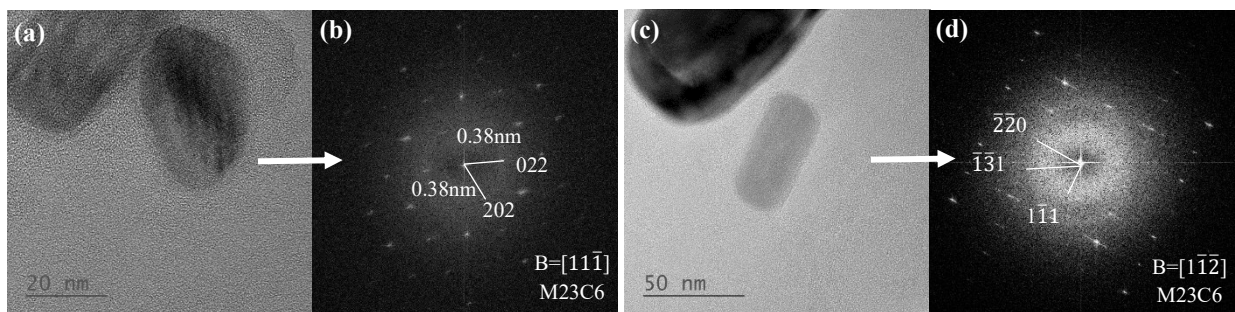
Figure 5.13. STEM DF images of $M_{23}C_6$ carbides with (a) oval shape and (c) rod shape from carbon replica samples tempered at 650 °C for 45 min. (b) and (d) FFT patterns from (a) and (c), respectively. There are indexed to $M_{23}C_6$ and close to the zone axes shown.

78

All the carbides identified in the samples tempered at six different conditions are summarized in Table 5.2. M_3C and MC carbides were identified in all the tempered steels, whereas $M_{23}C_6$ carbides were only identified in the 0.77 wt% Cr sample tempered at 650 °C for 45 min. No (S)TEM carbide identification was performed on tempered 0.52 wt% Cr and 0.77 wt% Cr samples at 650 °C for 390 min. Additionally, no $M_{23}C_6$ carbides were observed in tempered steels at 600 °C, which is inconsistent with thermodynamic equilibrium calculations (Figure 5.4). This inconsistency is mainly the result of neglecting kinetic effects during thermodynamic calculations. The effect of kinetics is particularly noteworthy at 600 °C, where the major metallic component of $M_{23}C_6$ (i.e., Mo) has a small diffusivity ($D_{Mo} = 4.2 \times 10^{-19} m^2/s$) in the ferrite matrix [17].

Table 5.2. Carbide types formed in tempered 0.52 wt% Cr and 0.77 wt% Cr steels determined by (S)TEM.

Conditions	HJ Parameter	0.52 wt% Cr	0.77 wt% Cr
600 °C – 45 min	16.9	M_3C + MC	M_3C + MC
650 °C – 45 min	17.9	M_3C + MC	M_3C + MC + $M_{23}C_6$
650 °C – 390 min	18.7	N/A	N/A
715 °C – 15 min	18.7	M_3C + MC	M_3C + MC
715 °C – 45 min	19.1	M_3C + MC	M_3C + MC
715 °C – 180 min	19.7	M_3C + MC	M_3C + MC

A factor that may inhibit the formation of $M_{23}C_6$ is the amount of Mo content left in solid solution. Figure 5.14 presents the driving force map for $M_{23}C_6$ as a function of Mo content and temperature. The driving force is defined as the magnitude of the difference in initial and final free energies for carbide formation. Given a large number of MC precipitates in the tempered steels, the Mo content in the ferrite phase is reduced so that the driving force for $M_{23}C_6$ formation is low. A decreased precipitation-driving force would suppress the nucleation of $M_{23}C_6$. A similar finding was described in the study by Jenkins et al [3], where the V addition indirectly suppressed the precipitation of $M_{23}C_6$ by absorbing Mo into (V, Mo)C carbides.
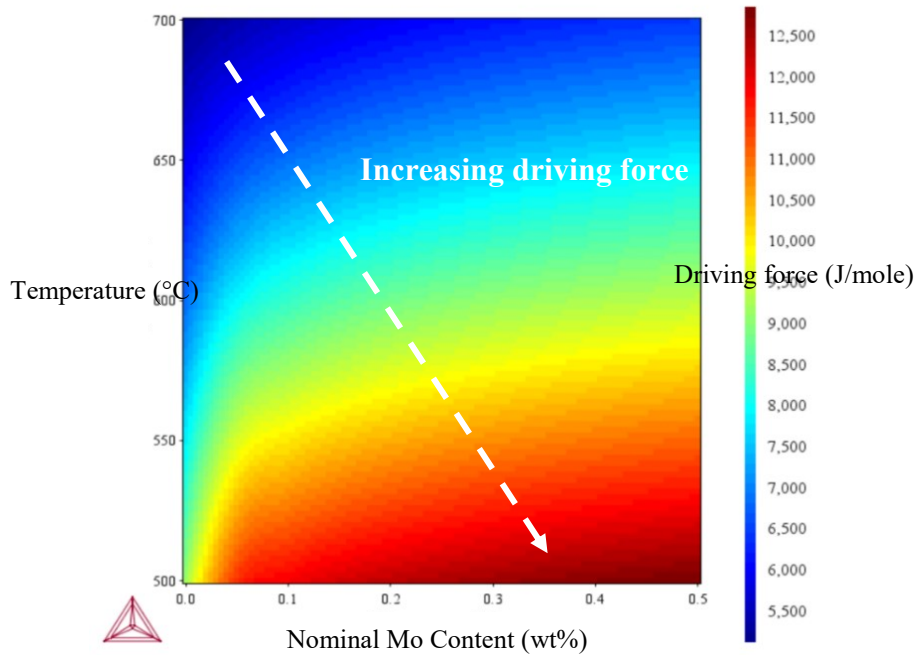
Figure 5.14. Driving force for precipitation for $M_{23}C_6$ with respect to varying nominal weight percent of Mo and tempering temperature.

5.5.2 STEM characterization of carbide composition

STEM-EDS chemical composition measurements were conducted on the Fe-based carbides of the tempered 0.52 wt% Cr and 0.77 wt% Cr steels at 600 °C, 650 °C, and 715 °C (45 min). Only the weight fractions of the two major metallic elements of the measured carbides (Fe and Cr) were considered.

Figure 5.15 illustrates the evolution of the amount of Fe and Cr (wt%) for carbides with increasing tempering temperature from 600 °C to 715 °C (45 min) for 0.52 wt% Cr and 0.77 wt% Cr steels. The carbides analyzed were all M_3C (alloyed cementite) particles, as M_3C is the only type of Fe-based carbide precipitated at 600 °C and 715 °C. Each point represents the metallic composition of one precipitate. It can be seen that the nominal Cr content has a dominant influence on the chemical composition of M_3C carbides. Specifically, more Cr atoms were partitioned into M_3C as the nominal Cr content increases from 0.52 to 0.77 wt%. Moreover, M_3C carbides become enriched in Cr and depleted in Fe with increasing temperature from 600 °C to 715 °C. This was expected since Cr in the tempered P110 steel does not form its own carbide according to the

equilibrium phase diagram (Figure 5.4); it has a high tendency to alloy with existing stable carbides (i.e., M_3C). Published studies provide evidence of Cr partitioning to cementite during tempering [69,105,70].
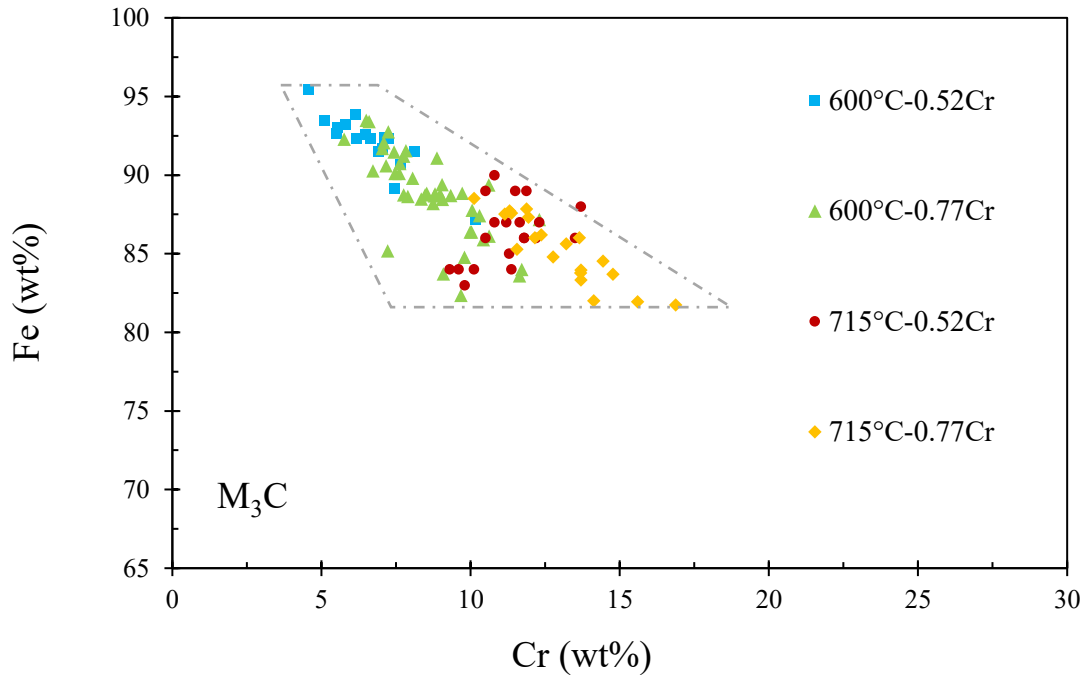
Figure 5.15. Fe and Cr content in the M constituent of M_3C of tempered 0.52 wt% Cr and 0.77 wt% Cr plate after 600 °C and 715 °C for 45 min.

Figure 5.16 shows the Fe and Cr contents for carbides from tempered 0.52 wt% Cr and 0.77 wt% Cr steels at 650 °C (45 min) along with the equilibrium composition of $M_{23}C_6$ predicted by Thermo-Calc. An alloy system with the composition of the 0.77 wt% Cr P110 steel was considered for the calculation. Since it is difficult to distinguish $M_{23}C_6$ from M_3C particles simply by their shape and size, some $M_{23}C_6$ carbides were inevitably included during the STEM-EDS measurements.

As shown in Figure 5.16, most carbides have reached the same level of Cr enrichment as the M_3C particles of tempered specimens after 715 °C for 45 min (Figure 5.15). Additionally, a large number of carbides with relatively high Cr and low Fe (wt%) were observed in the 0.77 wt% Cr tempered samples (650 °C for 45 min). These carbides are likely to be the previously identified $M_{23}C_6$ particles (Figure 5.13 and Table 5.2). It is interesting to note that these particles have an

average of 5 wt% measured Mo content, which is much smaller than the predicted 11 wt% equilibrium Mo content by Thermo-Calc simulation. Finally, the tempered 0.52 wt% Cr sample (650 °C for 45 min) contained much fewer particles with high Cr wt% (Figure 5.16) and no identified $M_{23}C_6$ particles (Table 5.2).
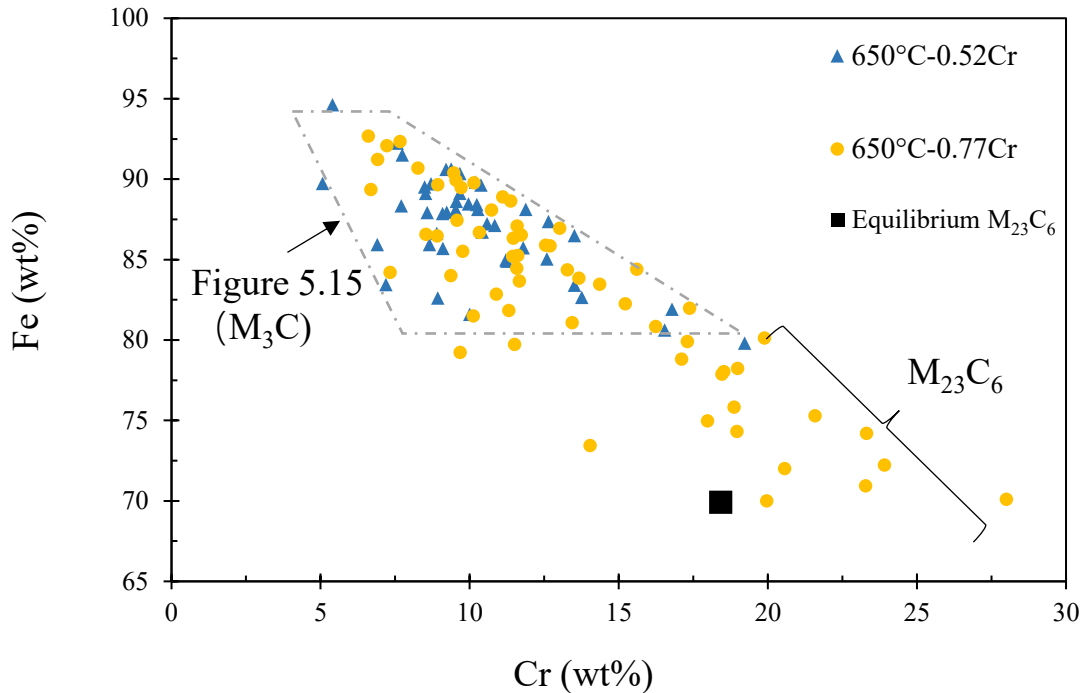
Figure 5.16. Fe and Cr content of the carbides for tempered 0.52 wt% Cr and 0.77 wt% Cr steels after 650 °C for 45 min. The equilibrium Fe and Cr content of $M_{23}C_6$ are predicted with Thermo-Calc.

Based on the observations from Figures 5.15 and 5.16, it is clear that the amount of Cr that partitions to M_3C carbides generally increases with increasing nominal Cr content and tempering temperature (from 600 °C to 715 °C). The M_3C composition after tempering at 650 °C (45 min) was rather scattered. For instance, M_3C composition varied from (7 wt% Cr - 93 wt% Fe) to (17 wt% Cr - 83 wt% Fe) (Figure 5.16). The reason may be related to the low Cr diffusion rate at 650 °C. To be more specific, Cr atoms can easily partition into the M_3C carbides located at grain boundaries (i.e., inter-lath and PAG boundaries) since the diffusion rate at grain boundaries is high, whereas the M_3C carbides located within the ferrite matrix require a longer time to become enriched in Cr. Finally, because of the lower diffusion and partitioning coefficient for Mo in

tempered martensite compare to Cr, a relatively low Mo content (< 5.0 wt%) was found in the M_3C particles [65].

$M_{23}C_6$ carbides were only identified in the tempered 0.77 wt% Cr sample (650 °C for 45 min) but not in the 0.52 wt% Cr sample. Published studies indicate that the nucleation, equilibrium, and coarsening of $M_{23}C_6$ carbides are all achieved by attracting Fe and Cr atoms (both are major constituents of $M_{23}C_6$) from ferrite solution and/or the neighboring less stable carbides (i.e., M_3C in this study) [98,56,62]. Thus, the higher Cr content in both ferrite solution and M_3C particles (Figure 5.16 and 5.17) can provide an opportunity for the nucleation of $M_{23}C_6$ particles in the 0.77 wt% Cr steels. No $M_{23}C_6$ particles were identified in the 0.52 wt% Cr steel tempered at 650 °C for 45 min (Figure 5.13), indicating that nucleation was restrained by the more limited Cr content. This speculation is supported by the work of Jenkins et al [3].

Some deviation in Cr and Fe content between the measured and predicted equilibrium composition of $M_{23}C_6$ was observed in Figure 5.16. The transition from M_3C to a more thermodynamically stable alloy carbide (i.e., $M_{23}C_6$) can be very slow due to the long-range of diffusion of Mo and Cr atoms. It is anticipated that the equilibrium composition will be reached after a sufficiently long holding time. Furthermore, the average measured Mo content (5 wt%) was lower than the equilibrium Mo content (11 wt%) of $M_{23}C_6$ carbides. This can be attributed to the reduced actual Mo content in the ferrite matrix through the precipitation of (Ti, Mo)C.

5.5.3 FESEM characterization of carbide morphology

Figure 5.17 and 5.18 show FESEM micrographs of the carbide morphology after different tempering conditions for 0.52 wt% Cr samples and 0.77 wt% Cr samples, respectively. According to the previous TEM characterization, the MC (< 20 nm) and $M_{23}C_6$ (~ 50 nm) carbides are much finer than the M_3C particles. Therefore, the carbides observed in the FESEM micrographs are predominantly M_3C.

After tempering at 600 °C for 45 min, fine carbides, including elliptical-shaped and needle-shaped carbides, formed within the martensite laths in 0.52 wt% Cr and 0.77 wt% Cr steels. Some relatively large (≈ 100 nm) and elliptical-shaped carbides are presented at PAG boundaries (i.e., HAGB with MA>15°). After tempering at 650 °C for 45 min, large quantities of rod-shaped

carbides along the lath (i.e., LAGB with MA<15°) and PAG boundaries. Carbides precipitated at lath boundaries are generally larger relative to the particles in matrix. In addition, some spherical carbides at grain boundaries were observed. After tempering at 715 °C for 45 min, there were some rod-shaped carbides distributed at the boundaries of martensite laths and PAG. Relatively finer carbides (<70 nm) were precipitated within the laths. Carbide coarsening becomes more strikingly evident, in particular for the carbides located at PAG boundaries. With extended tempering time from 45 min to 180 min at 715 °C, individual carbide size increased, whereas the number density decreased considerably, indicating continuous carbide coarsening at the expense of dissolution of the finer carbides (i.e., Ostwald ripening). The coarsened and spherical carbides are mainly located at grain boundaries, with few carbides in the ferrite matrix. The mechanism behind the high spheroidization and coarsening rate of carbides at grain boundaries are due to faster short circuit diffusion.

No prominent difference in the size, shape, and location of carbides between 0.52 wt% Cr and 0.77 wt% Cr steels was found. It is noteworthy that the errors from the chemical etching method were minimized by keeping the etching time and etched thickness the same. In subsequent sections, the carbide size, volume fraction, and number density are quantitatively studied.
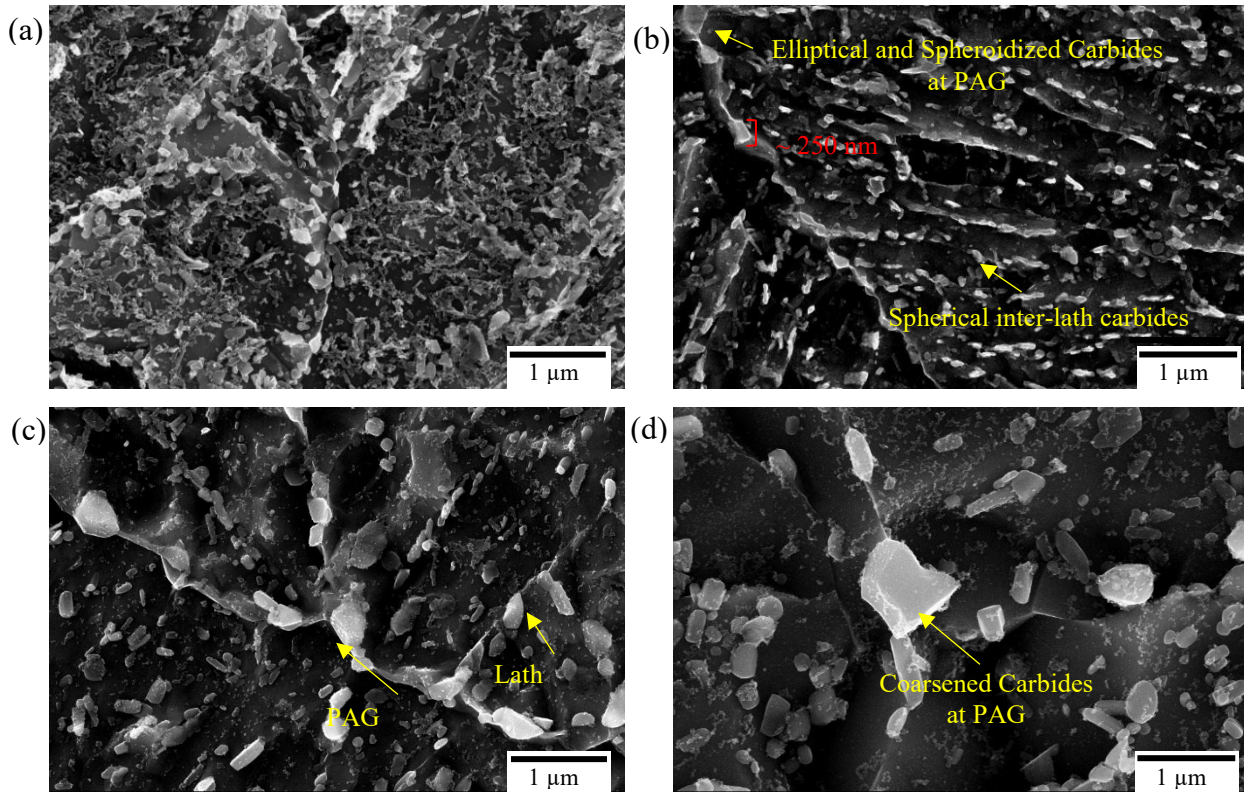
Figure 5.17. FESEM SE images of M₃C particles after tempering of 0.52 wt% Cr samples at (a) 600 °C - 45 min, (b) 650 °C - 45 min, (c) 715 °C - 45 min, and (d) 715 °C - 180 min.
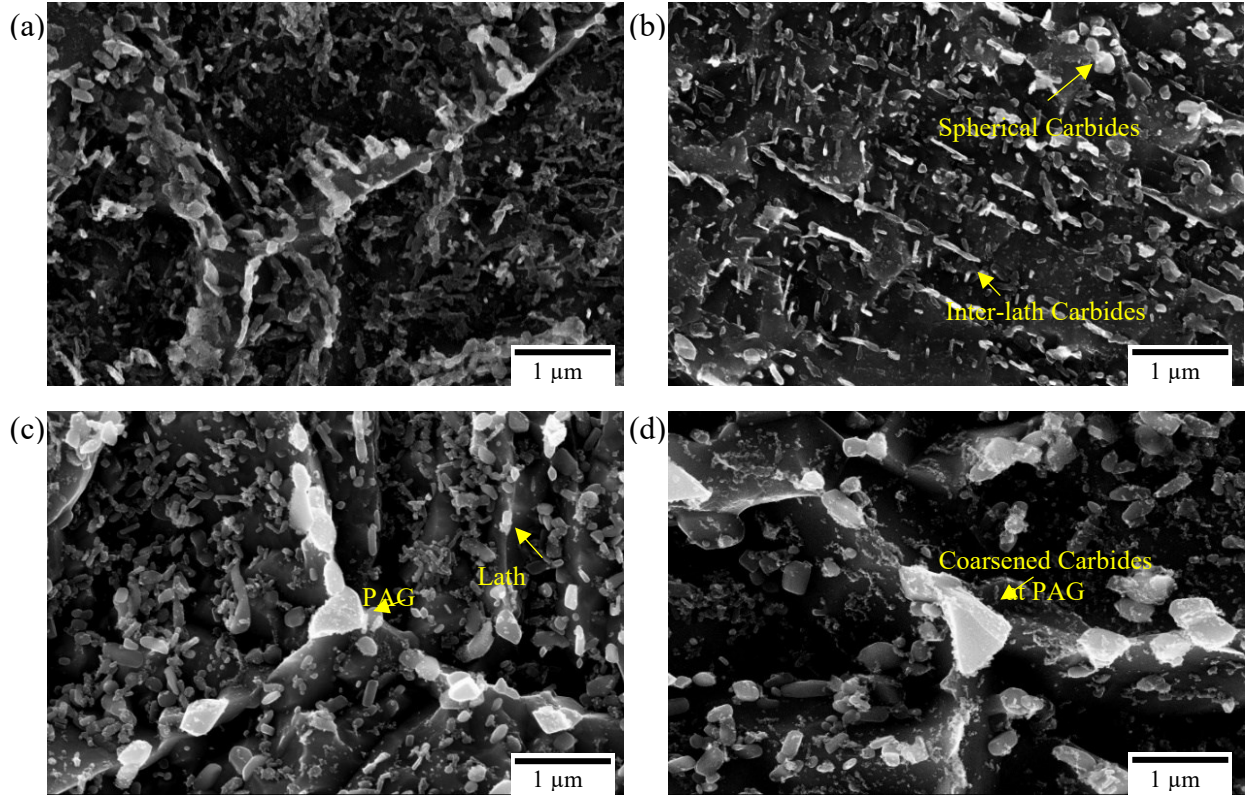
Figure 5.18. FESEM SE images of M₃C particles after tempering of 0.77 wt% Cr samples at (a) 600 °C - 45 min, (b) 650 °C - 45 min, (c) 715 °C - 45 min, and (d) 715 °C - 180 min.

5.5.4 STEM quantification of carbide size, volume fraction, and number density

TEM analysis was conducted on carbon replica samples to quantitatively evaluate the effect of tempering conditions and alloying composition on carbide morphology. Carbides with various shapes (e.g., rod, elliptical, and spherical shape) were all considered with the spherical equivalent diameter (*ED*) regarded as the particle size. The volume fraction of the carbides, f_v, was calculated using the Equation (5.1), where N is the number of particles per area, *ED* is equivalent diameter, S is the particle area, and S_0 is the total analyzed area [97,106]:

$$f_v = \frac{N\frac{4\pi}{3}}{S_0 D}\left(\frac{D}{2}\right)^3 = \frac{N\pi D^2}{6S_0} = \frac{2NS}{3S_0}$$

(5.1)

The average *ED* and f_v for M₃C particles were determined from 200-400 random particles for each specimen. Since it is difficult to distinguish M₃C and M₂₃C₆ simply by their shape and size, some

86

$M_{23}C_6$ carbides were inevitably included in the measurements of samples tempered at 650 °C for 45 min.

5.5.4.1 Quantification of carbides by equivalent diameter (ED)

The number fractions of particles for different *ED* sizes of 0.52 wt% Cr samples tempered at 600 °C, 650 °C, and 715 °C for 45 min are shown in Figure 5.19. With an increase in tempering temperature, *ED* values increase. Specifically, the size distribution in the tempered specimens at 715 °C (45 min) exhibits a much higher fraction of particles with *ED* >100 nm than those tempered at 600 °C or 650 °C (45 min). It is noteworthy that the coarse carbides with a size ranging from 200 to 300 nm account for only about 1% of particles of samples tempered at 650 °C (45 min). According to the FESEM micrographs in Figure 5.17 (b) and 5.18 (b), the carbides representing 1% fraction were observed to have an elliptical and/or spheroidal shape, forming at PAGBs as opposed to within the ferrite matrix. This can be explained in terms of the higher diffusivity of Cr and Mo along the PAGBs than through the matrix.
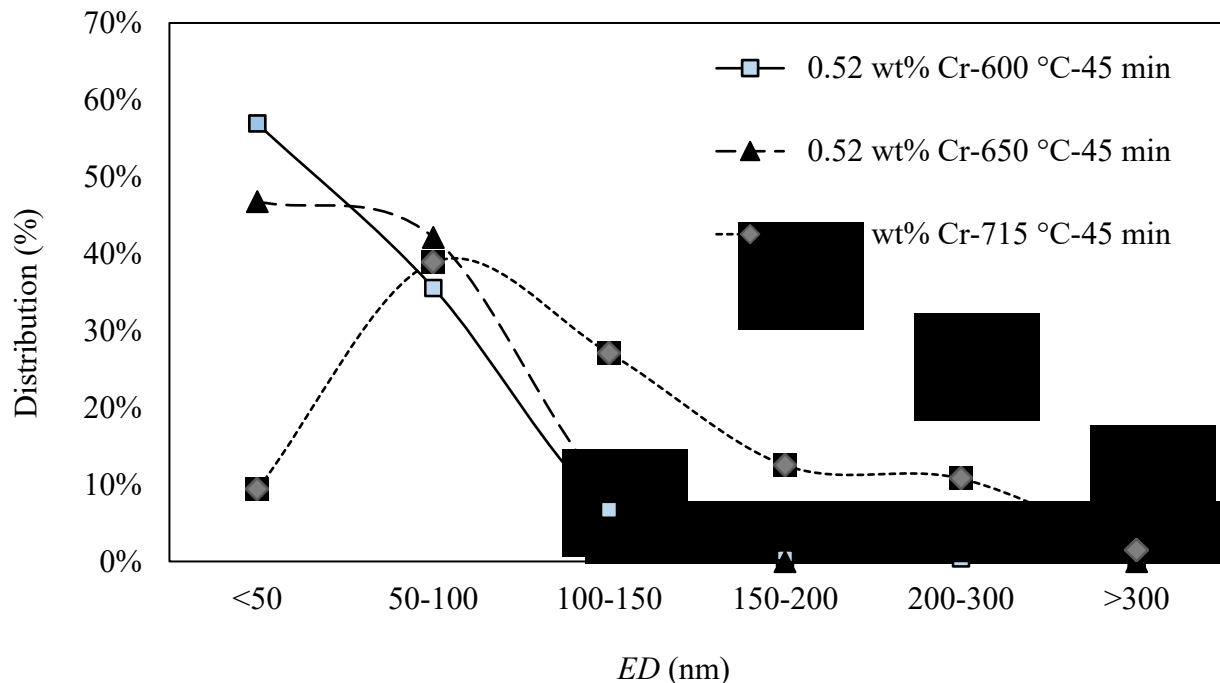
Figure 5.19. Carbide size distribution maps for the 0.52 wt% Cr steel tempered at 600 °C, 650 °C, and 715 °C for 45 min.

The PM (Property model) module of Thermo-Calc software (version 10.0) was used to predict the coarsening rate coefficient of M_3C during tempering at different temperatures. Coarsening rate is defined as the rate of diffusion controlled coarsening of precipitates (with the form of Equation 2.13). The coarsening model calculates the coarsening rate coefficient [m^3/s] of M_3C phase in the selected matrix phase (i.e., BCC), assuming spherical geometry of the precipitating phase. It is noteworthy that the thermodynamic data (from TCFE10 Steels/Fe-Alloys v10.1 database) includes molar volume of the matrix and precipitates phases as well as the kinetic data (from MOBFE3 Steels/Fe-Alloys Mobility v3.0 database) with mobilities for the matrix phase were required for the simulation. Figure 5.20 shows the coarsening rate of M_3C as a function of tempering temperature. The coarsening rate of M_3C exponentially increase with increasing temperature of temperature. Additionally, increasing Cr addition from 0.52 wt% to 0.77 wt% reduces the M_3C coarsening rate.

Average *ED* values of particles of samples tempered from six different conditions were further calculated and are provided as a function of tempering time and temperature in Figure 5.21. As expected, the measured average *ED* value increases with increasing time and/or temperature of tempering, which is approximately consistent with the Thermo-Calc simulation (Figure 5.20) in that the coarsening rate increases with an increase in temperature. The reason lies in the increasing diffusivity of Fe, Cr, and Mo atoms in the ferrite matrix with an increase in temperature. Specifically, the M_3C particles can easily reach a 100 nm size after tempering at 715 ˚C for 45 min, whereas the particles required as long as 390 min to reach the average size of 100 nm at 650 ˚C. As previously shown in Figure 5.19, after tempering at 650 °C for 45 min, a large quantity of particles with size are smaller than 100 nm (about 89%) which reduced the average *ED* value of the tempered sample. In contrast, at 715 °C, higher elemental diffusion rates increased the overall carbide coarsening rate, leading to a much higher average *ED* for the carbides after tempering at 715 °C for 45 min. Furthermore, since the precipitates with size larger than 70 nm normally have lower H trapping ability due to their incoherent interfaces with the ferrite matrix [79], tempering at low temperature (e.g., 600 °C and 650 °C) or at high temperature for a short time (e.g., 715°C for 15 min) to enhance the hydrogen trapping ability is desirable.
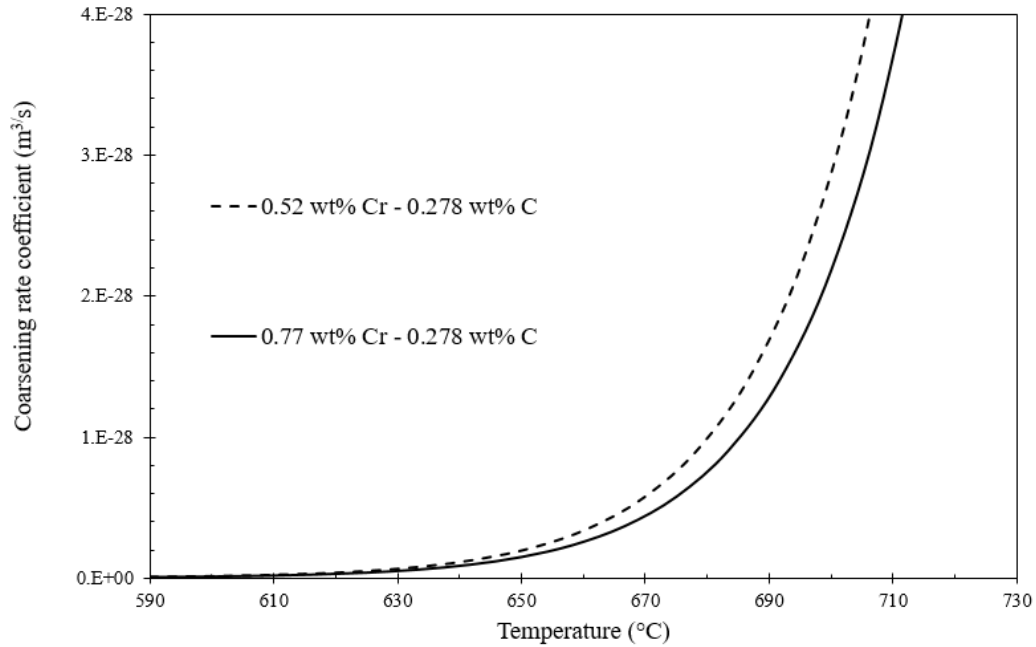
Figure 5.20. Calculated coarsening rate coefficient of M$_3$C particles considering the composition of 0.77 wt% Cr P110 steel using Thermo-Calc.
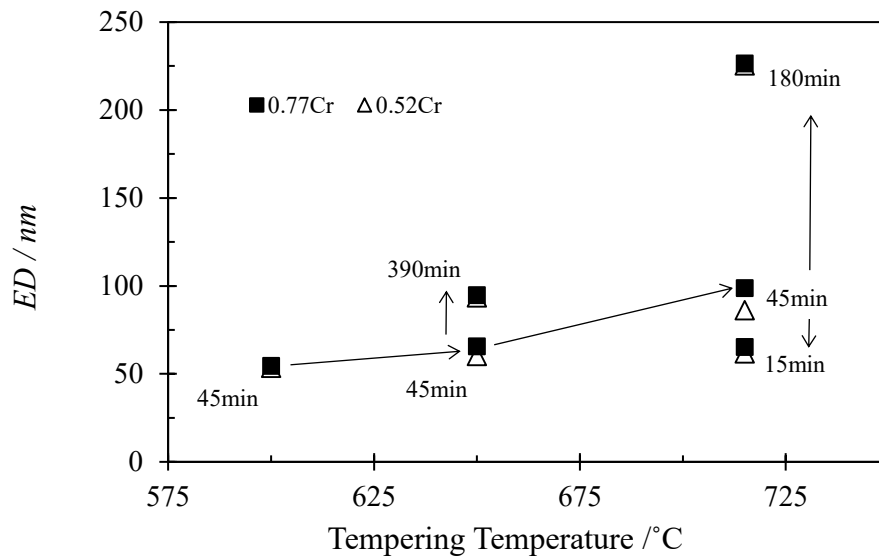
Figure 5.21. Experimental average *ED* of M$_3$C particles for the tempered 0.52 wt% Cr and 0.77 wt% Cr samples at six different conditions.

Figure 5.21 indicates that tempered 0.77 wt% Cr specimens contain particles (i.e., predominantly M_3C/ alloyed cementite) with slightly higher average *ED* values than the tempered 0.52 wt% Cr steels. However, the differences in average *ED* between the two steels are too small to determine the effect of nominal Cr and C content on carbide coarsening. The potential effects of C and Cr content on M_3C coarsening are:

[1] Coarsening of M_3C can be retarded by Cr addition. This phenomenon is consistent with the simulation result (Figure 5.20) in which higher Cr addition leads to lower M_3C coarsening rate. Two proposed mechanisms are:

   a. M_3C coarsening can be retarded by the sluggish diffusing alloying element (e.g., Cr), particularly when particle reaches a specific large size [107,67,108]. However, the effect of this can be very limited as the M_3C particles were enriched in Cr even after tempering at 650 °C for 45 min (Figure 5.16).

   b. The dissolution of strong carbide formers (i.e., Cr) in the matrix attracts C atoms, which reduces the diffusivity and activity of C to support coarsening [6,109]. Nazemi and Hamel-Akré et al. indicate that even small additions of substitutional elements (e.g., Cr and Mo with lower diffusivity than C) reduce the coarsening kinetics [65].

[2] According to Bjorklund and Donaghey et al., M_3C coarsening is dominantly controlled by C diffusion from the ferrite phase [67]. Ning and Yue et al. indicated that the coarsening rate of M_3C is proportional to the concentration of C in ferrite [68].

In summary, it is speculated that even though the higher nominal C content (0.278 wt% versus 0.255 wt%) of 0.77 wt% Cr steel favors M_3C coarsening, its higher Cr content inhibited coarsening. The effects of Cr and C content offset each other and, as a consequence, led to the similar average *ED* of M_3C.

5.5.4.2 Quantification of carbides by volume fraction (fv)

Assuming that the total amount of carbides can precipitate under equilibrium and stoichiometric conditions, the upper bound value for the volume fraction (theoretically calculated maximum value) of M$_3$C particles in the 0.77 wt% Cr steel was calculated using Equation 5.1 and 5.2. The weight fraction of cementite (wt%), [Fe$_3$C], was first estimated according to the lever rule:

$$[Fe_3C] = 1 - \frac{6.69 - (\% \ C \ in \ \gamma)}{6.69 - 0.022} \qquad \text{(Equation 5.1)}$$

The volume fraction of cementite, f_v, was then calculated according to Equation 5.2:

$$f_v = \frac{[Fe_3C]}{100} \frac{\rho_{Fe}}{\rho_{Fe_3C}} \qquad \text{(Equation 5.2)}$$

where ρ_{Fe} is the density of the low alloy steel (approximately 7.90 g cm^{-3}), and ρ_{Fe_3C} is the density of cementite (approximately 7.69 g cm^{-3}) [110,111]. According to Figures 5.15 and 5.16, tempered M$_3$C particles predominantly contain Fe and Cr atoms (they have similar atomic masses) with less than 5 wt% Mo content. Therefore, the difference between the actual density of M$_3$C and Fe$_3$C (cementite) was assumed to be negligible during this calculation.

Based on Equation (5.1) and (5.2), 0.0398 was calculated as the upper bound value of M$_3$C f_v in the 0.77 wt% Cr steel. Additionally, Thermo-Calc simulation (TCFE10 database) was also conducted to predict the equilibrium f_v of M$_3$C in the system with the composition of 0.77 wt% Cr steel at 600 °C, 650 °C, and 715 °C. The values are presented in Figure 5.22.

Figure 5.22 shows the experimental volume fraction (f_v) as a function of tempering time and temperature, along with the upper bound and Thermo-Calc simulated values of volume fraction. As expected, the experimental volume fraction from carbon replicas overestimated the actual values due to the etching effect (over three times larger than the maximum/upper bound value). Although the TEM measurements based on replicas cannot be used to accurately determine the actual volume fraction, the measured variation/trend of volume fraction is still of some value.

As shown in Figure 5.22, the volume fraction for M$_3$C particles increases with tempering temperature from 600 °C to 715 °C. This general trend is due to the diffusion of elements dissolved in ferrite matrix, and is consistent with the equilibrium M$_3$C fraction predicted by Thermo-Calc

simulations (Figure 5.4). In addition, the volume fraction is sensitive to an increase in tempering temperature from 600 °C to 650 °C, whereas the volume fraction trend flattens out as temperature is further increased to 715 °C or holding time extended to 390 min. This observation is likely due to the precipitation of M_3C approximately reaching equilibrium with ferrite after tempering at 650 °C for 45 min. As volume fraction is a function of particle number density and average size, this result also provides evidence of the occurrence of Ostwald ripening during tempering over the range from 650 °C to 715 °C, where the M_3C particle size increases as the number density decrease. Finally, the tempered specimens (650 °C - 45 min) displayed relatively low average *ED* (Figure 5.20) and high volume fraction (Figure 5.22) of carbides. Therefore, it is expected that the sample tempered at this condition can possess higher hydrogen trapping capacity comparing to samples tempered from the other conditions.
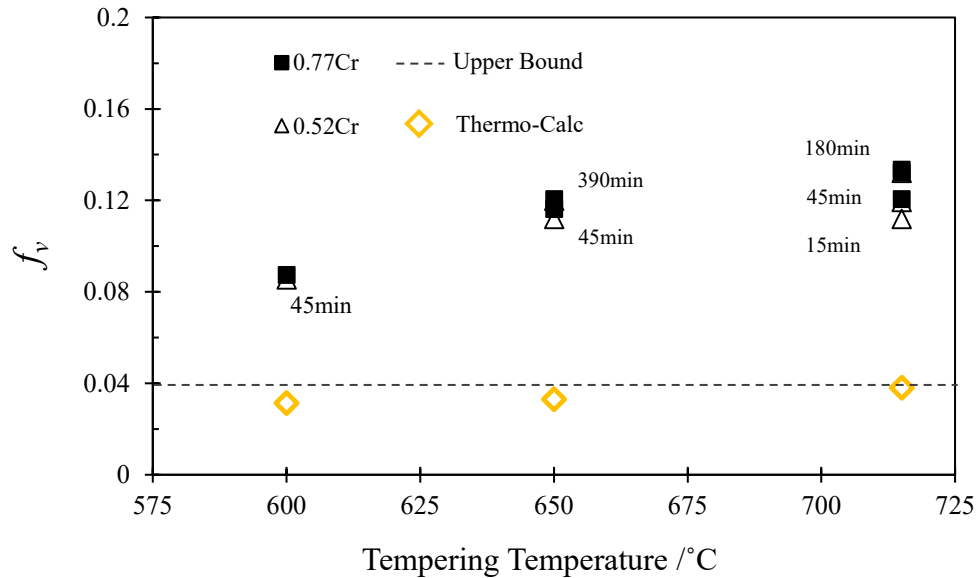
Figure 5.22. Experimental volume fraction (f_v) for M_3C particles for the tempered 0.52 wt% Cr and 0.77 wt% Cr samples. The calculated upper bound and Thermo-Calc simulated values of f_v in the 0.77 wt% Cr steel are highlighted by a dotted line and yellow diamonds, respectively.

Another important trend that can be seen in Figure 5.22 is that the tempered 0.77 wt% Cr steel contains a slightly higher volume fraction of M_3C particles than the tempered 0.52 wt% Cr steel in all the tempered samples. As the equilibrium M_3C fraction is directly proportional to the nominal

C concentration, this observation can be explained in terms of the marginally higher nominal C content (0.278 wt% C) of the 0.77 wt% Cr steel than the 0.255 wt% C of the 0.52 wt% Cr steel.

The carbide volume fractions increase with prolonged holding time. However, the magnitude of the increase is not so obvious (Figure 5.22). This indicates that the carbides precipitated after 650 °C for 45 min and/or 715 °C for 15 min were approaching equilibrium conditions with ferrite. Figure 5.23 presents STEM-BF micrographs of carbide morphology. After extending the tempering time from 45 min to 390 min (650 °C), individual particles coarsened at an approximately constant volume fraction (0.11 to 0.12). The coarsened elliptical particles, which were confirmed as M_3C, make up most of the carbide volume fraction.
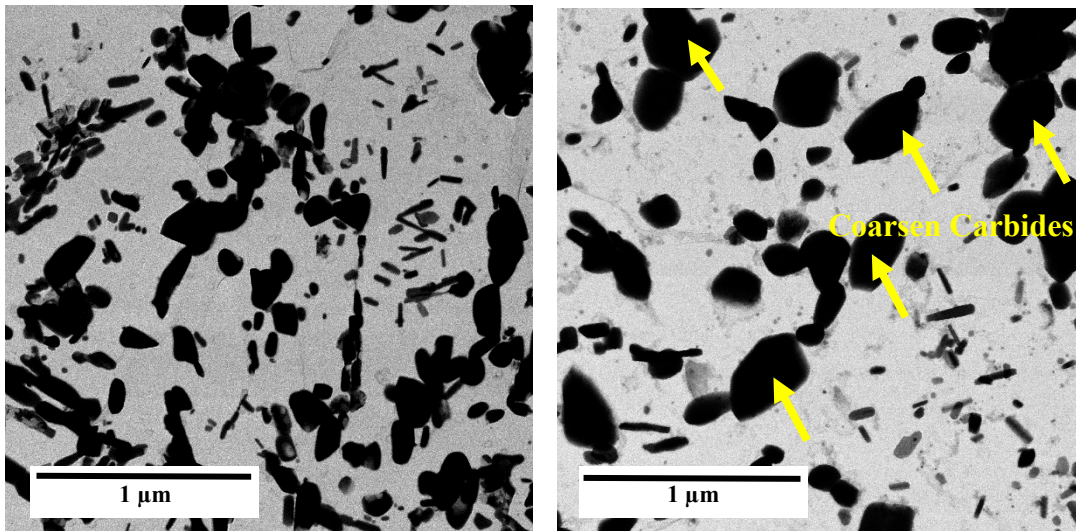
Figure 5.23. STEM BF images illustrating the morphology of precipitates of the 0.52 wt% Cr steel after tempering at 650 °C for (a) 45 min and (b) 390 min.

5.5.4.3 Quantification of carbides by number density (ρ)

By measuring the number of particles per analyzed area from the HAADF micrograph, the overall number density was estimated using Image J software. Figure 5.24 presents STEM-HAADF micrographs of carbide morphology as well as the overall particle number density (ρ) of 0.77 wt% Cr steels after tempering at three different conditions (i.e., 650 °C - 45 min, 650 °C - 390 min, and 715 °C - 15 min).

As shown in Figure 5.24 (a) and (b), with increasing tempering time (from 45 min to 390 min) at 650 °C, there is a sharp reduction in number density from $51/\mu m^2$ to $28/\mu m^2$. Additionally, according to Figure 5.24 (b), none or few fine particles were found near the coarsened elliptical carbides (300-500 nm), suggesting the dissolution of smaller carbides takes place in the vicinity of coarsening carbides. This observation, in which larger elliptical-shaped carbides grown at the expense of the smaller ones, is an indication of the Ostwald ripening.

# 698 particles per 13.7 μm²	# 375 particles per 13.7 μm²	#781 particles per 13.7 μm²
$\rho = 51/\mu m^2$	$\rho = 28/\mu m^2$	$\rho = 57/\mu m^2$
HJ=17.9	HJ=18.7	HJ=18.7
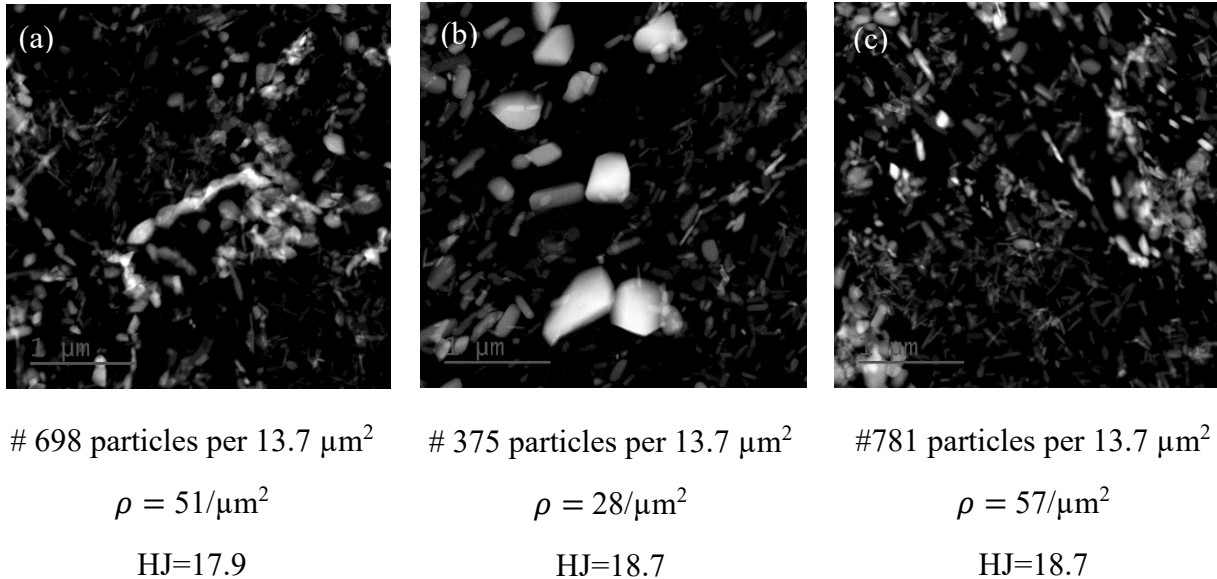
Figure 5.24. STEM HAADF images illustrating the shape and density of precipitates of the 0.77 wt% Cr steel after tempering at (a) 650 °C - 45 min, (b) 650 °C - 390 min, and (c) 715 °C - 15 min.

In contrast to the tempered sample from 650 °C for 390 min (Figure 5.24 (b)), the sample tempered at 715 °C for 15 min contains much finer and more densely spaced carbides (Figure 5.24 (c)). Thus, two different tempering conditions, 650 °C-390 min and 715 °C-15 min with the same HJ parameter (18.7) and similar micro-hardness (~258.0 Hv), can exhibit distinctive carbide morphologies. Figure 5.24 (c) also demonstrates that the studied P110 steels can be tempered at high temperatures (e.g., 715 °C) for a short time (e.g., 15 min) to obtain a microstructure with relatively fine (< 61 nm) and densely distributed ($57/\mu m^2$) carbides.

5.5.5 Summary of carbide morphology

STEM-EDS analysis of carbides in tempered samples from 600 °C, 650 °C, and 715 °C for 45 min (Figures 5.15 and 5.16) indicates that the majority of carbides were enriched in Cr atoms after tempering at 650 °C (45 min). When tempering at an extended time (T = 650 °C, t > 45min) or higher temperature (T > 650 °C, t = 45min), volume fraction remains approximately constant (despite some slight increase), whereas significant carbide coarsening proceeds as reflected by the increase in average particle size and the decrease in number density (Ostwald ripening). It can be concluded that after tempering at 650 °C for 45 min, there are less amount of alloy elements (i.e., Cr and Mo) left from the matrix that can diffuse into carbides, and the existing carbides were approaching equilibrium conditions with ferrite at this condition. Any further tempering beyond this condition leads to the occurrence of Ostwald ripening.

5.6 Tensile Test Performance

Tensile tests were conducted on the 0.77 wt% Cr steel tempered under seven different conditions. Figure 5.25 (a) and (b) show stress-strain curves of the 0.77 wt% Cr steel tempered at different times (i.e., 715 °C for 15, 45, and 180 min) and temperatures (i.e., 600 °C, 650 °C, and 715 °C for 45 min), respectively. An increase in either tempering time or temperature is always accompanied by a decrease in both the ultimate tensile strength (UTS) and yield strength (YS) (Figure 5.25 (a) and (b)). In addition, all tensile curves show an upper yield point with an extended lower yield point; both features became more evident after tempering at relatively high temperatures (T> 650 °C). Specifically, the yielding features in the tempered specimens after 650 °C (45 min) and 715 °C (45 min) are distinct, with the latter exhibiting a much more prominent upper yield point and a higher magnitude of yield point elongation. This observation corresponds to a drastic decrease in mobile dislocations through the formation of Cottrell atmospheres during tempering.
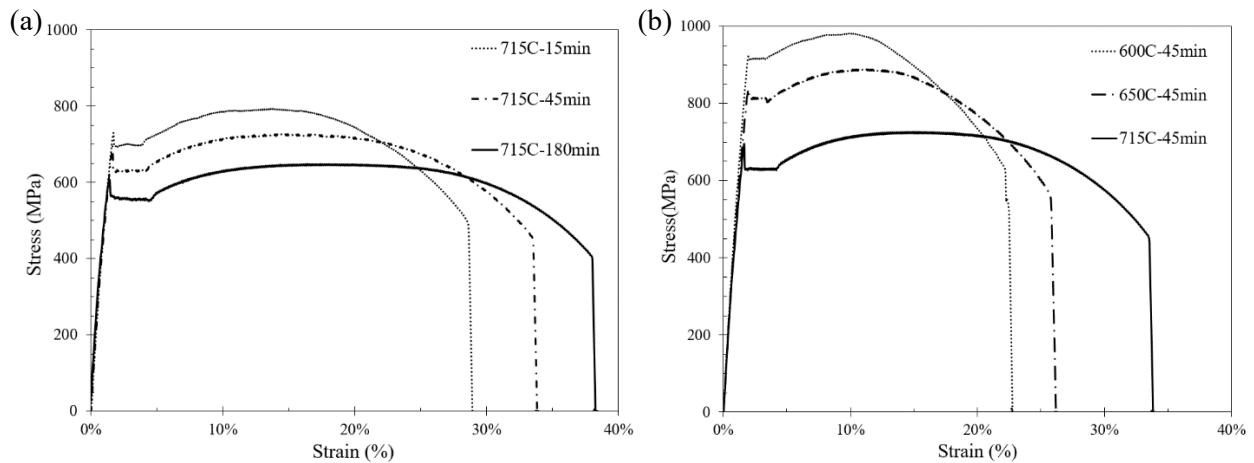
Figure 5.25. Stress-strain curves showing the effect of tempering (a) time and (b) temperature on tensile properties.

The measured values of UTS and YS as a function of the hardness are plotted in Figure 5.26 (exact values are tabulated in Appendix D). Linear equations were fitted to the data as indicated by the regression lines. Both the linear relationships and R^2 value are included in Figure 5.26.
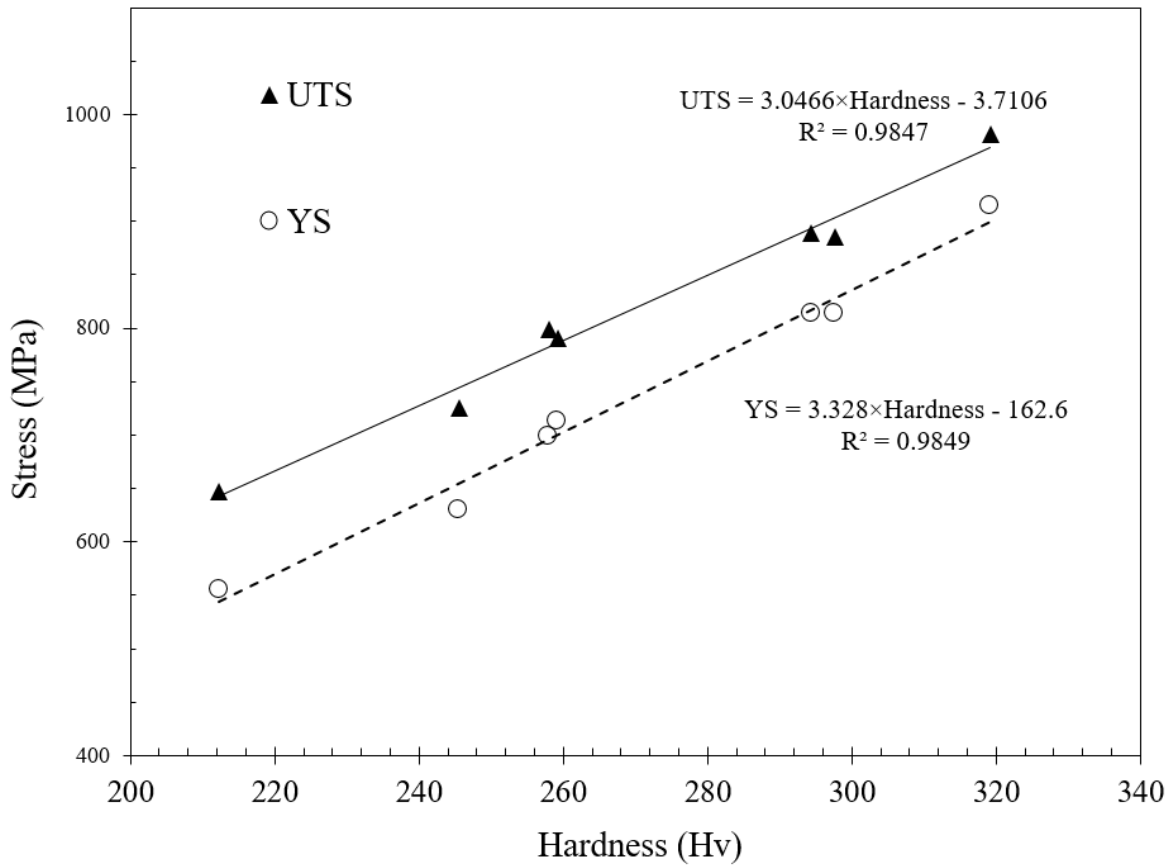
Figure 5.26. Measured UTS (MPa), and YS (MPa) as a function of hardness (Hv).

The UTS, YS, and total percent elongation (%EL) as a function of the HJ parameter are plotted in Figure 5.27 (a). The HJ parameter can be used to predict hardness values and tensile properties (i.e., UTS, YS, and %EL). As expected, the %EL increases with increasing HJ parameter, while UTS and YS values decrease.

Figure 5.27 (a) also shows that in order to produce P110 steel that meets the specified minimum yield strength (SMYS) of 110 KSI (758 MPa) from the API 5CT standard, tempering should be conducted at conditions with HJ lower than 18.4 [7]. For standard tempering times of 15 min and 45 min, HJ < 18.4 corresponds to temperatures lower than 700 °C and 675 °C, respectively. As indicated in Chapter 5.5.5, unless the tempering time is short, the temperature should not exceed 650 °C to avoid significant carbide-coarsening. The tempered particles from 715 °C for 15 min are much finer (average ED <60 nm) relative to the tempered particles from 675 °C for 45 min (60 < average ED < 100 nm); both values were extrapolated from Figure 5.23. Published studies indicate that an increasing number of finer precipitates (< 70 nm) can enhance the H trapping ability and improve the strength via dispersion strengthening [79,81]. Thus, tempering at high temperature for a short time (i.e., 700 °C for 15 min) to enhance H trapping ability is a feasible choice.

Figure 5.27 (b) and (c) show the stress-strain curves for different tempering conditions with the same HJ value. It is interesting to note that two distinctive tempering conditions with the same or similar HJ values displayed approximately the same tensile properties.
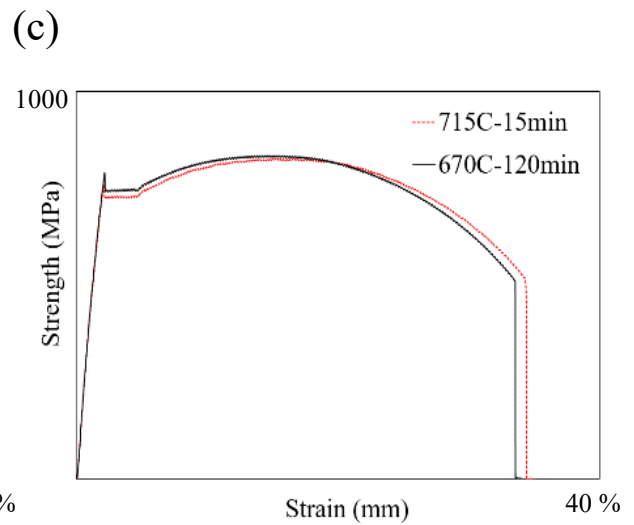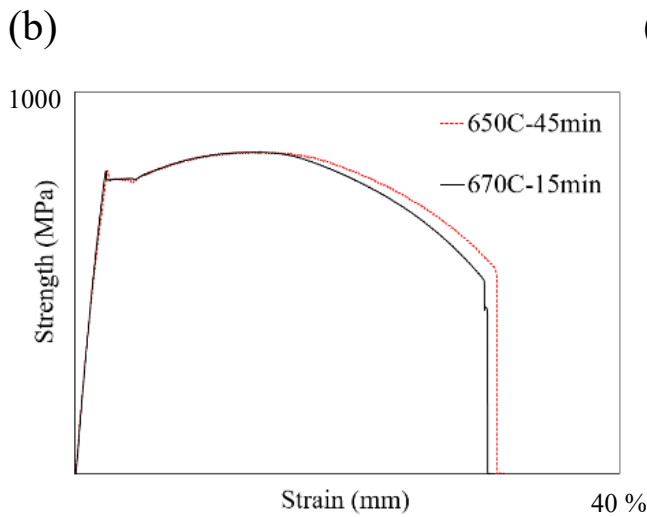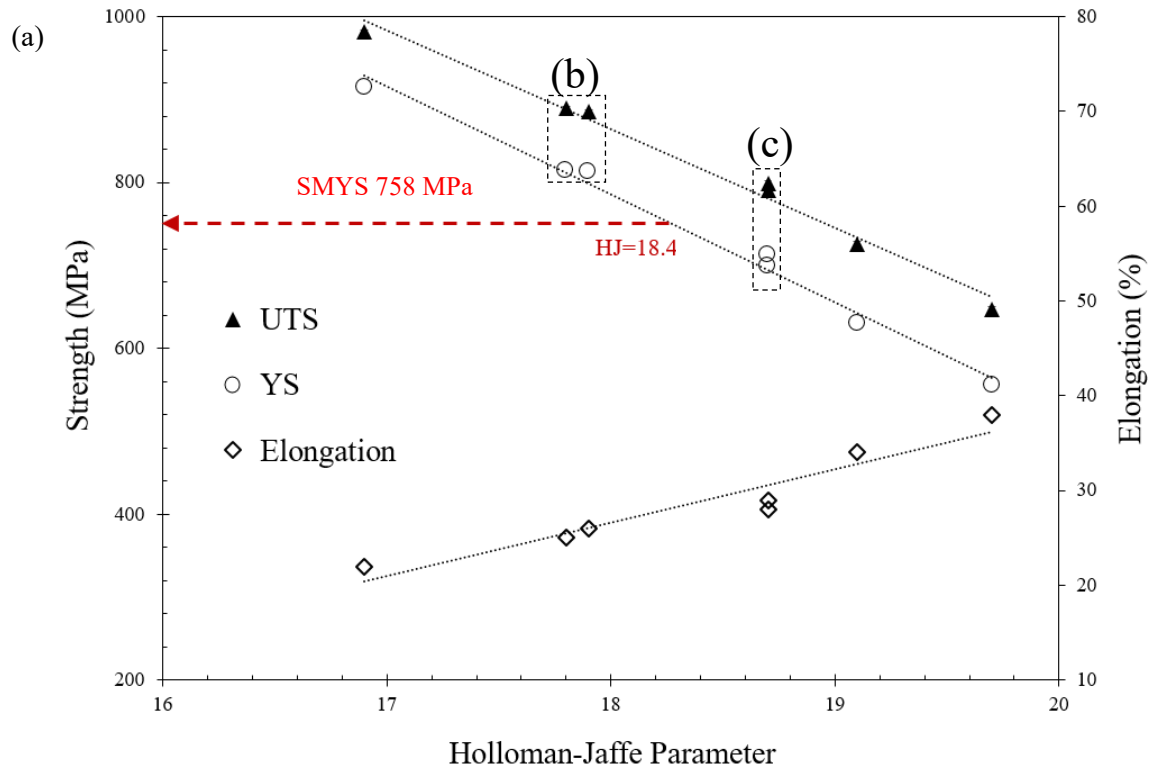
Figure 5.27. (a) Variation of tensile properties with tempering parameters. (b) Stress-strain curves for two samples after equivalent tempering (HJ=17.8). (c) Stress-strain curves of two samples after equivalent tempering (HJ=18.7).

Figure 5.28 (a) and (b) show SEM micrographs of the tensile fracture surfaces of the specimens tempered at the extremes of the HJ plot (i.e., at HJ = 16.9 and HJ = 19.7). The sample tempered at HJ = 16.9 (i.e., 600 °C-45 min) showed a moderately ductile fracture surface with a dominant shear fracture at a 45° angle, some necking, and a delaminated area close to crack propagation path. The shear fracture and necking are signs of ductile fracture, whereas the shear delamination is an indication of brittle behavior. In contrast, the specimen tempered at HJ = 19.7 (i.e., 715 °C-180 min) displayed a typical "cup-and-cone" ductile fracture surface. The differences between the two fracture surfaces correspond to the increase in ductility with the progression of tempering.
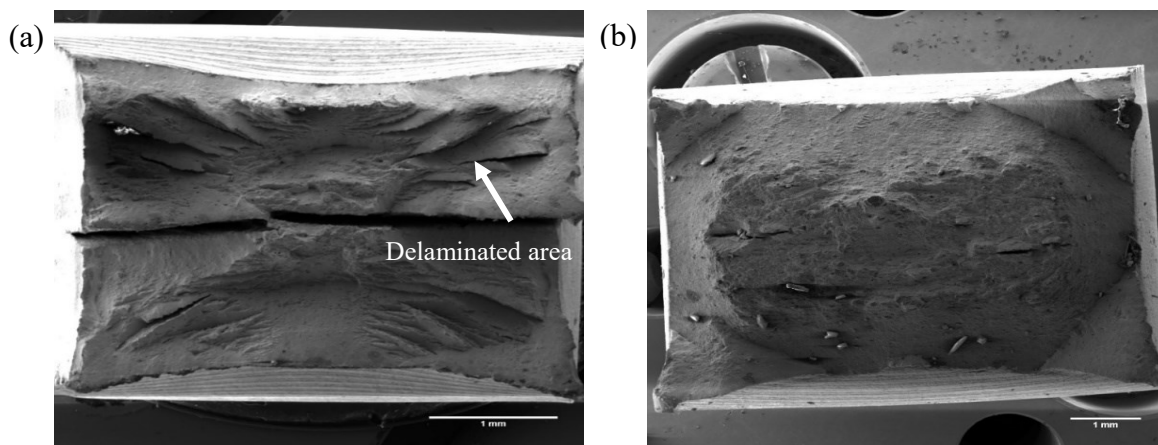
Figure 5.28. Tensile fracture morphologies of the 0.77 wt% Cr specimens tempered at (a) 600 °C-45 min and (b) 715 °C-180 min.

5.7 *Relationship between Carbide Morphology and Mechanical Properties*

The mechanical testing results indicate a drop in mechanical properties including UTS, YS, and hardness after tempering. In addition to the decrease in the quantity of interstitial C atoms in ferrite (via cementite precipitation), the evolution of the ferrite structure and carbide morphology during tempering also affects the mechanical properties.

During tempering at low temperatures (i.e., $T \leqslant 650°C$), fine (< 20 nm) MC carbides, as well as rod-shaped carbides with relatively high number density and volume fraction, have strong pinning action on grain boundaries. This partially offsets the softening caused by the decomposition of

martensite as reflected by the reduction in softening (Figure 5.2). Furthermore, the relatively fine carbide distribution can effectively hinder martensite lath coarsening and lead to high YS.

The spheroidization of carbides proceeds during tempering at 650 °C and then Ostwald ripening occurs at even higher temperatures and/or prolonged holding time. Coarsened carbides (with a lower number density) are less effective in pinning grain boundaries, thereby enabling the lath coarsening (Figure 5.3). Furthermore, according to the stress-strain curve shown in Figure 5.23 (a), during tempering at temperatures higher than 650 °C, the progression of dislocation annihilation is facilitated. Hence, the rapid decrease in hardness and YS after tempering in the higher temperature range can be attributed to the combined effects of carbide coarsening, dislocation annihilation, and lath structure coarsening.

Chapter 6

Conclusions and Recommendations

In this study, the effects of chromium (Cr) content, and to a lesser degree carbon (C) content, on the microstructural development during the quench and temper (Q&T) heat treatment of API-5CT-P110 casing steel were studied. Emphasis was put on the qualitative and quantitative study of the tempered carbide morphology including types, size, volume fraction, composition, and distribution. In the first section, the main findings obtained from the metallurgical characterization of as-rolled and austenitized and quenched (A&Q) microstructures are summarized. The second section summarizes the main findings of the microstructural characterization and the mechanical testing results from the tempered steels. Based on these conclusions, recommendations for the heat treatment and alloy design of P110 steel to improve sour service performance are provided

6.1 Characterization of As-rolled and A&Q Samples

The observations/conclusions for the EMPA analysis of the as-rolled and A&Q P110 steels are presented. This is followed by a summary of the microstructural analysis of the A&Q steels.

6.1.1 EMPA analysis of microsegregation

The main findings obtained from the EMPA analysis are summarized below:

[1] Microsegregation was observed in the as-rolled 0.52 wt% Cr and 0.77 wt% Cr plates. The maximum segregation ratio for Cr and Mo of the 0.77 wt% Cr steel can reach as high as 1.25 and 1.67, respectively.

[2] The 0.77 wt% Cr plate, with slightly higher nominal C wt%, does not display a higher extent of microsegregation in the as-rolled condition.

[3] Mo exhibited the highest magnitude of microsegregation followed by Mn and Cr. This trend agrees with the values for the equilibrium partition coefficients (due to segregation that occurs during solidification).

[4] The A&Q treatment at 950 °C for 30 min decreased the peak concentrations for both Mo and Cr. The maximum segregation ratio of the 0.77 wt% Cr steel decreased from 1.67 to 1.39 for Mo and from 1.20 to 1.10 for Cr.

6.1.2   Microstructural study of A&Q plates

The main findings based on the characterization of A&Q plates are as follows:

[1] Ti and Mo rich precipitates were observed in both the 0.52 wt% Cr and 0.77 wt% Cr plates after quenching. The variation in nominal C content from 0.255 wt% to 0.278 wt% did not affect the size distribution of the precipitates.

[2] Considerable prior austenite grain (PAG) growth from 11 μm (15 min) to 15 μm (90 min) occurred during austenitization at 950 °C.

[3] A&Q steels from 950 °C for 15 min were selected as the starting materials for tempering studies based on the optimum balance between solutionizing and PAG growth.

[4] The A&Q steel from 950 °C for 15 min contained the finest PAG size (~ 11 μm), less than 0.5 vol% retained austenite, as well as fine (< 20 nm) and dispersed carbides containing Ti and Mo.

6.2   Characterization of Quenched and Tempered Samples

The observations/conclusions for the microstructural analysis of the Q&T P110 steels are presented. This is followed by a summary of the tensile and hardness testing results of the Q&T steels.

6.2.1   Microstructural study of Q&T plates

The major microstructural findings are given in the following:

[1] Fine and dispersed MC particles (< 20 nm), likely formed during the hot rolling process, were observed in the as-quenched samples. Their shapes and size distribution were unaffected by subsequent tempering heat treatments.

[2] The average Mo content in the M constituent of MC carbides increased from 34 wt% (20 at%) to 44 wt% (28 at%) after tempering at 715 °C for 45 min. This increasing trend is consistent with thermodynamic calculations.

103

[3] An increase in both nominal Cr content (from 0.52 wt% to 0.77 wt%) and temperature (from 600 °C to 715 °C) led to an increase in the Cr content of M_3C carbides.

[4] $M_{23}C_6$ carbides were only identified in tempered 0.77 wt% Cr steels, but not in tempered 0.52 wt% Cr steels. The higher Cr content in both ferrite solution and M_3C particles of the 0.77 wt% Cr steel promotes the nucleation of $M_{23}C_6$ carbides.

[5] No prominent difference in the size and volume fraction of M_3C particles between the 0.77 wt% Cr and 0.52 wt% steels was identified. According to ThermoCalc simulations, although a higher nominal C content in the 0.77 wt% Cr steel (0.278 wt% C) would tend to favor M_3C coarsening, its higher nominal Cr content (0.77 wt% Cr) could inhibit M_3C coarsening by reducing C diffusivity.

[6] Coarsening of M_3C was accelerated by increasing tempering temperature, particularly at a temperature higher than 650 °C. After tempering at 600 °C, 650 °C, and 715 °C for 45 min, the average M_3C equivalent diameter (*ED*) value increased from ~54 nm to ~66 nm to ~95 nm.

[7] The M_3C volume fraction in ferrite approached equilibrium values after tempering at 650°C for 45 min. Any increase in tempering temperature or time beyond this condition led to the Ostwald ripening of M_3C, where larger particles grew at the expense of smaller ones.

[8] Significant coarsening in the lath structure was observed during tempering at temperatures above 650 °C. After tempering at 600 °C, 650 °C, and 715 °C for 45 min, the average lath width for the 0.77 wt% Cr steel increased from 329 ± 69 nm to 335 ± 89 nm to 638.7 ± 90 nm.

6.2.2 *Mechanical properties of Q&T plates*

The mechanical testing results and their relationship with underlying carbide morphology are as follows:

[1] The hardness, yield strength (YS), ultimate tensile strength (UTS), and total elongation after tempering for any combination of time and temperature exhibited linear behavior when plotted against the Holloman Jaffe (HJ) parameter.

[2] By increasing the tempering time and temperature, the hardness, UTS, and YS of the quenched steel decreased, while the elongation and ductility increased.

[3] The continuous decrease in hardness and tensile properties is attributed to the combined effects of carbide coarsening, dislocation annihilation, and lath structure coarsening.

[4] During tempering with HJ < 17.4, fine (< 20 nm) MC carbides, as well as rod-shaped M_3C particles with high number densities and volume fractions, pinned the grain boundaries. This effect partially offset the softening caused by the decomposition of martensite.

6.3 Recommendations

Recommendations for the heat treatment and alloy design of P110 casing steel are as follows:

[1] To avoid the potential decrease in toughness from PAG growth during austenitization at 950 °C, the holding time (heating + soaking) should be no more than 15 min.

[2] The 0.52 wt% Cr P110 steel is more economic choice relative to the 0.77 wt% Cr steel, since the tempered carbide morphology (i.e., size, volume fraction, distribution, and type) exhibited no significant difference due to the additional Cr content.

[3] To produce P110 steel that meets the minimum YS requirements (i.e., 758 MPa) from the API 5CT standard, tempering should be conducted at conditions where HJ < 18.4. For standard tempering times of 15 min and 45 min, HJ < 18.4 corresponds to temperatures lower than 700 °C and 675 °C, respectively.

[4] Unless the tempering time (i.e., the HJ parameter) is very low, the tempering temperature should not exceed 650 °C in order to acquire sufficient strength (i.e., hardness, UTS, and YS) by avoiding significant carbide coarsening, lath structure coarsening, and dislocation annihilation,

[5] Tempering at high temperatures for a short time, such as 715 °C for 15 min (HJ = 18.7), can produce an optimal microstructure with relatively fine (<61 nm) and densely distributed (57/μm^2) carbides. The HJ parameter must be strictly controlled to avoid excessive reduction in strength.

[6] In terms of hydrogen embrittlement resistance (HE) resistance, the optimum carbide morphology can be obtained by tempering at 650 °C for 45 min, where uniformly distributed fine particles (60-65 nm) with a high number density (51/μm^2) and volume fraction (0.11) are produced.

Reference

1. Urband B, Bernard F, Morey S, et al. Latest enhancements in hiqh strength sour service tubulars. *SPE/IADC Drill Conf Proc*. 2009;2:1159-1170.
2. Luo M, Liu M, Wang XT, et al. Effect of tempering temperature at high temperature zone on sulfide stress cracking behavior for casing steel. *Eng Fail Anal*. 2019;105(June):227-236. doi:10.1016/j.engfailanal.2019.06.095
3. Jenkins CF, Mickalonis JI, Wilson DA, et al. DEVELOPMENT OF 125KSI GRADE HSLA STEEL OCTG FOR MILDLY SOUR ENVIRONMENTS. *Corrosion*. 2005;(05604):1-16. doi:http://dx.doi.org/10.1016/j.compeleceng.2015.03.017
4. Ju Y, Goodall A, Davis C, Strangwood M. Characterisation of precipitation and coarsening of carbides during tempering in a low alloyed quenched and tempered steel. *Mater Sci Forum*. 2018;941 MSF:33-38. doi:10.4028/www.scientific.net/MSF.941.33
5. Wang XT, Liu M, Zhou GY, et al. Effects of chromium and tungsten on sulfide stress cracking in high strength low alloy 125 ksi grade casing steel. *Corros Sci*. 2019;160(August):108163. doi:10.1016/j.corsci.2019.108163
6. Zhang ZH, Liu M, Liu YH, et al. A systematical analysis with respect to multiple hydrogen traps influencing sulfide stress cracking behavior of API-5CT-C110 casing steel. *Mater Sci Eng A*. 2018;721(December 2017):81-88. doi:10.1016/j.msea.2018.02.070
7. Publication A, Specification API. API Specification 5CT. *API Specif 5CT*. 2019;(June 2018).
8. Perez TE. Corrosion in the Oil and Gas Industry: An Increasing Challenge for Materials. In: *Energy Materials 2014*. Cham: Springer International Publishing; 2016:565-574.
9. Kane RD, Cayard MS. Roles of H2S in the Behavior of Engineering Alloys: A Review of Literature and Experience. *Corros NACE*. 1998;(Paper No.274):1-28.
10. Engineering P. Chemical and Petroleum Engineering, 'Col. 32, No. 6, 1996. 1996;(6):59-62.
11. Cracking SS. Hydrogen-induced cracking and sulfide stress cracking. 1972;448:183-194.
12. Tems RD. *4 - Downhole Corrosion*. Elsevier Ltd; 2017. doi:10.1016/B978-0-08-101105-8.00004-8
13. Pfeil LB, Carpenter HCH. The effect of occluded hydrogen on the tensile strength of iron. *Proc R Soc London Ser A, Contain Pap a Math Phys Character*. 1926;112(760):182-195. doi:10.1098/rspa.1926.0103
14. Troiano AR. The Role of Hydrogen and Other Interstitials in the Mechanical Behavior of Metals. *Metallogr Microstruct Anal*. 2016;5(6):557-569. doi:10.1007/s13632-016-0319-4
15. Oriani RA. A mechanistic theory of hydrogen embrittlement of steels. *Berichte der Bunsengesellschaft für Phys Chemie*. 1972;76(8):848-857. doi:10.1002/bbpc.19720760864
16. Oriani RA. Whitney Award Lecture—1987: Hydrogen—The Versatile Embrittler. *CORROSION*. 1987;43(7):390-397. doi:10.5006/1.3583875
17. Gerberich WW, Marsh PG, Hoehn JW. Hydrogen Induced Cracking Mechanisms — Are There Critical Experiments? *Hydrog Eff Mater*. September 1994:539-554. doi:doi:10.1002/9781118803363.ch47
18. Wan L, Mei Q, Geng WT, et al. Hydrogen embrittlement controlled by reaction of dislocation with grain boundary in alpha-iron. *Int J Plast*. 2019;112:206-219.

doi:10.1016/j.ijplas.2018.08.013

19. Lynch SP. Progress Towards Understanding Mechanisms Of Hydrogen Embrittlement And Stress Corrosion Cracking. *Corros 2007*. 2007:55. https://doi.org/.

20. Lynch SP. 2 - Hydrogen embrittlement (HE) phenomena and mechanisms. In: Raja VS, Shoji TBT-SCC, eds. *Woodhead Publishing Series in Metals and Surface Engineering*. Woodhead Publishing; 2011:90-130. doi:https://doi.org/10.1533/9780857093769.1.90

21. Lynch SP. Progress Towards Understanding Mechanisms Of Hydrogen Embrittlement And Stress Corrosion Cracking. *Corros 2007*. 2007:55.

22. Lynch SP. 2 - Hydrogen embrittlement (HE) phenomena and mechanisms. In: Raja VS, Shoji TBT-SCC, eds. *Woodhead Publishing Series in Metals and Surface Engineering*. Woodhead Publishing; 2011:90-130. doi:https://doi.org/10.1533/9780857093769.1.90

23. Dai T, Thodla R, Kovacs III W, Tummala K, Lippold J. Effect of Postweld Heat Treatment on the Sulfide Stress Cracking of Dissimilar Welds of Nickel Base Alloy 625 on Steels. *Corrosion*. 2019;75(6):641-656. doi:10.5006/3081

24. King RA. 11 - Sulfide stress cracking. In: El-Sherik AMBT-T in O and GCR and T, ed. *Woodhead Publishing Series in Energy*. Boston: Woodhead Publishing; 2017:271-294. doi:https://doi.org/10.1016/B978-0-08-101105-8.00011-5

25. King RA. 11 - Sulfide stress cracking. In: El-Sherik AMBT-T in O and GCR and T, ed. *Woodhead Publishing Series in Energy*. Boston: Woodhead Publishing; 2017:271-294. doi:https://doi.org/10.1016/B978-0-08-101105-8.00011-5

26. Pollack HW. *Materials Science and Metallurgy*. Englewood Cliffs, N.J.: Prentice-Hall; 1988.

27. Savran VI. *Austenite Formation in C-Mn Steel*.; 2009.

28. Capdevila C, Caballero FG, García de Andrés C. Modeling of kinetics of isothermal idiomorphic ferrite formation in a medium-carbon vanadium-titanium microalloyed steel. *Metall Mater Trans A*. 2001;32(7):1591-1597. doi:10.1007/s11661-001-0137-3

29. Mehl RF, Hagel WC. The austenite: Pearlite reaction. *Prog Met Phys*. 1956;6:74-134. doi:https://doi.org/10.1016/0502-8205(56)90005-3

30. Dykhuizen RC, Robino C V, Knorovsky GA. A method for extracting phase change kinetics from dilatation for multistep transformations: Austenitization of a low carbon steel. *Metall Mater Trans B*. 1999;30(1):107-117. doi:10.1007/s11663-999-0011-z

31. Matsuo S, Ando T, Grant N. Grain refinement and stabilization in spray-formed AISI 1020 steel. *Mater Sci Eng A-structural Mater Prop Microstruct Process - MATER SCI ENG A-STRUCT MATER*. 2000;288:34-41. doi:10.1016/S0921-5093(00)00881-9

32. Hong S, Lim S, Hong H, Lee K, Shin D, Lee K-S. Effects of Nb on strain induced ferrite transformation in C–Mn steel. *Mater Sci Eng A*. 2003;355:241-248. doi:10.1016/S0921-5093(03)00071-6

33. Lee SJ, Lee YK. Prediction of austenite grain growth during austenitization of low alloy steels. *Materials Des*. 2008;29(9):1840-1844. doi:10.1016/j.matdes.2008.03.009

34. Lee S. Predictive Model for Austenite Grain Growth during Reheating of Alloy Steels. *ISIJ Int*. 2013;53(10):1902-1904.

35. Xu D, Ji C, Zhao H, Ju D, Zhu M. A new study on the growth behavior of austenite grains during heating processes. *Scientific Reports*. 2017;7(1):1-13. doi:10.1038/s41598-017-04371-8

36. Petkov P. AUSTENITE DECOMPOSITION OF L O W C A R B O N H I G H Library Authorization. 2004;(March).

37. Giumelli AK, Militzer M, Hawbolt EB. Analysis of the Austenite Grain Size Distribution in Plain Carbon Steels. *ISIJ Int*. 1999;39(3):271-280. doi:10.2355/isijinternational.39.271

38. Maki T. 2 - Morphology and substructure of martensite in steels. In: Pereloma E, Edmonds DVBT-PT in S, eds. *Woodhead Publishing Series in Metals and Surface Engineering*. Vol 2. Woodhead Publishing; 2012:34-58. doi:https://doi.org/10.1533/9780857096111.1.34

39. Maki T. 2 - Morphology and substructure of martensite in steels. In: Pereloma E, Edmonds DVBT-PT in S, eds. *Woodhead Publishing Series in Metals and Surface Engineering*. Vol 2. Woodhead Publishing; 2012:34-58. doi:https://doi.org/10.1533/9780857096111.1.34

40. Stoicanescu M, Ene E, Zara A, Giacomelli I, Crisan A. The Heat Treatment Influence of 1.3343 High Speed Steel on Content of Residual Austenite. *Procedia Technol*. 2016;22:161-166. doi:https://doi.org/10.1016/j.protcy.2016.01.039

41. Speich GR, Leslie WC. Tempering of steel. *Metall Trans*. 1972;3(May):1043-1054.

42. Ojha S, Mishra NS, Jha BK. Effect of cooling rate on the microstructure and mechanical properties of a C-Mn-Cr-B steel. *Bull Mater Sci*. 2015;38(2):531-536. doi:10.1007/s12034-015-0862-7

43. Pashangeh S, Zarchi HRK, Banadkouki SSG, Somani MC. Detection and estimation of retained austenite in a high strength Si-bearing bainite-martensite-retained austenite micro-composite steel after quenching and bainitic holding (Q&B). *Metals*. 2019;9(5). doi:10.3390/met9050492

44. Krauss G. *STEELS - Processing, Structure, and Performance*.; 2005.

45. Berns H, Theisen W. *Ferrous Materials: Steel and Cast Iron*.; 2008. doi:10.1007/978-3-540-71848-2

46. Krauss G. 5 - Tempering of martensite in carbon steels. In: Pereloma E, Edmonds DVBT-PT in S, eds. *Woodhead Publishing Series in Metals and Surface Engineering*. Vol 2. Woodhead Publishing; 2012:126-150. doi:https://doi.org/10.1533/9780857096111.1.126

47. Krauss G. 5 - Tempering of martensite in carbon steels. In: Pereloma E, Edmonds DVBT-PT in S, eds. *Woodhead Publishing Series in Metals and Surface Engineering*. Vol 2. Woodhead Publishing; 2012:126-150. doi:https://doi.org/10.1533/9780857096111.1.126

48. Ji C, Yao J, Zhu M. Effect of Ostwald ripening of carbide particles on mechanical properties of SCM435 steel during subcritical annealing. *J Iron Steel Res Int*. 2018;25(7):724-731. doi:10.1007/s42243-018-0105-4

49. Furuhara T, Kobayashi K, Maki T. Control of Cementite Precipitation in Lath Martensite by Rapid Heating and Tempering. *ISIJ Int*. 2004;44(11):1937-1944. doi:10.2355/isijinternational.44.1937

50. Honeycombe RWK. *Structure and Strength of Alloy Steels*. United States: Climax Molybdenum Co Ltd; 1975. http://inis.iaea.org/search/search.aspx?orig_q=RN:06195633.

51. BAIN EC, PAXTON HW. *Alloying Elements in Steel. Second Edition [of the Work by E.C. Bain]. By E.C. Bain ... and Harold W. Paxton*. Metals Park; 1961. https://books.google.ca/books?id=BSANMwEACAAJ.

52. Schick HL. *Thermodynamics of Certain Refractory Compounds : H.L.Schick, Principaal Contributor and Editor in Collaboration with the Contributors*. N.Y. : Academic Press; 1966.

53. Canale LCF, Yao X, Gu J, Totten GE. A historical overview of steel tempering parameters. *Int J Microstruct Mater Prop*. 2008;3(4-5):474-525.

doi:10.1504/IJMMP.2008.022033

54. Revilla C, López B, Rodriguez-Ibabe JM. Carbide size refinement by controlling the heating rate during induction tempering in a low alloy steel. *Materials Des*. 2014;62:296-304. doi:10.1016/j.matdes.2014.05.053

55. Euser VK, Clarke AJ, Speer JG. Rapid Tempering: Opportunities and Challenges. *J Mater Eng Perform*. 2020;29(7):4155-4161. doi:10.1007/s11665-020-04946-z

56. Dépinoy S, Toffolon-Masclet C, Urvoy S, et al. Carbide Precipitation in 2.25 Cr-1 Mo Bainitic Steel: Effect of Heating and Isothermal Tempering Conditions. *Metall Mater Trans A Phys Metall Mater Sci*. 2017;48(5):2164-2178. doi:10.1007/s11661-017-4045-6

57. Viswanathan R, Nutting J [eds. . EPRI (USA)]. *Advanced Heat Resistant Steel for Power Generation*. United Kingdom: IOM Communications Ltd., London (United Kingdom); 1999.

58. Eremenko VN, Velikanova TY. Phase equilibria in the Mo-TiC-Ti region of the ternary system Mo-Ti-C. Character of solidification of alloys and projection of the solidus surface Part I. *Sov Powder Metall Met Ceram*. 1969;8(11):931-936. doi:10.1007/BF00778406

59. Okazaki Y. Effects of Heat Treatment and Hot Forging on Microstructure and Mechanical Properties of Co-Cr-Mo Alloy for Surgical Implants. *Mater Trans*. 2008;49(4):817-823. doi:10.2320/matertrans.MRA2007274

60. Villars P, Cenzual K, eds. (Cr,Fe)7C3 (Cr3.5Fe3.5C3 rt) Crystal Structure: Datasheet from "PAULING FILE Multinaries Edition – 2012" in SpringerMaterials (https://materials.springer.com/isp/crystallographic/docs/sd_1413617). https://materials.springer.com/isp/crystallographic/docs/sd_1413617.

61. TmaKi K. Precipitation of Carbides during Tempering of Cr-Mo steels. :antibiotic resistance among disease causing bacter.

62. Janovec J. Effect of tempering on development of carbide particles in 2.7Cr-O.6Mo-O.3V steel. *J Mater Sci*.1992;27.

63. Robson JD. Modelling the overlap of nucleation, growth and coarsening during precipitation. *Acta Mater*. 2004;52(15):4669-4676. doi:10.1016/j.actamat.2004.06.024

64. Hou Z, Babu RP, Hedström P, Odqvist J. Early stages of cementite precipitation during tempering of 1C–1Cr martensitic steel. *J Mater Sci*. 2019;54(12):9222-9234. doi:10.1007/s10853-019-03530-8

65. Nazemi F, Hamel-Akré J, Bocher P. Modeling of cementite coarsening during tempering of low-alloyed-medium carbon steel. *Journal Mater Sci*. 2018;53(8):6198-6218. doi:10.1007/s10853-017-1943-3

66. Hou Z, Babu RP, Hedström P, Odqvist J. On coarsening of cementite during tempering of martensitic steels. *Mater Sci Technol (United Kingdom)*. 2020;36(7):887-893. doi:10.1080/02670836.2020.1740380

67. Lee HM, Allen SM. Coarsening resistance of M2C carbides in secondary hardening steels: Part III. Comparison of theory and experiment. *Metall Trans A*. 1991;22(12):2877-2888. doi:10.1007/BF02650249

68. Ning A, Yue S, Gao R, Li L, Guo H. Influence of tempering time on the behavior of large carbides' coarsening in aisi h13 steel. *Metals (Basel)*. 2019;9(12). doi:10.3390/met9121283

69. Wu YX, Sun WW, Gao X, Styles MJ, Arlazarov A, Hutchinson CR. The effect of alloying elements on cementite coarsening during martensite tempering. *Acta Mater*. 2020;183:418-437. doi:10.1016/j.actamat.2019.11.040

70.   Miyamoto G, Oh JC, Hono K, Furuhara T, Maki T. Effect of partitioning of Mn and Si on the growth kinetics of cementite in tempered Fe-0.6 mass% C martensite. *Acta Mater*. 2007;55(15):5027-5038. doi:10.1016/j.actamat.2007.05.023

71.   Ghosh S. Rate-controlling parameters in the coarsening kinetics of cementite in Fe-0.6C steels during tempering. *Scripta Mater*. 2010;63(3):273-276. doi:10.1016/j.scriptamat.2010.04.002

72.   Babu SS, Hono K, Sakurai T. Atom probe field ion microscopy study of the partitioning of substitutional elements during tempering of a low-alloy steel martensite. *Metall Mater Trans A*. 1994;25(3):499-508. doi:10.1007/BF02651591

73.   Liu J, Liu W, Hao Z, et al. Effects of Silicon Content and Tempering Temperature on the Microstructural Evolution and Mechanical Properties of HT-9 Steels. *Mater (Basel, Switzerland)*. 2020;13(4):972. doi:10.3390/ma13040972

74.   Asahi H, Sogo Y, Ueno M, Higashiyama H. Metallurgical factors controlling SSC resistance of high-strength, low-alloy steels. *Corrosion*. 1989;45(6):519-527. doi:10.5006/1.3582053

75.   Watkins Houston, TX (United States)] M [Exxon PRC, Ayer Inc., Woodbridge, CT (United States)] R [STEM. *Microstructure -- the Critical Variable Controlling the SSC Resistance of Low-Alloy Steels*. United States: NACE International, Houston, TX (United States); 1995. https://www.osti.gov/biblio/99520.

76.   Carneiro RA, Ratnapuli RC, de Freitas Cunha Lins V. The influence of chemical composition and microstructure of API linepipe steels on hydrogen induced cracking and sulfide stress corrosion cracking. *Mater Sci Eng A*. 2003;357(1):104-110. doi:https://doi.org/10.1016/S0921-5093(03)00217-X

77.   Pous-Romero H, Bhadeshia H. Coalesced martensite in pressure vessel steels. *J Press Vessel Technol Trans ASME*. 2014;136(3). doi:10.1115/1.4026192

78.   Asahi H, Ueno M. Effect of Austenite Grain Size on Sulfide Stress Cracking Resistance of Low Alloy Martensitic Steels. *ISIJ Int*. 1992;32(9):1021-1026. doi:10.2355/isijinternational.32.1021

79.   Depover T, Verbeken K. The effect of TiC on the hydrogen induced ductility loss and trapping behavior of Fe-C-Ti alloys. *Corros Sci*. 2016;112:308-326. doi:https://doi.org/10.1016/j.corsci.2016.07.013

80.   Nagao A, Martin ML, Dadfarnia M, Sofronis P, Robertson IM. The effect of nanosized (Ti,Mo)C precipitates on hydrogen embrittlement of tempered lath martensitic steel. *Acta Mater*. 2014;74:244-254. doi:10.1016/j.actamat.2014.04.051

81.   Hutchinson B, Hagström J, Karlsson O, et al. Microstructures and hardness of as-quenched martensites (0.1–0.5%C). *Acta Mater*. 2011;59(14):5845-5858. doi:https://doi.org/10.1016/j.actamat.2011.05.061

82.   Huang W, Cao F, Srinivasan R, et al. SSC resistance and cracking behavior of 125ksi grade low alloy OCTG in sour environments. *NACE - Int Corros Conf Ser*. 2013;(2293):1-15.

83.   INTERNATIONAL A. Standard Test Methods for Determining Average Grain Size. *Astm E112-10*. 2010:1-27. doi:10.1520/E0112-13.1.4

84.   Golden A. the Effect of Heat Treatment on the Through Thickness Properties of Vanadium Microalloyed Forging Steels. *Master Sci Thesis*. file:///C:/Users/User/Downloads/fvm939e.pdf.

85.   ASTM. A370: Standard Test Methods and Definitions for Mechanical Testing of Steel

Products. *ASTM Int*. 2014:1-50.

86. Turkeli A. *Effect of Carbon Content on the Segregation of Manganese in Steel*.; 1993.

87. Ilie S, Preßlinger H, Reisinger P, Mayr M, Etzelsdorfer K. Results of Research into the Segregation Behaviour of Manganese, Silicon and Chromium in Continuous Casting. *steel Res Int*. 2007;78(4):327-332. doi:https://doi.org/10.1002/srin.200705899

88. Guo J, Wen G. Influence of Alloy Elements on Cracking in the Steel. 2019.

89. Zhang D. Characterisation and modelling of segregation in continuously cast steel slab. In: ; 2015.

90. Ghosh A. Segregation in cast products. *Sadhana - Acad Proc Eng Sci*. 2001;26(1-2):5-24. doi:10.1007/BF02728476

91. Alberry PJ, Haworth CW. Interdiffusion of Cr, Mo, and W in Iron. *Met Sci*. 1974;8(1):407-412. doi:10.1179/msc.1974.8.1.407

92. Yuehui H, Qiuhua R, Yuua T. Investigation on the morphology of martensite in carbon steels. *J Cent South Univ Technol (English Ed*. 1996;3(2):133-134. doi:10.1007/bf02652191

93. Prawoto Y, Jasmawati N, Sumeru K. Effect of Prior Austenite Grain Size on the Morphology and Mechanical Properties of Martensite in Medium Carbon Steel. *J Mater Sci Technol*. 2012;28(5):461-466. doi:10.1016/S1005-0302(12)60083-8

94. Schwenk M. Transformation Hardening in Steel BT - Encyclopedia of Thermal Stresses. In: Hetnarski RB, ed. Dordrecht: Springer Netherlands; 2014:6140-6153. doi:10.1007/978-94-007-2739-7_464

95. Jatczak CF. Retained austenite and its measurement by X-ray diffraction. *SAE Tech Pap*. 1980;89:1657-1676. doi:10.4271/800426

96. Raja VS, Shoji TBT-SCC, eds. Front matter. In: *Woodhead Publishing Series in Metals and Surface Engineering*. Woodhead Publishing; 2011:i-iii. doi:https://doi.org/10.1533/9780857093769.frontmatter

97. Sun Y, Wang Q, Gu S, He Z, Wang Q, Zhang F. Sulfide stress crac king behavior of a martensitic steel controlled by tempering temperature. *Materials*. 2018;11(3). doi:10.3390/ma11030412

98. Taneike M, Sawada K, Abe F. Effect of Carbon Concentration on Precipitation Behavior of M 23 C 6 Carbides and MX Carbonitrides in Martensitic 9Cr Steel during Heat Treatment. 2004;35(April).

99. Jung J-G, Park J-S, Kim J, Lee Y-K. Carbide precipitation kinetics in austenite of a Nb–Ti–V microalloyed steel. *Mater Sci Eng A*. 2011;528(16):5529-5535. doi:https://doi.org/10.1016/j.msea.2011.03.086

100. Duan X, Cai Q, Wu H. Ti-Mo Ferrite Matrix Micro-alloy Steel with Nnaometer-sized Precipitates. 2011:251-256.

101. Yuan S, Wang C, Liang G, Liu Y. Precipitation Behavior in a Mo - contained Micro - alloyed Steel. *J Tangshan Coll*. 2008;21.

102. Funakawa Y, Seto K. Coarsening Behavior of Nanometer-Sized Carbides in Hot-Rolled High Strength Sheet Steel. *Mater Sci Forum - MATER SCI FORUM*. 2007;539:4813-4818. doi:10.4028/www.scientific.net/MSF.539-543.4813

103. Wei F-G, Hara T, Tsuchida T, Tsuzaki K. Hydrogen Trapping in Quenched and Tempered 0.42C-0.30Ti Steel Containing Bimodally Dispersed TiC Particles. *ISIJ Int*. 2003;43(4):539-547. doi:10.2355/isijinternational.43.539

104. Wei FG, Hara T, Tsuzaki K. Precise determination of the activation energy for desorption

of hydrogen in two Ti-added steels by a single thermal-desorption spectrum. *Metall Mater Trans B*. 2004;35(3):587-597. doi:10.1007/s11663-004-0057-x

105.   Clarke AJ, Miller MK, Field RD, et al. Atomic and nanoscale chemical and structural changes in quenched and tempered 4340 steel. *Acta Mater*. 2014;77:17-27. doi:10.1016/j.actamat.2014.05.032

106.   Wang Q, Sun Y, Gu S, He Z, Wang Q, Zhang F. Effect of quenching temperature on sulfide stress cracking behavior of martensitic steel. *Materials Sci Eng A*. 2018;724(March):131-141. doi:10.1016/j.msea.2018.03.063

107.   Zhu C, Xiong XY, Cerezo A, Hardwicke R, Krauss G, Smith GDW. Three-dimensional atom probe characterization of alloy element partitioning in cementite during tempering of alloy steel. *Ultramicroscopy*. 2007;107(9):808-812. doi:10.1016/j.ultramic.2007.02.033

108.   Kozeschnik E, Bhadeshia HKDH. Influence of silicon on cementite precipitation in steels. *Mater Sci Technol*. 2008;24(3):343-347. doi:10.1179/174328408X275973

109.   Xie ST, Liu ZY, Wang Z, Wang GD. Microstructure and mechanical properties of a Ti-microalloyed low-carbon stainless steel treated by quenching-partitioning-tempering process. *Mater Charact*. 2016;116:55-64. doi:10.1016/j.matchar.2016.03.025

110.   Kayser FX, Litwinchuk A, Stowe GL. The densities of high-purity iron-carbon alloys in the spheroidized condition. *Metall Trans A*. 1975;6(1):55-58. doi:10.1007/BF02673670

111.   Poorhaydari K, Ivey DG. Precipitate volume fraction estimation in high strength micro alloyed steels. *Can Metall Q*. 2009;48(2):115-122. doi:10.1179/cmq.2009.48.2.115

Appendix A

Chemical Compositions of P110 Steels

Table A.1. Chemistries and heat numbers for 0.52 Cr and 0.77 Cr plates, provided by EVRAZ NA Regina.

Materials	0.52 Cr Heat #: 531789	0.77 Cr Heat #: 412429
C	0.255	0.278
Mn	0.46	0.46
Cr	0.52	0.77
Mo	0.188	0.19
Ti	0.03	0.027
B	0.0022	0.026
N	0.0041	0.0049
S*	0.0006	0.0003
P*	0.006	0.01
Cu* +Ni* +Si +Ca	0.71	0.70

Appendix B

Characterization of Industrial Quenched Pipes

Figure B.1. (a) and (b) shows the OM micrographs of industrial quenched 0.52 Cr and 0.77 Cr plates. It can be noted that both two pipes comprised of uniform lath martensite morphology.
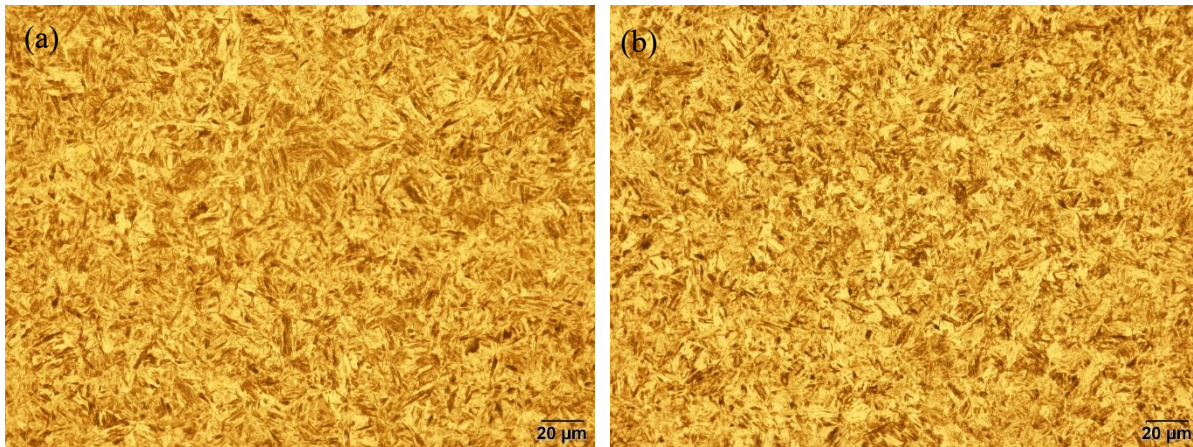

Figure B.1. Optical Micrographs of (a) 0.52 Cr and (b) 0.77 Cr industrial quenched plates at ¼ thickness in the RD-ND plane.

Figure B.2. and B.3. show SEM observations of the industrial quenched pipes. Some spherical and needle shape carbides were found. These carbides were more randomly orientation within grains, indicating that those structures are likely to be tempered martensite. According to Thermo-calc simulation on 0.52 Cr P110, cementite will dissolve at approximately 740°C. The martensite start temperature, M_s, is high for low/med carbon steel. The existence of this relatively large size of carbides in industrial quenched pipes indicated that re-precipiations (self-tempering) might occur during industrial quenching.
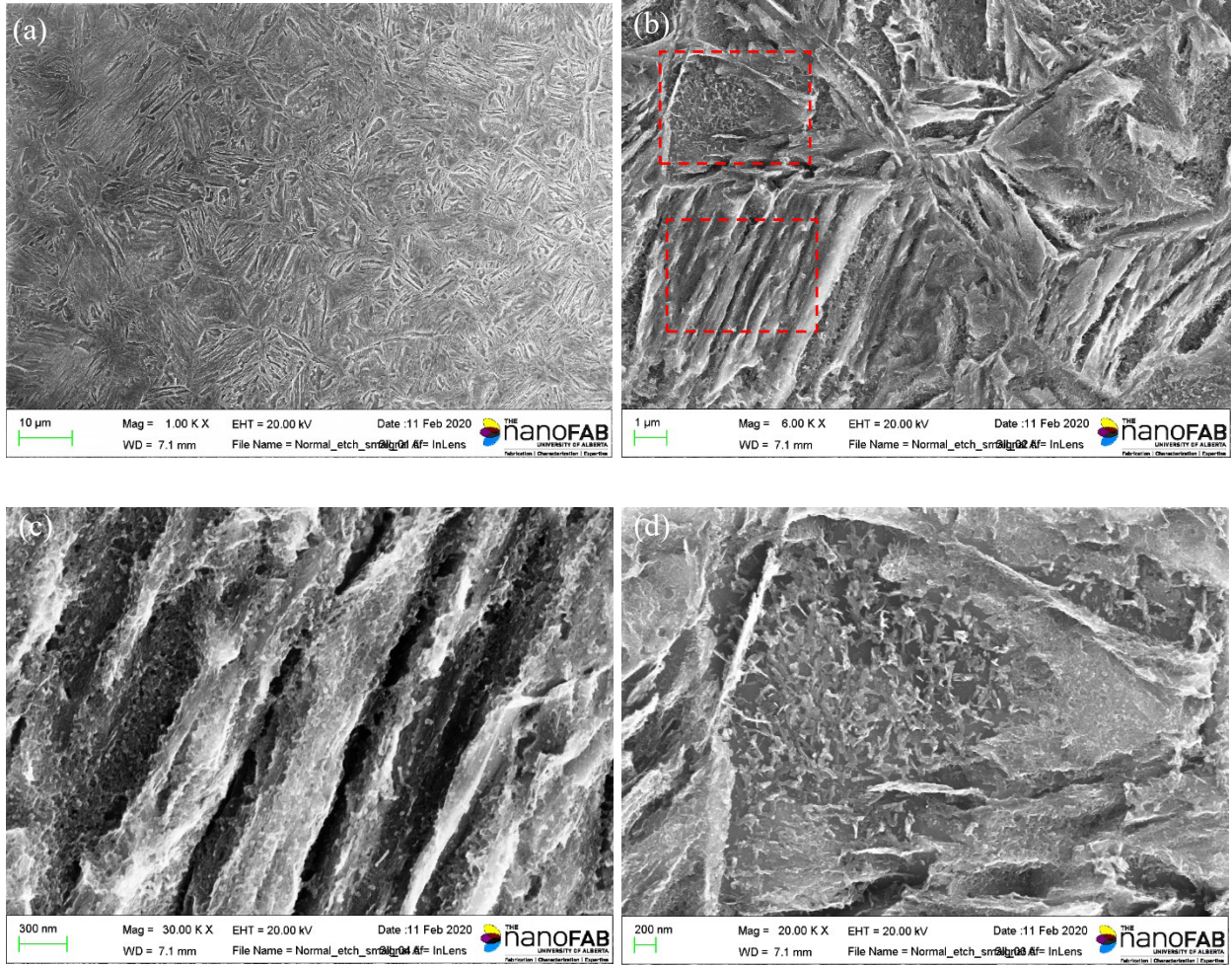
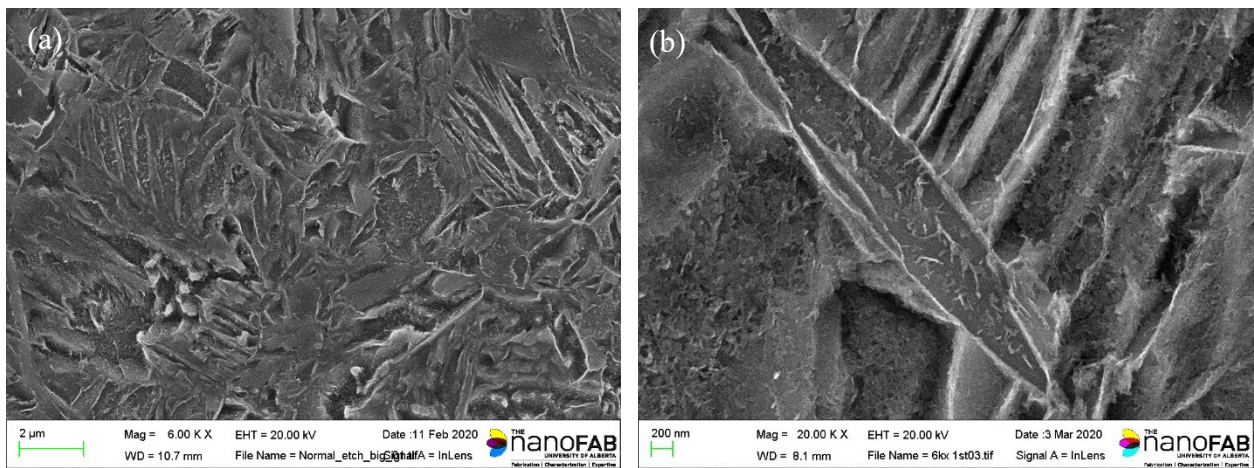**Figure B.2.** SEM micrographs of as-quenched 0.52 Cr pipes.

Figure B.3. SEM micrographs of as-quenched 0.77 Cr pipes.

The peaks for the ferritic phase (martensite) and retained austenite were identified by XRD pattern, as shown in Figure B.4. The low micro-hardness values in quenched pipes can be attributed to the soft retained austenite structure, see Figure B.5.
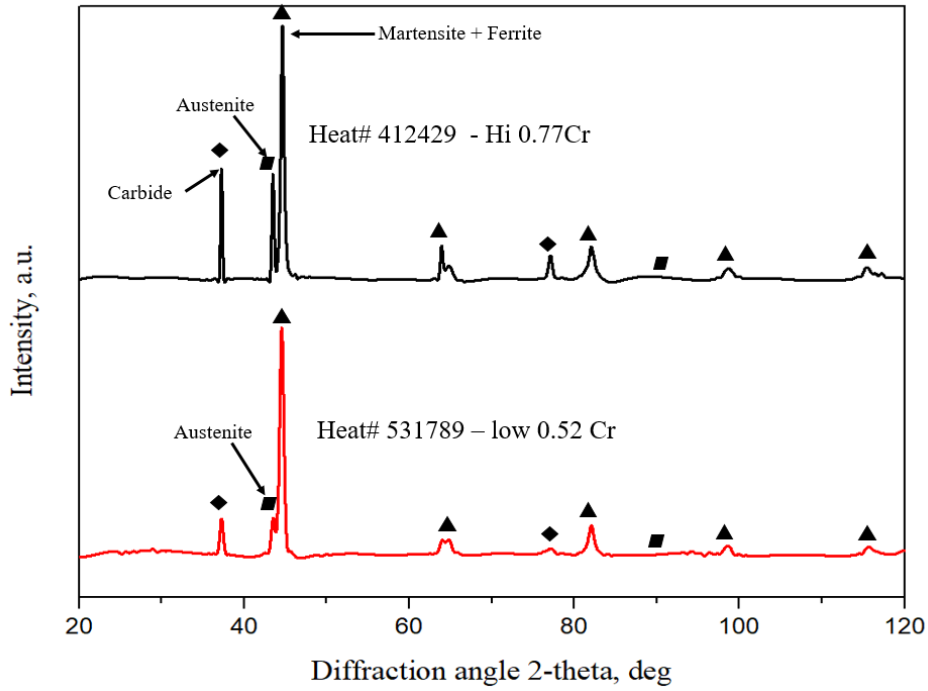

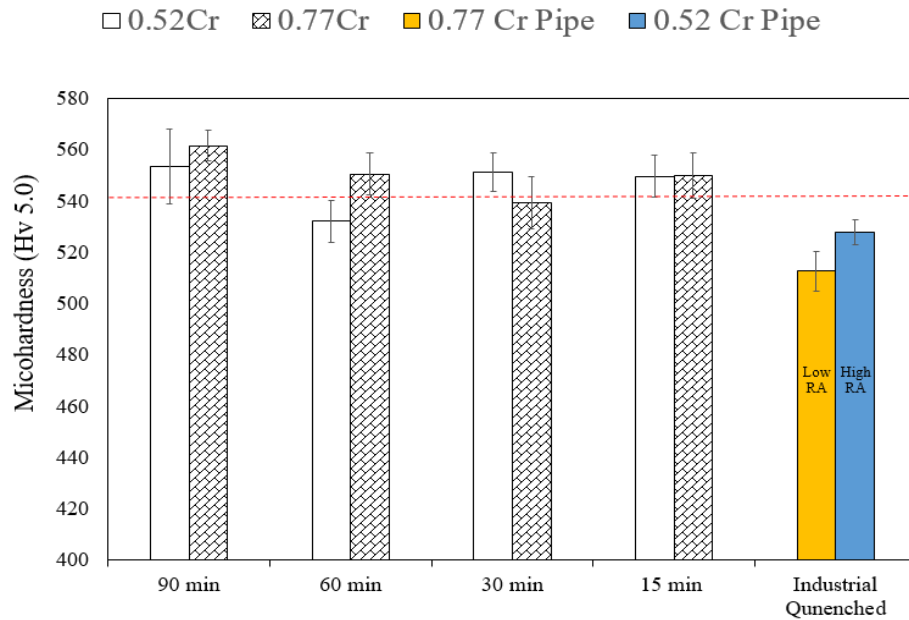**Figure B.4.** XRD patterns of quenched P110 pipes.

Figure B.5. Micro-hardness of A&Q plates and industrial quenched pipes as a function of austenitizing time.

Both the average prior austenite grain size of the industrial quenched pipes and lab quenched plates are displayed in Figure B.6. The industrial quenched pipes have relatively small PAG size comparing to laboratory A&Q plates.
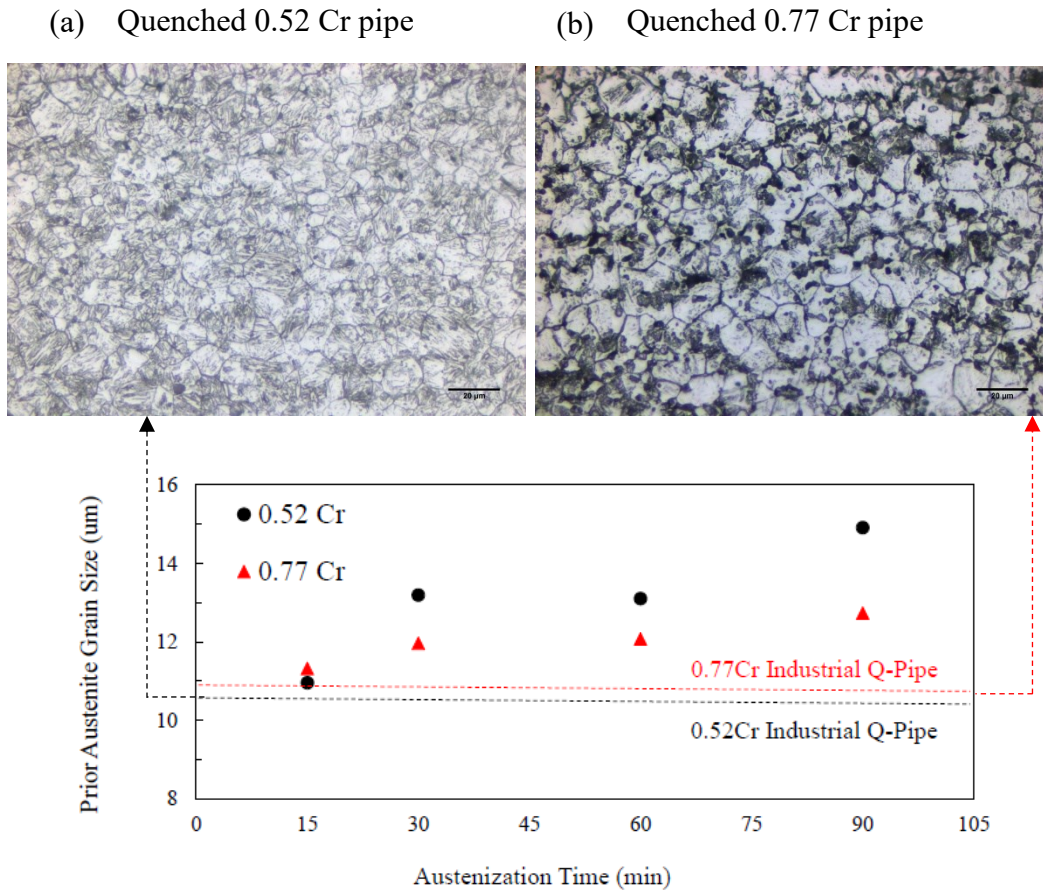
(a)   Quenched 0.52 Cr pipe   (b)   Quenched 0.77 Cr pipe

Figure B.6. Optical images for (a) quenched 0.52 wt% Cr pipes and (b) quenched 0.77 wt% Cr pipes. (c) Prior austenite grain size of both quenched pipes and plates.

Appendix C

Supplementary Characterization on A&Q Plates

C.1.   SEM Characterization of A&Q Pipes

The martensite structures of 0.52 Cr and 0.77 Cr plates after 950 °C-15 min and 950 °C-30 min are shown in Figure C.1. It can be seen that there is no relationship between austenitization time and as-quenched martensite morphology.
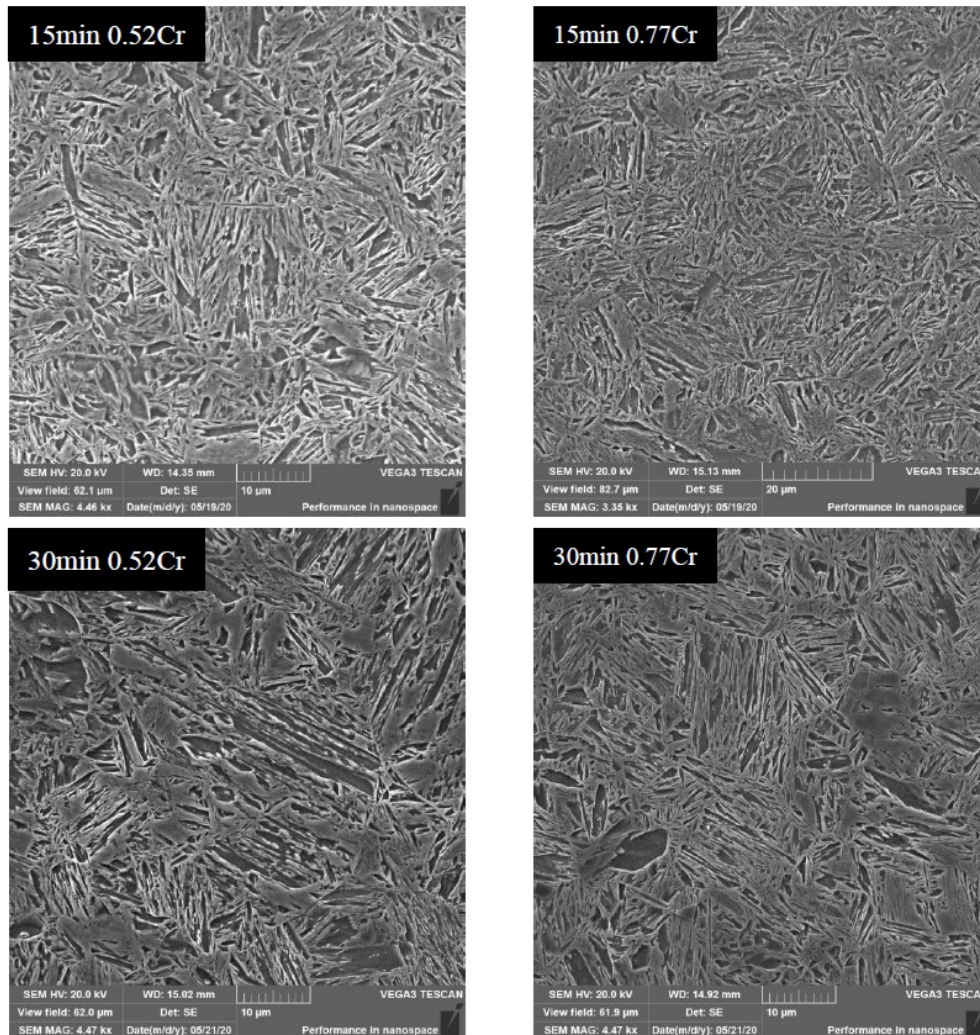

Figure C.1. SEM images of A&Q plates.

C.2.   Partition Coefficient Calculation

An example of partition coefficient calculation for Mo element in as quenched 0.52 Cr plate is shown in this section.

Step 1: An EMPA point scan across the ¼ thickness area was made, see Figure A.2.

Step 2: The Mo concentration data as a function of travel distance is plotted, see Figure A.3.

Figure C.2. EMPA Mo point scan location for quenched 0.52 Cr plate.
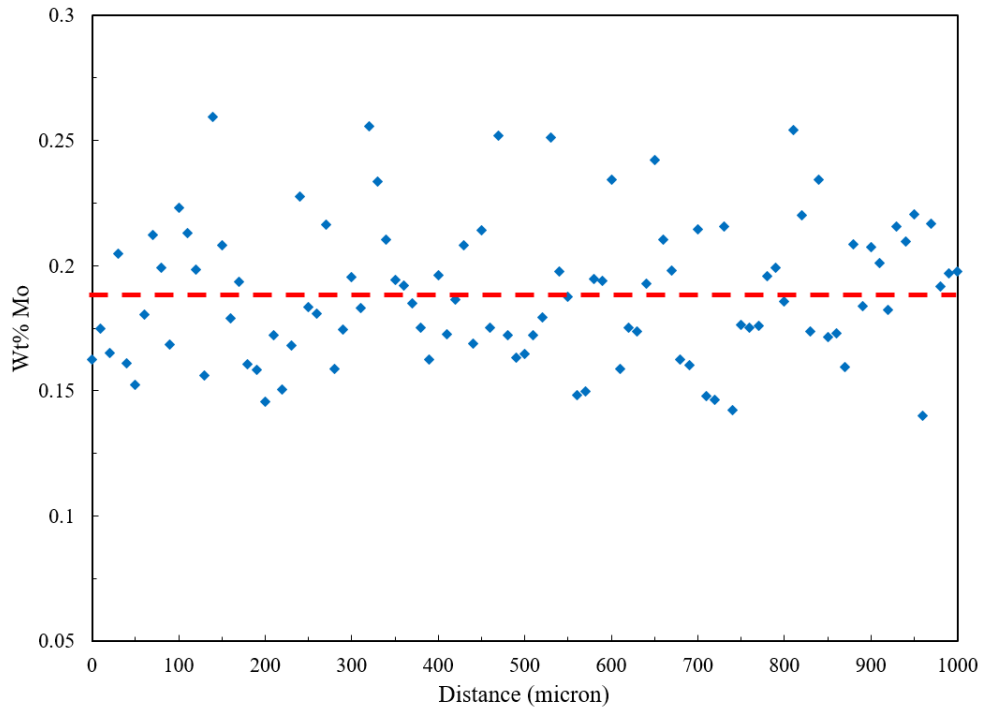

Figure C.3. EMPA Mo points scan for quenched 0.52 Cr plate.

Step 3. The obtained concentration data was sorted into an ascending order. The x-axis was changed from distance to particle number counts, see Figure A.4 (a).

Step 4. Convert x-axis (particle numbers) into normalized fraction, see Figure A.4 (a). The normalized fraction was regarded as fraction soild (f_s). Each f_s has a corresponding composition value.
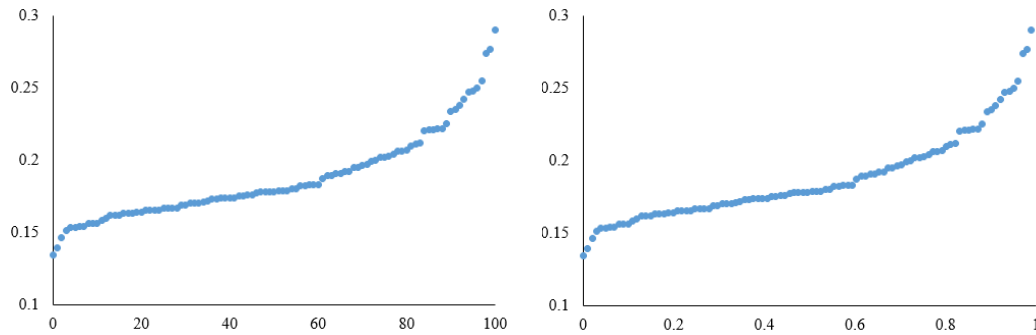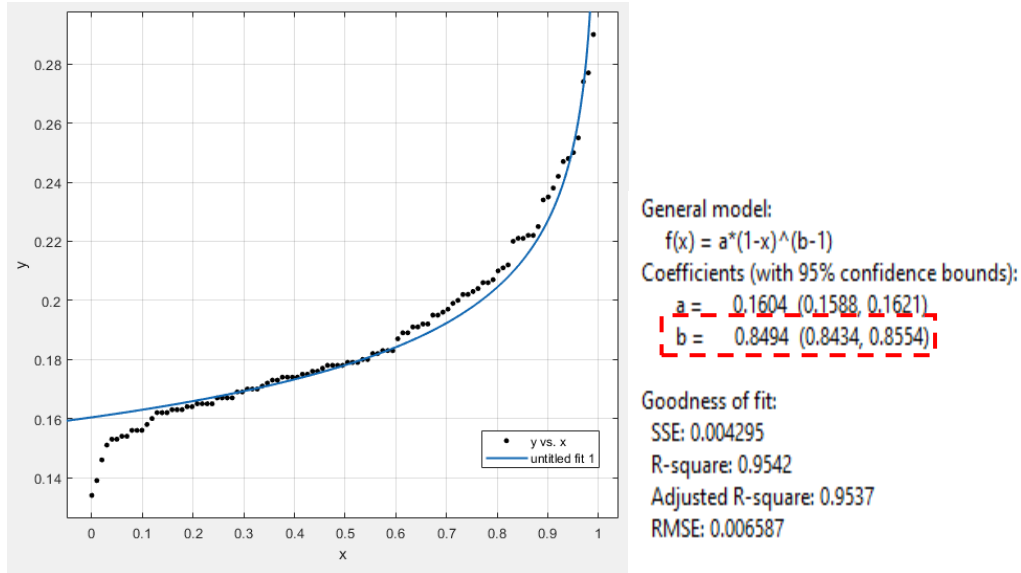

Figure C.4. EMPA measured Mo concentration versus (a) particle number counts, (b) normalized fraction (f_s).

Step 5. The data was then input into Matlab to determine the best fit function of $C_s=C_o(1-f_s)^{(k-1)}$ (commonly known as Scheil equation); where C_s is the known EMPA concentration data, C_o (C_o <1) and k (k<1)were the parameters to be determined. k is partition coefficient. An illustration has been shown below.

General model:
$$f(x) = a*(1-x)^{(b-1)}$$
Coefficients (with 95% confidence bounds):
a = 0.1604 (0.1588, 0.1621)
b =   0.8494 (0.8434, 0.8554)

Goodness of fit:
SSE: 0.004295
R-square: 0.9542
Adjusted R-square: 0.9537
RMSE: 0.006587

The blue line is the best fit. Partition coefficient (k) is determined to be 0.85.

C.3.   Segregation Ratio Plots

The calculated segregation ratio values (S.R.) for each sample were sorted into an ascending order. Figures C.5 to C.8 show the calculated S.R. values for Cr and Mo obtained along the line scan in the A&Q 0.52 and 0.77 wt% Cr plates. The calculated "pseudo-partition coefficient" (k) values for both as-rolled and A&Q plates were included in each figure. Three conclusions are drawn:

1. Based on the values of k in the as-rolled samples, than the 0.52 wt% Cr plate does not display a higher extent of microsegregation in than the 0.77 wt% Cr plate.
2. The tendency to segregate follows the trend: Mo > Cr.
3. Reduction in the extent of Cr and Mo microsegregation is clearly illustrated.
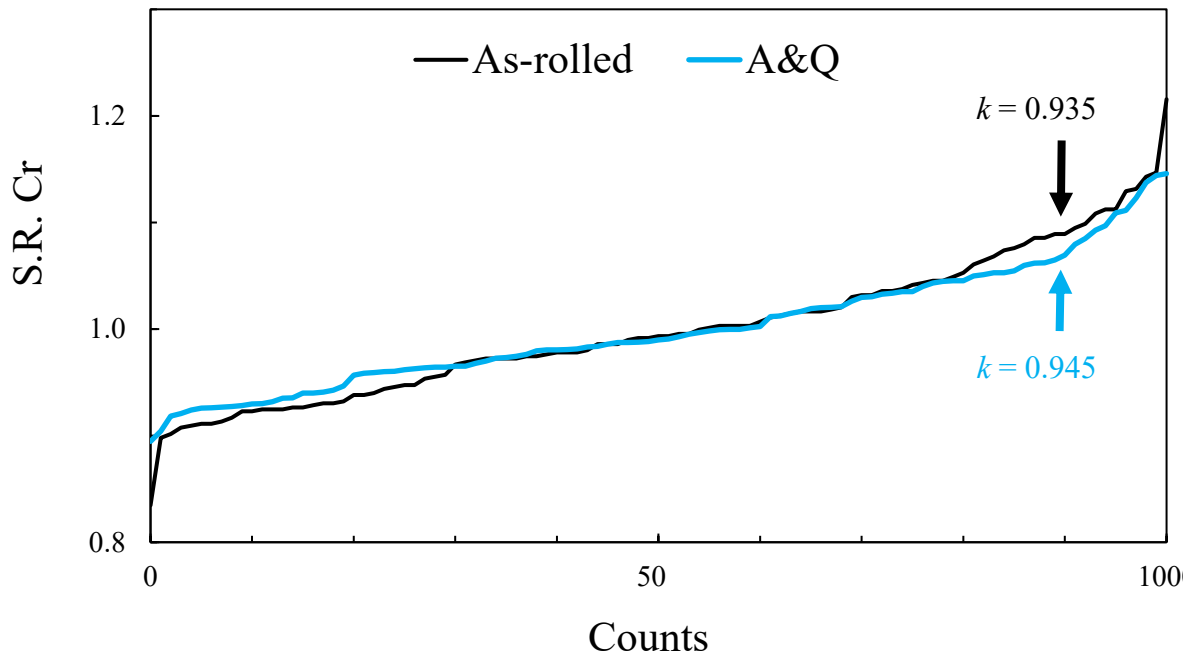
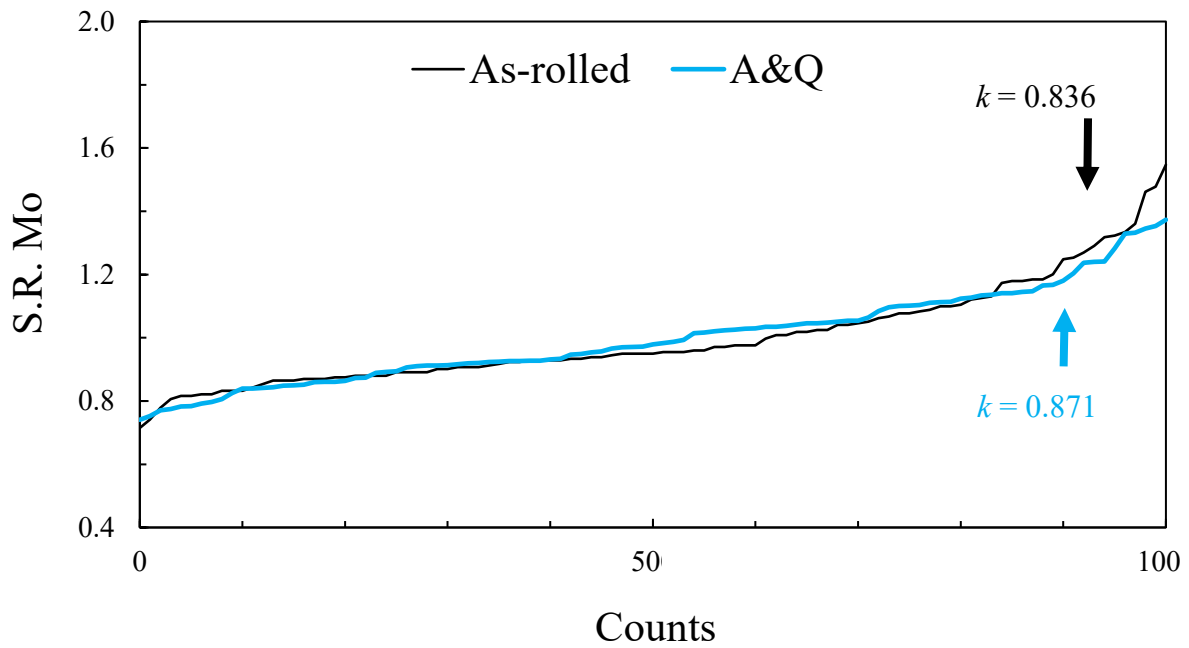**Figure C.5.** S.R. of Cr before and after austenitization (950 °C-30min) for 0.52 wt% Cr plate.

Figure C.6. S.R. of Mo before and after austenitization (950 °C-30min) for 0.52 wt% Cr plate.
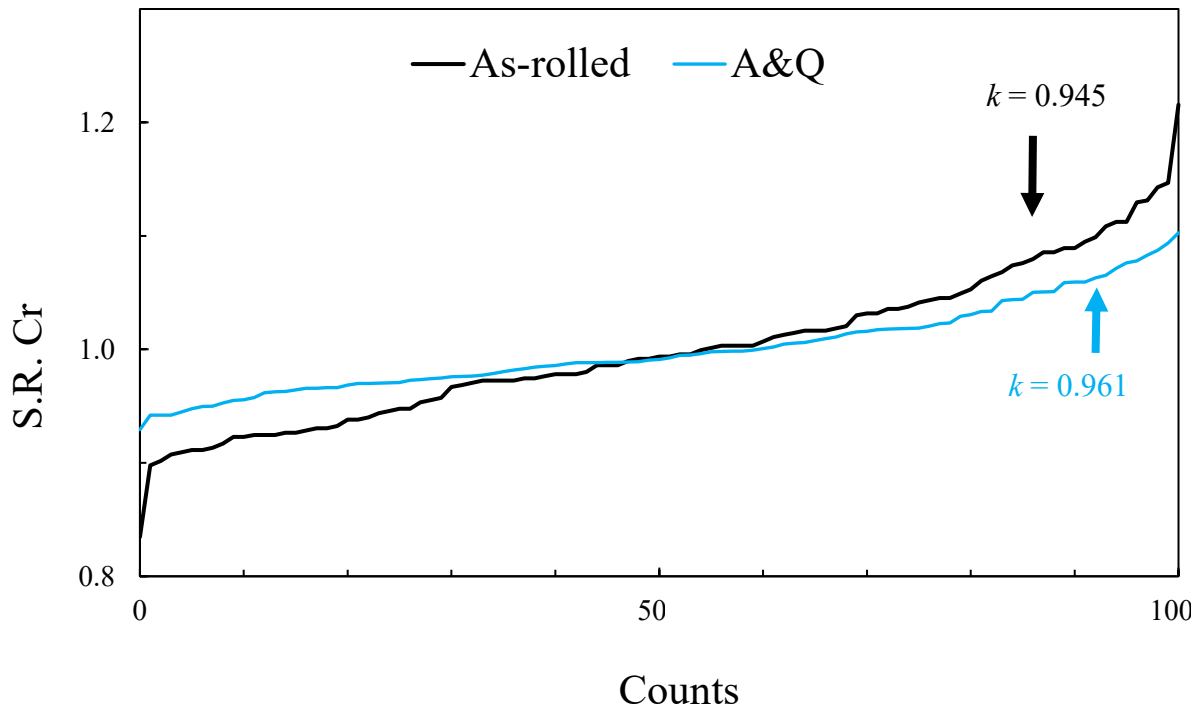
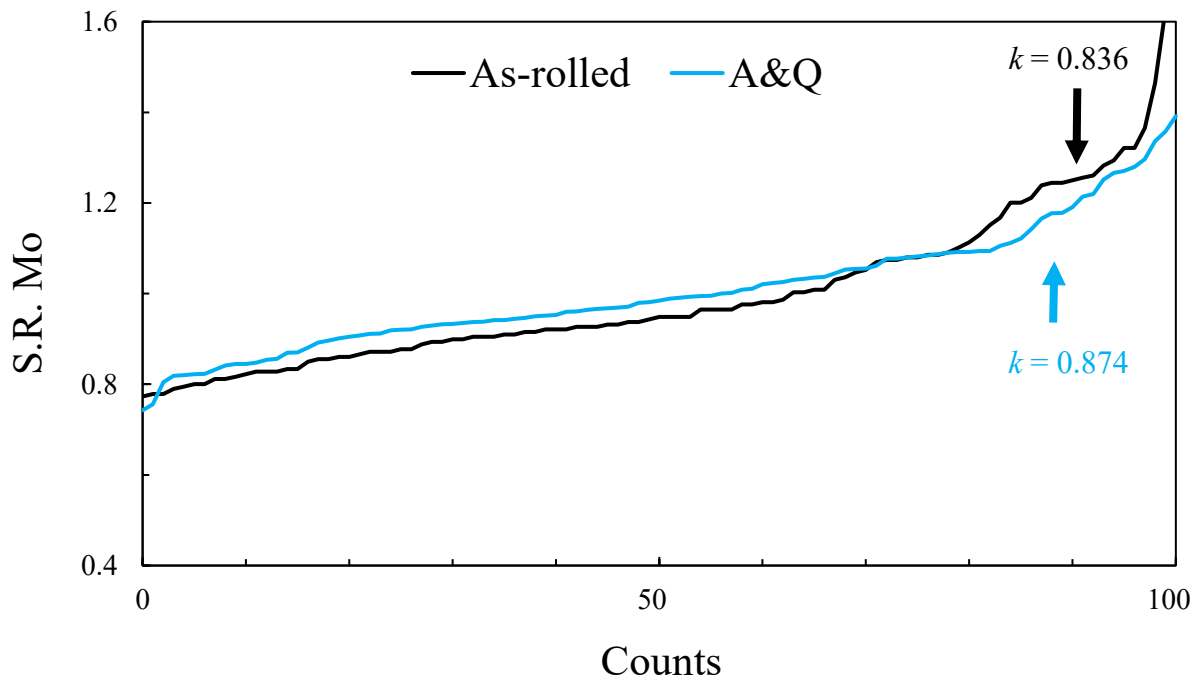**Figure C.7.** S.R. of Cr before and after austenitization (950 °C-30min) for 0.77 wt% Cr plate.

Figure C.8. S.R. of Mo before and after austenitization (950 °C-30min) for 0.77 wt% Cr plate.

Appendix D

Analysis on Tempered Plates

Table D.1. HJ, tensile properties, and micro-hardness values.

Temperature (°C)	Time (min)	HJ Parameter	YS (MPa)	UTS (MPa)	Elongation (%)	Hv 0.77 Cr (wt%)	Hv 0.52 Cr (wt%)
550	45	15.9	N/A	N/A	N/A	335 ± 4	329 ± 3
575	45	16.4	N/A	N/A	N/A	326 ± 4	318 ± 4
600	45	16.9	914.3	981.2	22.0	319 ± 5	310 ± 5
600	300	17.6	N/A	N/A	N/A	303 ± 3	300 ± 4
625	45	17.4	N/A	N/A	N/A	311 ± 4	307 ± 3
650	45	17.9	813.5	885.9	26.0	297 ± 5	294 ± 2
650	390	18.7	N/A	N/A	N/A	257 ± 4	253 ± 3
670	15	17.8	813.8	889.5	25.0	294 ± 6	289 ± 4
670	45	18.3	N/A	N/A	N/A	276 ± 3	272 ± 2
670	120	18.7	712.8	791.2	29.0	255 ± 4	258 ± 3
675	45	18.4	N/A	N/A	N/A	269 ± 4	268 ± 2
680	45	18.5	N/A	N/A	N/A	267 ± 3	266 ± 3
685	45	18.6	N/A	N/A	N/A	265 ± 3	260 ± 4
690	45	18.7	N/A	N/A	N/A	256 ± 2	255 ± 3
700	45	18.9	N/A	N/A	N/A	256 ± 3	254 ± 2
715	15	18.7	698.9	799.3	28.0	259 ± 6	258 ± 5
715	45	19.1	629.8	725.7	34.0	245 ± 3	242 ± 3
715	90	19.4	555.7	647.5	38.0	225 ± 3	220 ± 5